Title
Optimization, Characterization and Commissioning of a Novel Uniform Scanning Proton Beam Delivery System

Author
Mascia, Anthony Edward

Publication Date
2013

Peer reviewed|Thesis/dissertation

UNIVERSITY OF CALIFORNIA

Los Angeles

Optimization, Characterization and Commissioning of a Novel Uniform Scanning Proton Beam Delivery System

A dissertation submitted in partial satisfaction of the requirements for the degree Doctor of Philosophy in Biomedical Physics

By

Anthony Edward Mascia

2013

ABSTRACT OF THE DISSERTATION

Optimization, Characterization and Commissioning

of a Novel Uniform Scanning Proton Beam Delivery System

by

Anthony Edward Mascia

Doctor of Philosophy in Biomedical Physics

University of California, Los Angeles, 2013

Professor Daniel Low, Chair

Purpose: To develop and characterize the required detectors for uniform scanning optimization and characterization, and to develop the methodology and assess their efficacy for optimizing, characterizing and commissioning a novel proton beam uniform scanning system.

Methods and Materials: The Multi Layer Ion Chamber (MLIC), a 1D array of vented parallel plate ion chambers, was developed in-house for measurement of longitudinal profiles. The Matrixx detector (IBA Dosimetry, Germany) and XOmat V film (Kodak, USA) were characterized for measurement of transverse profiles. The architecture of the uniform scanning system was developed and then optimized and characterized for clinical proton radiotherapy.

Results: The MLIC detector significantly increased data collection efficiency without sacrificing data quality. The MLIC was capable of integrating an entire scanned and layer stacked proton field with one measurement, producing results with the equivalent spatial sampling of 1.0mm. The Matrixx detector and modified 1D water phantom jig improved data acquisition efficiency and complemented the film measurements. The proximal, central and distal proton field planes were measured using these methods, yielding better than 3% uniformity. The binary range

modulator was programmed, optimized and characterized such that the proton field ranges were separated by approximately 5.0mm modulation width and delivered with an accuracy of 1.0mm in water. Several wobbling magnet scan patterns were evaluated and the raster pattern, spot spacing, scan amplitude and overscan margin were optimized for clinical use.

Conclusion: Novel detectors and methods are required for clinically efficient optimization and characterization of proton beam scanning systems. Uniform scanning produces proton beam fields that are suited for clinical proton radiotherapy.

The dissertation of Anthony Edward Mascia is approved.

Nzhde Agazaryan

Magnus Dahlbom

David Saltzberg

Daniel Low, Committee Chair

University of California, Los Angeles

2013

Table of Contents

Table of Figures

Acknowledgements

As with any project as large as the development of new detectors and commissioning of a novel proton beam delivery system, my work could not have been accomplished without the collaboration of others.

For the development of the Multi Layer Ionization Chamber (MLIC), I would like to acknowledge Dmitri Nichiporov, Keith Solberg, Wen Hsi, Mark Wolanski, Jonathan Farr and Andries (Niek) Schreuder. For optimization and characterization of the uniform scanning nozzle, I would like to acknowledge Jonathan Farr, Wen Hsi, Chris Allgower, Frederick Jesseph, Andries (Niek) Schreuder, Mark Wolanski, Dmitri Nichiporov, and Vladimir Andferov. The collaboration and work of my colleagues was critical in the success of this project.

Vita

2002: Awarded Bachelor of Science in Physics at Fordham University

2005: Advancement to Candidacy in Biomedical Physics at University of California, Los Angeles

2005: Awarded Master of Science in Biomedical Physics at University of California, Los Angeles

2006: Began uniform scanning detector project at Midwest Proton Radiotherapy Institute

2007: Began uniform scanning proton beam delivery system project at Midwest Proton Radiotherapy Institute

2011: Certified in Therapeutic Radiologic Physics by American Board of Radiology

1 Introduction

In 1946, Robert Wilson published “Radiological Use of Fast Protons” in Radiology and made the first documented case for proton radiotherapy[1]. Eight years later at the University of California, Berkeley, the first patient was treated using protons. Proton therapy spread in 1954 to Uppsala University in Sweden and in 1961 to the Harvard Cyclotron Laboratory. Proton radiotherapy would remain isolated in national research laboratories for more than three decades. In 1990, Loma Linda University Medical Center (LLUMC) was the first institution to develop a hospital-based proton radiotherapy clinic[2]. Today, there exist eleven centers in the United States that specialize in proton therapy, with several additional centers in various stages of planning, development and construction. In 2003, the Midwest Proton Radiotherapy Institute (MPRI) became the third high-energy proton radiotherapy center in the United States. In 2008, MPRI became the first proton therapy center to utilize an active scanning beam delivery system in a high throughput clinical environment.

1.1 General Proton Therapy

Radiation therapy cures cancer. Radiation therapy harms normal tissue. The most important challenge in radiotherapy is maximizing the curative while minimizing the harmful effects of radiation. This simple axiom drives much of medical physics and radiation oncology research and development. If the dose can be escalated, greater tumor control is possible; however, normal tissue complications often arise with the use of greater doses. Many techniques, both available and emerging, have been deployed in radiation oncology that increase dose to the tumor while decreasing dose to normal tissues. Proton radiotherapy is one such technique that, through the basic physics of

proton interactions in matter, the radiation oncologist can often achieve greater tumor dose while minimizing the dose to normal tissue.

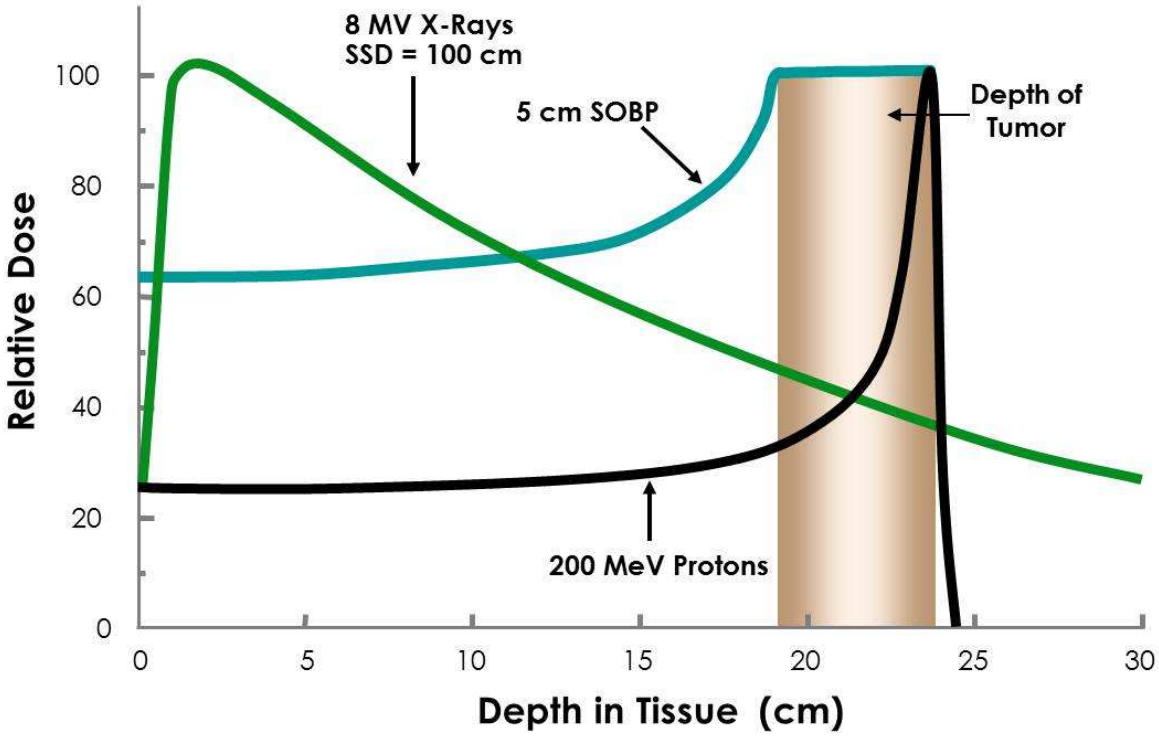

Figure 1. Pristine Bragg peak, spread out Bragg peak (SOBP) and 8MV X-ray depth doses. (Image courtesy of Niek Schreuder, Indiana University Proton Therapy Center).

In examining the depth-dose curves of protons and megavoltage x rays, see Figure 1, it becomes evident that protons exhibit unique dose deposition properties that can be exploited for radiotherapy. Photons deliver dose by indirectly ionizing electrons that then "locally" deposit energy. For photons, the greatest dose is delivered near the patient entrance surface, creating a dose peak within the secondary electron build-up region. Thereafter, the dose falls off exponentially with depth. Protons continuously lose energy as they traverse the medium. At the end of the energetic proton range, the proton energy is deposited in peak region, known as the Bragg peak. Since proton

radiotherapy was initially postulated, dose has been delivered to targets by summing many Bragg peaks into a single spread out Bragg peak (SOBP).

As the proton beam exits the cyclotron, it is unsuitable for radiotherapy. The proton beam spot is very small, typically only one centimeter in width. In order to provide tumor coverage, the beam must be modified to cover larger fields, sometimes 30cm or more in diameter. The most ubiquitous method used to achieve this large field is passive scattering[3,4]. This is available at MPRI in treatment room 1 (TR1) and has been commissioned and clinically treating patients since 2003. The gantry rooms at MPRI use scanning magnets, which scan the proton beams in predefined patterns, to generate large clinical proton fields.

Several longitudinal modulation techniques are utilized in addition to the transverse modulation techniques. In passive scattering systems, a range modulating propeller, milled from a solid block of plastic, graphite or aluminum, rotates in the beamline[5,6]. This rotating, stepped propeller incrementally scans the Bragg peak depth based on the step size and proportion of beam charge on that step. This process sums many incremental Bragg peaks into a single, flat, spread out Bragg peak (SOBP). For an active beam delivery system such as the scanning system, an incremental step wedge is used. In this study the step wedge acts as a binary range modulator.

Without further modification of the proton beam, SOBP dose distributions produce rectangular isodose distributions in water phantoms. The distal isodose curves corresponding to the distal dose falloff lie parallel to the water surface. Many, if not most, patients have curved skin surfaces, so the distal isodose curves will track the

curved skin surface. Add internal heterogeneities, and the distal dose distribution will be a complex surface that will not generally conform to the distal tumor shape. A range compensator is used to modify the proton energy distribution at the patient surface such that the energy compensates for the patient surface, internal heterogeneities, and tumor shape such that the distal dose falloff conforms to the distal target volume surface. The relevant quantities necessary to calculate the dose distribution, and subsequently, the compensator shape, are the stopping power of the patient's tissues. These are inferred from a computed tomography (CT) simulation scan, which is also used to segment the tumor and normal organs. The compensator is designed such that the greatest energy protons stop at the distal edge of the target volume. Proton radiotherapy is a three-dimensional, conformal radiation treatment modality and has shown great promise in the treatment of cancer.

1.2 Scanning Beam Detectors

Scanning an ionization chamber along the beam axis in a water phantom is the standard method for measuring depth-dose and longitudinal beam profiles for both x-ray and proton radiotherapy[7,8,9,10], see Figure 2. In the passive spreading system, depth scans are performed with the Markus parallel-plate chamber and the Wellhofer water phantom, which employs three dimensional linear motors. The Wellhofer system scans the Markus chamber along any of three orthogonal axes. The ionization chamber current is continuously sampled using an electrometer. Depth scans, which are often used to measure the Bragg peak range, entrance dose or SOBP size, the Markus chamber is scanned along the axis corresponding to the beam direction, either towards or away from the beam source.

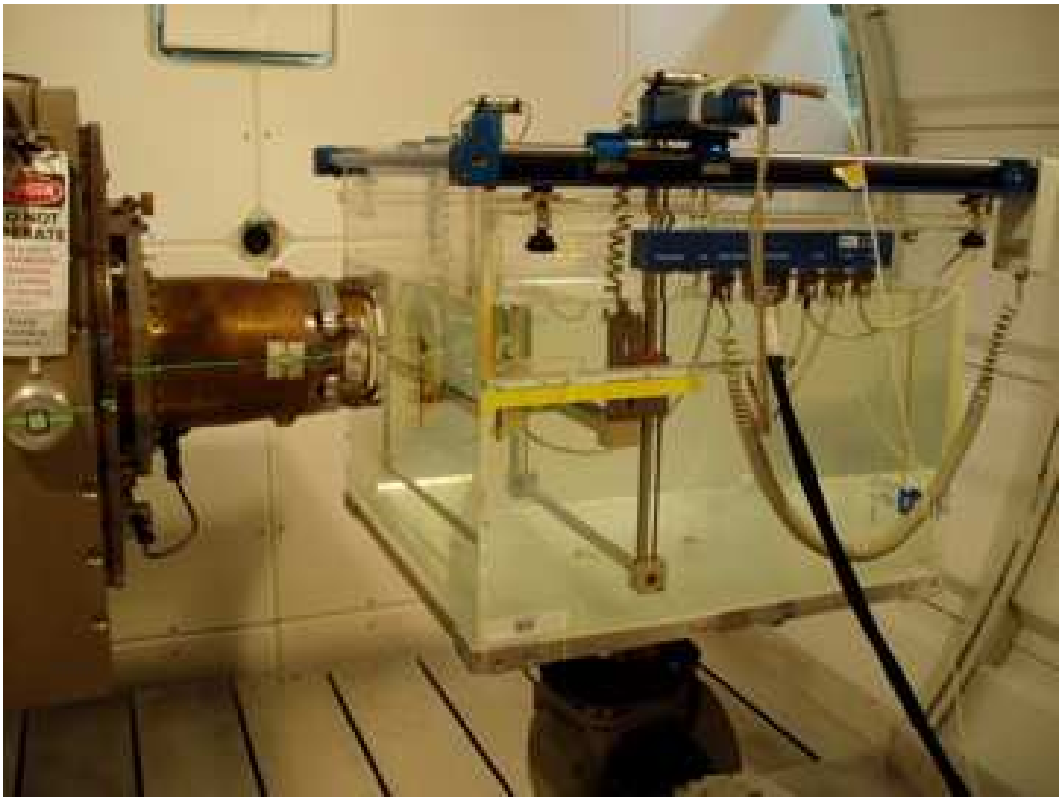

Figure 2. Water phantom, Markus chamber setup in gantry room.

Unlike passive spreading, in uniform scanning, the beam is stacked, layer-by-layer in depth along the beam axis, so such a moving detector method will not work. One method used at MPRI in the uniform scanning environment is referred to as “point-by-point” measurement. The ion chamber is placed at one location, the entire radiation field is delivered, and the charge from the electrometer is recorded. The chamber is then moved to the next location and the process is repeated. Though this method yields accurate results for a typical depth-dose measurement, which can be well characterized by acquiring 15-20 discrete points, this method is quite time consuming, requiring 15-20 minutes per depth-dose scan.

For longitudinal profile measurements, The Magic Cube, which is a quasi-3D detector[11], was designed for hadron radiotherapy at the University and Istituto Nazionale di Fisica Nucleare (INFN) of Torino, see Figure 3. The Magic Cube is a stacked, strip ionization chambers with near water equivalent slabs of material to degrade the hadron beam. The Magic Cube has an active area of 24 x 24 cm^2. Each sensitive area is essentially a parallel plate ion chamber with dimensions 0.375 x 24.0 cm^2. Loma Linda tested this chamber in a clinical proton beam. The major drawback of this detector was its "quasi-3D" nature. The spatial sampling in one transverse direction was approximately 0.4cm, while perpendicular to that transverse direction there was no spatial measurement sampling because the sensitive volume spanned the length of the active area. This detector was only developed as a prototype, and due to its limitations, no commercially available version exists.

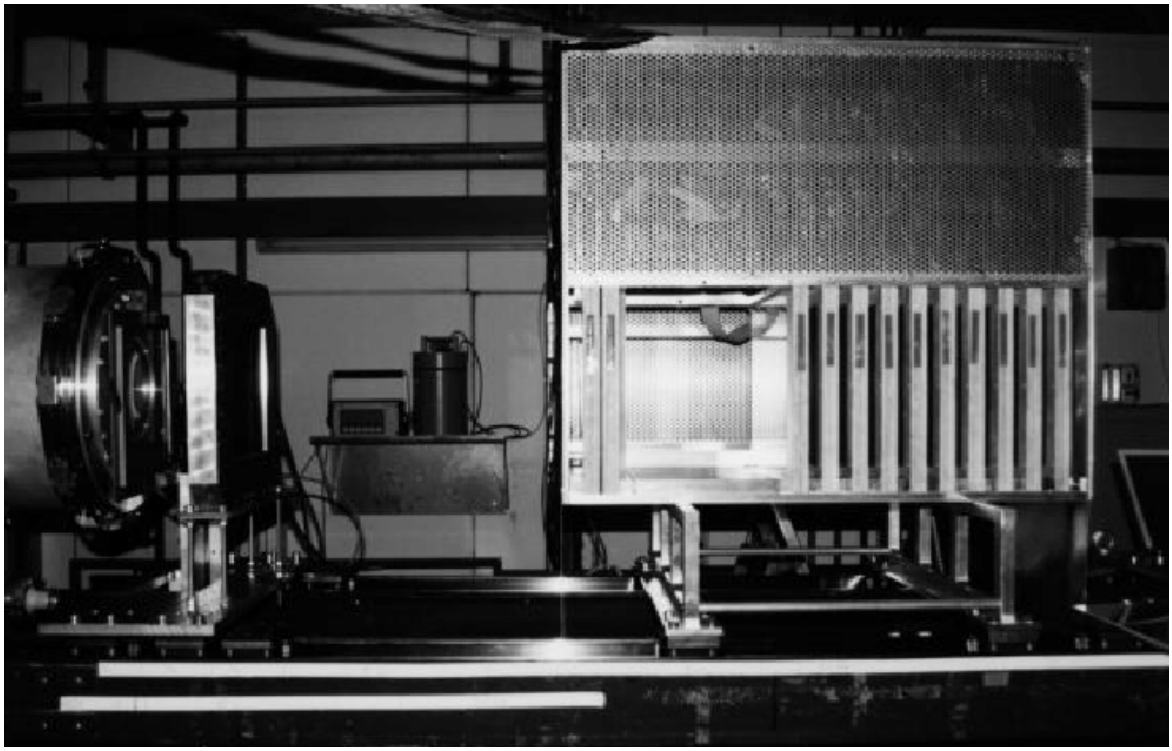

Figure 3. Photo of Magic Cube[11].

The Matrixx detector (IBA Dosimetry, Germany) was used for transverse measurements in commissioning, other dosimetry projects and quality assurance at MPRI, discussed in-depth in Section 2.3. The precursor to the Matrixx detector was a 1024 ion chamber 2D array, the Pixel Ionization Chamber (PXC)[12], see Figure 4. PXC was developed for transverse profile measurements at University and Istituto Nazionale di Fisica Nucleare (INFN) of Torino. Each ion chamber was a parallel plate ion chamber with 0.4 cm diameter and 0.55 cm height, with a center-to-center spacing of 0.75 cm. The mini-chambers, each with a volume of 0.07cm^3, were arranged in a 24 x 24 cm^2 matrix. The detector utilized fast electronics to process the signal at the detector and digitally read out the entire 2D array to be subsequently analyzed using a personal computer.

Figure 4. Pixel Ionization Chamber (PXC). Presented from Cirio et al.

Radiochromic and radiographic film dosimetry were explored as potential detector devices[13,14,15,16]. Though films are well characterized integrating detectors with a long history of radiotherapeutic applications, there were several drawbacks. Neither film system acted as a real-time detector. Precise radiographic film dosimetry takes extreme and often tedious care, especially with regard to the measurement process. For example, to get consistent results, the measurer needs to manage “time to development” sensitivity, variation among film lots, film processor dependence and energy dependence. Given the large amount of commissioning and quality assurance (QA) data that needed to be collected, the inconveniences of using film did not allow for sufficiently efficient measurements. However, because film is an accepted standard for

relative dosimetry, the transverse detectors were benchmarked and commissioned based on their agreement with film-based measurements. Importantly, neither film system accurately measured the depth-dose, especially in the high LET, Bragg peak region. The LET changed significantly over the proton depth-dose, therefore leading to significant under-response in the high LET, Bragg peak region.

1.3 Facility and System Architecture

1.3.1 Cyclotron and Beamline

Proton radiotherapy requires the use of proton accelerators in order to generate and deliver a radiation beam to the patient. There exist different types and models of accelerators available for proton radiotherapy. The two most common models of proton accelerators are cyclotrons and synchrotrons. In the traditional cyclotron, as at MPRI[17,18,19], the proton is injected into a fixed magnetic field. The protons accelerate across radiofrequency acceleration cavities, gaining energy through every cavity. The strong magnetic field inside the accelerator bends the path of protons, keeping them in a nearly closed orbit. As the proton energy increases, the radius of the protons' trajectory increases like a spiral until it is "kicked" out of the cyclotron by a magnetic switch. In a synchrotron, the proton is injected into a fixed radius accelerator. The proton accelerates across the radiofrequency acceleration cavities and its energy increases. As the energy increases, the bending and focusing magnet magnetic fields are increased in order to apply a stronger force. This ramping magnetic field fixes the radius of the protons' trajectory through the accelerator. Because of the different acceleration techniques, a cyclotron produces a continuous beam, whereas a synchrotron produces a pulsed beam.

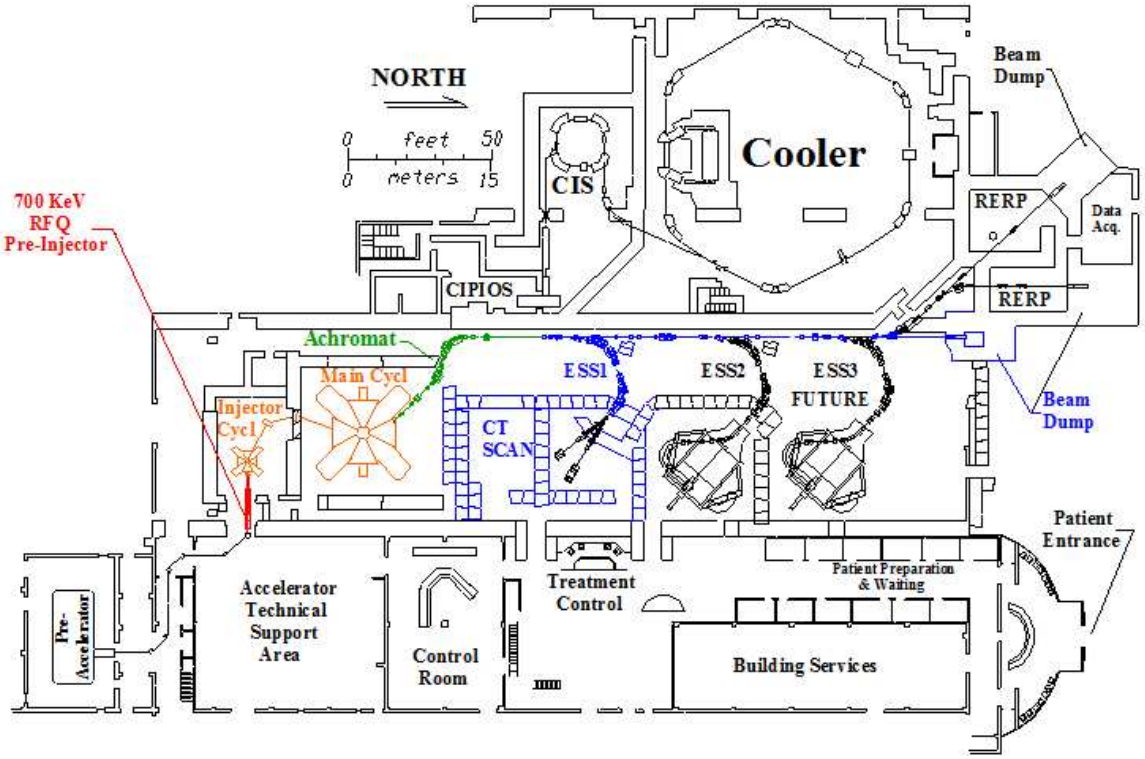

Figure 5. Indiana University - Midwest Proton Radiotherapy Institute facility layout.

After thermalizing and ionizing hydrogen gas, the proton plasma is injected into the pre-injector accelerator in which the protons are accelerated to approximately 10 MeV. Upon exiting the pre-injector accelerator, the protons are transported through a beamline to the main stage cyclotron, which accelerates the protons to approximately 208 MeV. Upon exiting the cyclotron accelerator, the proton beam travels down the trunkline. The trunkline is under high vacuum such that the accelerated protons do not interact with undergo no interaction in air. The trunkline transport a 208 MeV proton beam to the energy selection (ES) system of each treatment room. The one cyclotron provides a proton beam to three treatment rooms. Fast kicker magnets, located near the entrance to each ES line, divert the proton beam from the trunkline into the ES lines. The proton beam can enter one ES line at a given instance, but the beam cannot beam delivered to

more than one ES line simultaneously. In the ES line, the maximum energy is degraded by two Beryllium wedges. This degrader allows for the selection of any energy required for patient treatment less than or equal to the maximum energy from the cyclotron. After the energy is degraded to the requested treatment energy, the proton beam enters the treatment room.

1.3.2 Gantry and Uniform Scanning

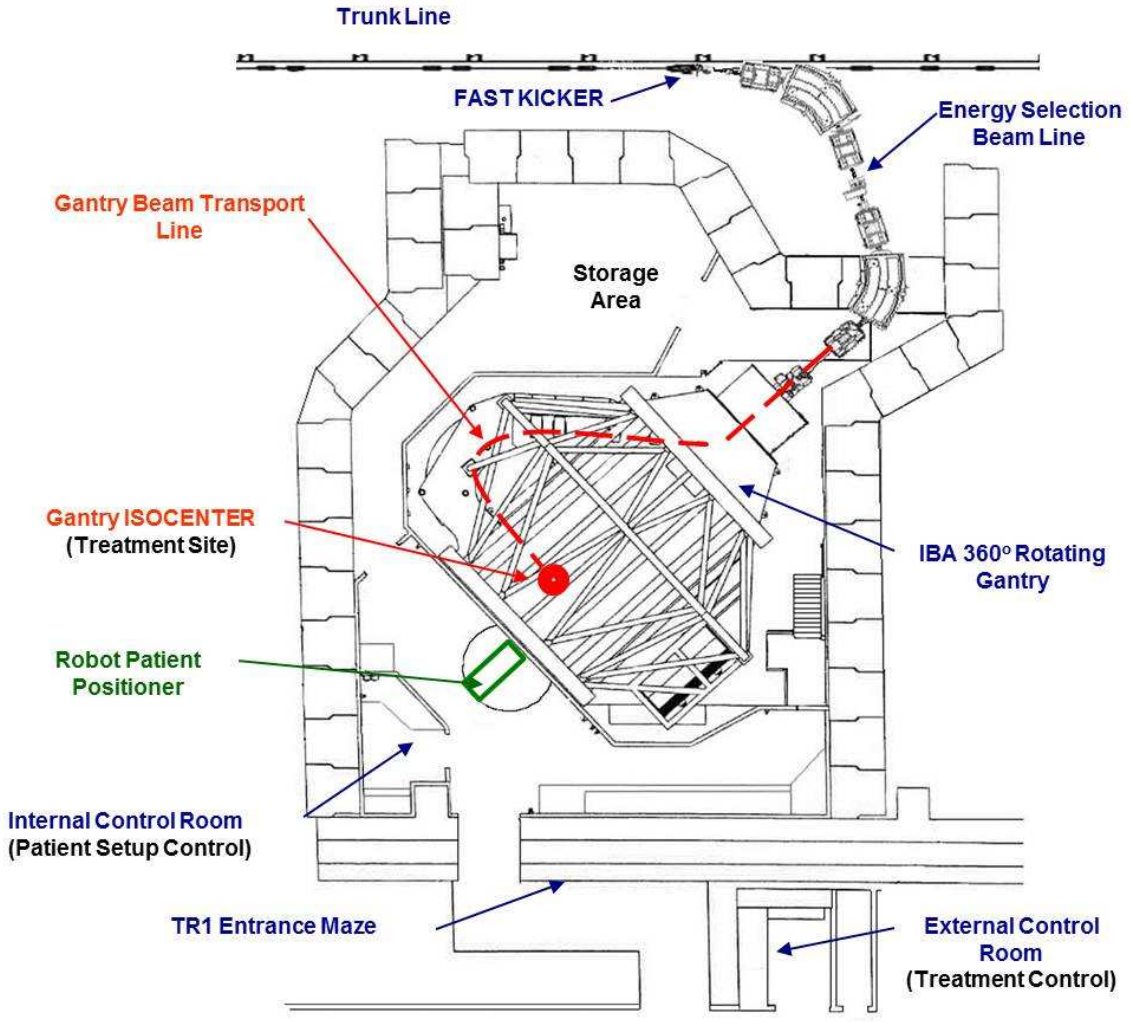

Figure 6. Gantry treatment room layout, including trunkline, shielding, ES line, and rotating gantry.

For the project, the main focus is in the gantry treatment rooms which contain an active scanning system[20,21], see Figure 6. This active scanning system represents a significant technological advancement, being the first active and uniform scanning system deployed for routine clinical use. There are other types of proton scanning systems, but they differ in clinical use or delivery method[22,23,24,25]. The scan magnet sweeps a pencil proton beam in the x and y directions in a raster scan pattern. At isocenter, this scanning technique creates an integral flat large-field. The magnet scans the pencil beam across the entire field at 15 Hz. The wobbling system has several advantages and improvements over conventional double scattering method. Due to the less than optimal energy of the MPRI cyclotron (i.e. 208.4 MeV), the active spreading system minimizes the energy loss through the treatment delivery beamline. In double scattering systems, the pencil proton beam loses almost 2.5 cm equivalent range in water due to the energy loss across the scattering foils when the beam is spread laterally to 20cm. When using the active spreading system, there is no energy loss, except that in air and thin windows at the entrance and exit of the beamline and monitor chambers. Because the scanning magnet can theoretically provide any field size within clinical limits, the fraction of the proton beam that strikes the aperture is reduced and secondary radiation dose to the patient is limited.

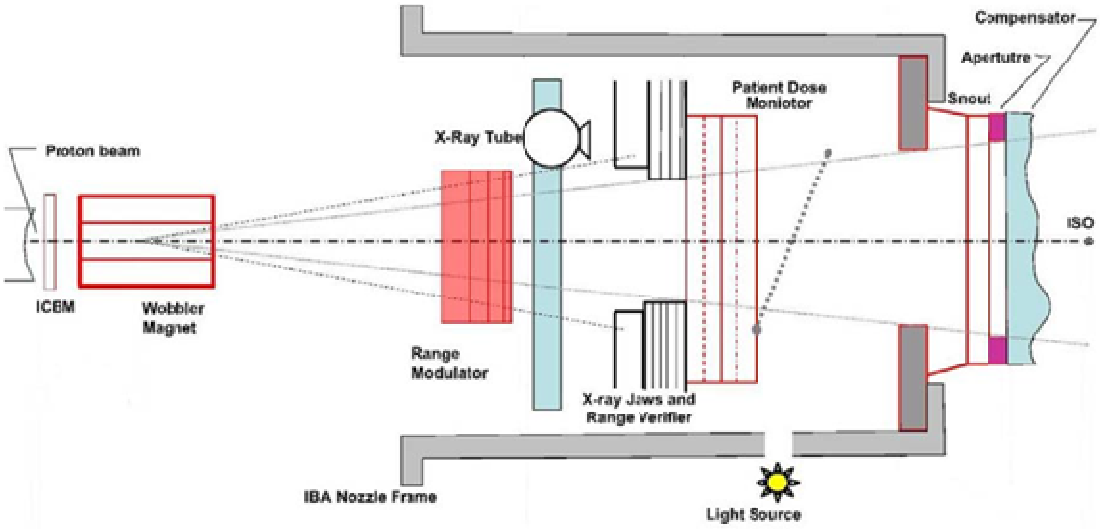

Figure 7. Uniform scanning nozzle layout.

As the scanning magnet sweeps the proton pencil beam in the plane perpendicular to the beam, the binary range modulator degrades the beam in discrete steps, modulating the proton beam depth. The range modulator is comprised of several slabs of Lucite and Carbon of varying thickness. These slabs are inserted into and removed from the beamline in combinations that reduce the proton beam energy in precisely controlled and known steps. The number of protons delivered to the patient for each energy layer is carefully selected to yield a Spread Out Bragg Peak (SOBP). This energy stacking system is significantly different from and has advantages over the more traditional modulation propeller. With the modulation propeller, the proton beam is swept across the entire depth of the field nearly 48 times per second. With the current design of the energy stacking method, the entire depth of the tumor will be scanned only once. In principal, the energy stacking method can accommodate as many or few sweeps in depth as desired within an engineering limits. Though MPRI operates with a library of

verified SOBPs, any SOBP size is theoretically possible within bins of 3mm, the minimum amount of degrading with the range modulator.

After the wobbling magnet and binary range modulator, the proton beam then passes through the dose monitor ion chamber. This chamber serves as a pass-through detector and the ionization charge provides a measurement of the number of protons traversing the nozzle. The charge is converted to monitor units by the treatment control system. At this point, the proton beam enters the snout which is the only remaining section of the nozzle. The snouts in each of the gantry rooms are identical. An aperture is inserted at the end of the snout and trims the proton beam to the prescribed radiation portal shape, typically corresponding to the beam's eye view of the tumor. A compensator is placed downstream of the aperture and degrades the proton beam energy across the beam such that the distal proton range conforms to the distal tumor surface.

1.4 Specific Aims and Goals

Uniform scanning beam delivery is still an evolving technological innovation for particle therapy. Uniform scanning beam delivery is currently utilized at less than half of the operating proton therapy centers in the United States, including the University of Florida Proton Therapy Institute, four ProCure Treatment Center locations, and Indiana University Proton Therapy Center. Only at ProCure Treatment Centers and Indiana University does uniform scanning serve the entire clinical population. Though national and international guidelines exist for conventional proton therapy, standards and guidelines for scanning beam optimization, characterization and commissioning is limited[26,27,28,29,30]. At this time, an American Association of Physicists in Medicine task

group on proton therapy acceptance and commissioning is not available. This project represents the largest, integrated contribution to the implementation, optimization and characterization of a uniform scanning system available in the literature today. This project is divided into three main components, each of which represents a unique contribution to the available knowledge base in uniform scanning.

In short, this project optimized, characterized and commissioned the first clinical uniform scanning nozzle in the world and, to that end, designed, developed and characterized the measurement tools necessary to perform such a task.

1.4.1 Detector Development and Characterization for Uniform Scanning

During the planning and design phase of the first uniform scanning system, there existed no detectors or detector accessories designed for efficient and effective uniform scanning commissioning. In order to fill that need, this project identified the specifications of such a detector and detector accessories. The development project was separated into two categories—longitudinal and transverse measurements.

The specifications for measuring a uniform scanning depth-dose (longitudinal measurements) were defined. The design of a prototype detector was based on the measurement need and specifications. The prototype was designed, fabricated and tested. Based on the results, a clinical version of the detector was designed, fabricated and implemented clinically. The detector was then characterized and released for commissioning the uniform scanning system. The detector aided in performing the full system optimization and characterization.

A commercially available two-dimensional ion chamber array was identified suitable for transverse measurements characterizing the uniform scanning system,. However, the need for multiple measurement depths in water was critical for the optimization and characterization of the uniform scanning system. Therefore, a commercially available one-dimensional translational water phantom system was retrofitted for the purposed of multiple depth transverse profiles. The detector and an adapted accessory aided in performing the full system optimization and characterization.

1.4.2 Optimization and Characterization of the Binary Range Modulator in the Uniform Scanning Environment

The binary range modulator (BRM) is a key component used for longitudinal layer stacking installed in the uniform scanning nozzle. The BRM modulates the range of the pristine Bragg peak in incremental steps by pneumatically driving slabs of known water equivalent thickness into and out of the beam path. After the developer installation, the BRM was not capable of delivering proton radiation fields as needed by the proton therapy clinic. This project developed the initial process and input to the BRM for the delivery of clinically useful proton radiation fields. Furthermore, this project identified the limitations of the system architecture and led to improvements and optimizations in the system design in order to achieve clinical usability. The performance of the BRM was characterized and commissioned for use in the proton therapy clinic.

1.4.3 Optimization and Characterization of Wobbling Magnet in Uniform Scanning Environment

The wobbling magnet is a key component used for transverse large spot scanning in the uniform scanning nozzle. By quickly varying the magnet field, the wobbling magnet scans the proton beamspot in a predefined pattern in order to achieve a flat uniform radiation field at isocenter. After installation by the developer, the wobbling magnet delivered a limited scan pattern which was not optimized or suitable for proton radiotherapy. This project developed the initial scanning patterns and input for the wobbling magnet. Furthermore, this project identified key parameters of the scanning pattern which were later used for optimization. The limitations of the uniform scanning implementation were explored, and the clinical results optimized. The performance of the wobbling magnet was characterized and commissioned for use in the proton therapy clinic.

2 Uniform Scanning Proton Beam Detectors

2.1 Introduction

The uniform proton beam scanning system is an active beam delivery system. As an active system, the proton beam spot is scanned at various frequencies in three dimensions. Conventionally, the detectors often used in radiotherapy environments are "active" detectors in that the detector, often an ion chamber, is scanned in order to acquire a beam profile in one of three dimensions. However, if the delivery system is "active," for example intensity modulated radiotherapy (IMRT) or uniform-scanning proton delivery, the detector must be passive. In the case of IMRT, film or two-dimensional ion chamber or diode arrays are commonly used for relative dosimetry. In order to acquire meaningful beam data, the beam and the detector cannot both be scanned without synchronization which proved impossible at the 15Hz frequency in the uniform scanning system. Due to this fact, alternative and new detectors were investigated and developed.

2.2 Longitudinal or Depth-Dose Detector: Multi Layer Ion Chamber (MLIC)

The Multi Layer Ion Chamber (MLIC) was developed to acquire longitudinal beam profiles in a precise, accurate and efficient manner.

2.2.1 Early Prototype Development

Early in the uniform scanning system development, the realization was made that effectively measuring the scanning beam would be as important as delivering the scanning beam. With the clear limitations of scanning detectors, there existed a need to develop a depth array of ionization chambers. This was incorporated into the design of the Multi Layer Ion Chamber (MLIC).

The prototype MLIC consisted of 64 parallel plate ion chambers arranged in a longitudinal array. Multi Channel Gated Integrator (MCGI) cards were used in the electronics and, along with economics, provided the limiting factor for the number of ionization chambers. The prototype had 64 channels, so 64 ionization chambers were available.

Each detector piece was designed for and fabricated from G-10 computer board. G-10 computer board is a particle board with double-sided copper laminate. The copper thickness per plate is about 100 μm for commercial 1-pound (i.e., 1lb./ft.) G-10 board. Each board contained a signal pad and lead, and a high voltage pad and lead. The detector consisted of 65 identical G-10 boards, see Figure 11, with the components etched out of the copper laminate – 64 ionization chambers plus a front high voltage only board. The boards were stacked longitudinally with the high voltage pad on the back of one board providing high voltage pad and therefore electric field for the subsequent board's signal pad, and so on.

The size of the detector element was designed from a practical standpoint with three constraints. First, the signal pad had to be large enough to provide adequate signal,

with the conservative estimate of the total signal noise from cables, electronics and environmental factors being +/- 4.0 nanoAmps (nA). Second, the signal pads had to be small enough to preserve transient equilibrium and Bragg-Gray corollary thereby forcing the chamber area to be “significantly smaller” than the radiation field. In this case, the proton beam spot was about 2.5cm at the full-width, half-maximum. The typical field size of a proton therapeutic radiation field is typically greater than 5.0cm with the reference condition field size at MPRI at 10.0cm diameter. Third, the signal must be greater than the noise (ie, signal-to-noise ratio must be greater than 1.0). A Microsoft Excel sheet was designed for fast computation of signal according to signal pad dimension, see the results page of that sheet in Figure 8.

Calculation of Ionization Current in Parallel Plate Detector		
Constants	density air (g/cm3) =	1.29E-03
	W (MeV/ion-pair) =	3.48E-05
	elemental charge (nC) =	1.60E-10
	stopping power for 200MeV p+ (MeV*cm^2/g) =	4.52
	beam current (nA) =	2.00
Detector Parameters	air gap (cm) =	0.30
	detector element radius (cm) =	2.22
	detector element area (cm^2) =	15.48
	field size diameter (cm) =	10.00
	field size area (cm^2) =	78.50
Calculation	beam protons / sec =	1.25E+10
	created ionpairs / sec =	1.24E+11
	Ionization Current (nA) =	19.81 +/- 4 nA

Figure 8. Results page from Ionization Current Calculation Sheet.

The MS Excel sheet summary, Figure 8, is based on transforming the beam current in the beam delivery system, through unit conversion and application of experimental design, into collected ionization current. Using the constraints governing signal pad diameter, the air gap could be adjusted to ensure adequate signal ionization current. The handwork of this transformation is shown below.

The assumptions are as follows:

$$\frac{dE}{dx} = 4.518\frac{MeV}{g/cm^2}\ ;\ stopping\ \ power\ \ for\ 200MeV\ \ protons\ in\ air$$

$$\rho_{air} = 1.29\times10^{-3}\frac{g}{cm^3}\ ;\ density\ of\ \ air$$

$$W_{air} = 34.8\times10^{-6}\frac{MeV}{ionpair}\ ;\ \ energy\ \ per\ ion\ \ pair$$

$$p^+ = 1.602\times10^{-10}\,nC\ ;\ elemental\ \ cha\,rge$$

Figure 9. Ionization chamber collection assumptions.

The beam current transformation can be approximated by:

$$beam\ current\left(nA\ or\ \frac{C}{s}\right)\times\frac{p^+}{C} = \frac{p^+}{s}$$

$$\frac{p^+}{s}\times\frac{dE}{dx}\times\rho_{air}\times(air\ \ gap)\times\frac{ion\ \ pairs}{MeV} = \frac{ion\ \ pairs}{s}$$

$$\frac{ion\ \ pairs}{s}\times\frac{C}{ion\ \ pair}\times\frac{area\ \ of\ \ pad}{area\,of\ \ field}\times\left(ISL\ \ \ from\frac{dose\,monitor}{d\,etector}\right) = collected\ \ current\left(nA\ or\ \frac{C}{s}\right)$$

Figure 10. Equations used to transform beam current into collected detector current based on ion chamber parameters.

According to the three constraints, the signal pad should be as close to the size of the proton beam spot size while still remaining small compared to typical radiation fields. Since the typical beam spot FWHM is 2.5cm (ie, 1 inch), 2.2cm (ie, 7/8 inch) was used as the prototype signal pad diameter. When applying this signal pad dimension to the device, the three constraints were satisfied and the signal-to-noise ratio was approximately 1.2. This study was satisfactory to move the detector elements toward fabrication and development, see Figure 11.

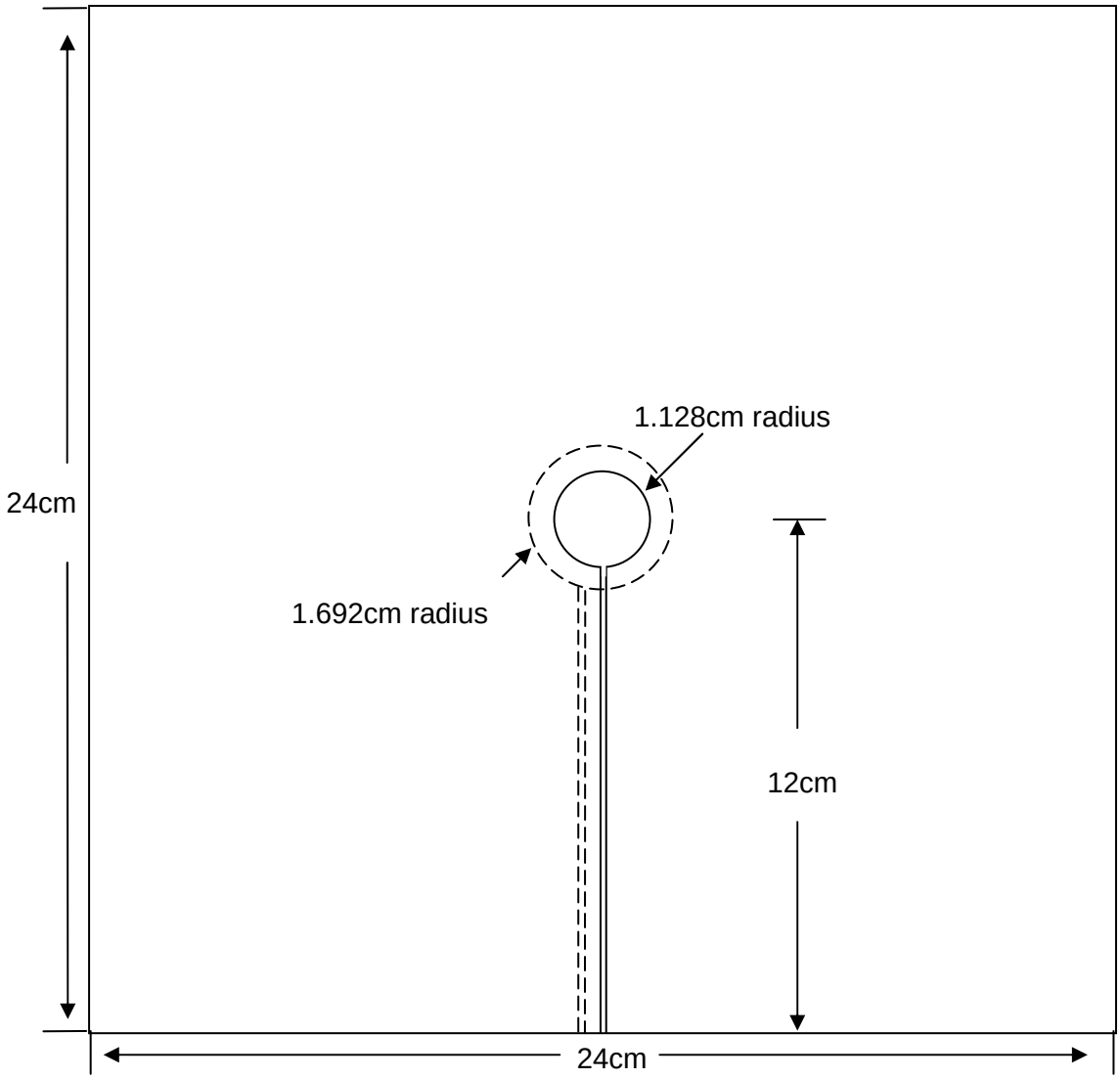

Figure 11. Computer aided design of MLIC detector element.

After the detector board elements were designed, the composite detector dimensions were analyzed. Based on typical therapeutic ranges of between 8.0 and 27.0cm in water, the 80%-to-20% distal penumbra, or the D80-20, was approximately 0.45cm and the D90-10 was 0.75cm. Based on an analytical study, see Figure 12, the distal edge of the Bragg peak was adequately characterized by spatial sampling of 1mm, 2mm and 3mm. There was no significant change from 1mm to 3mm spatial sampling. However,

as the spatial sampling approached 4mm, the distal edge was no longer adequately characterized and the shape became perturbed by under-sampling. A range loss measurement using standard, industrial G-10 board, with 0.060" double-sided 1 oz. copper laminate, was performed and the water-equivalent thickness of 1.00mm (G-10) was determined to be 2.75mm at a nominal proton range of 20.0cm in water. Applying this result to the detector design yielded an inherent depth-dose spatial sampling of 2.75mm. With a 2.75mm water equivalence and spatial sampling, the typical therapeutic proton ranges measurement would have at least 3-5 discrete points in the distal edge. This was enough to adequately measure the standard proton depth-dose characteristics (i.e. R90, R80-20, R50, etc).

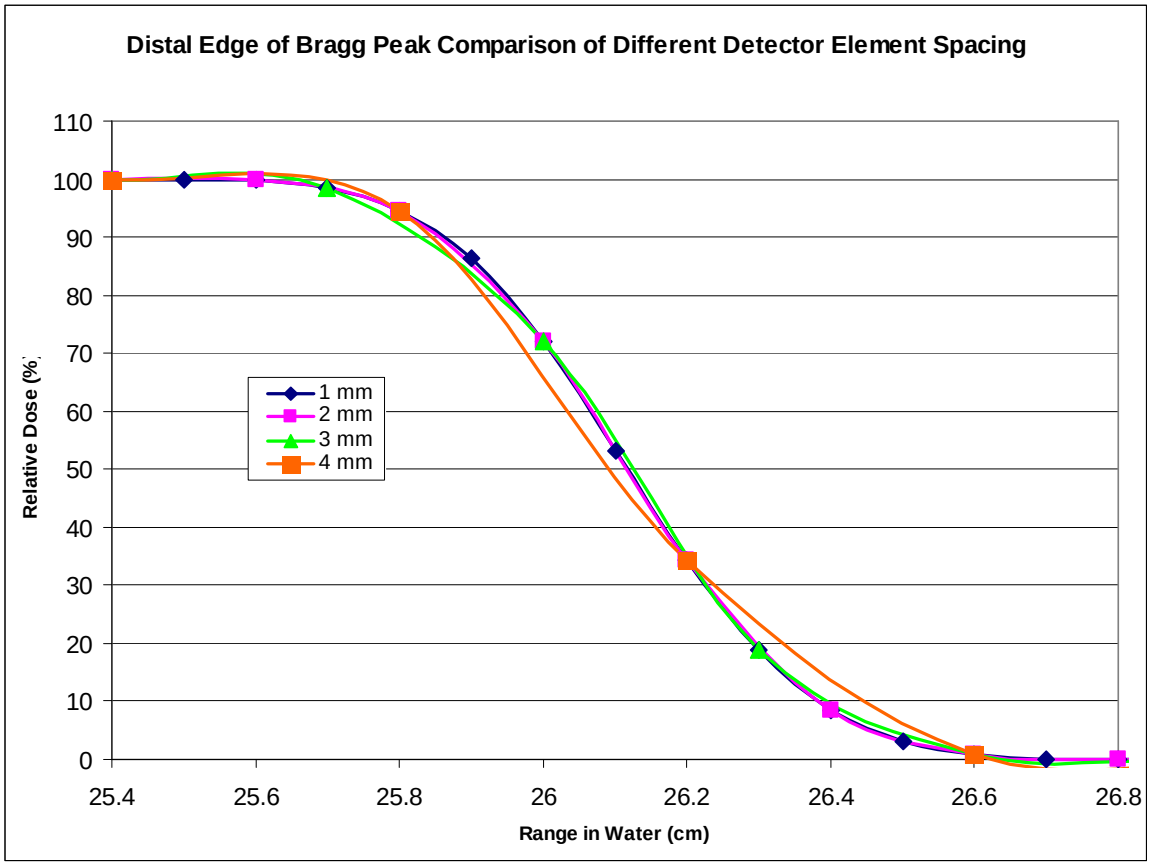

Figure 12. Comparison of distal edge measurement shape based on detector element spacing.

Characteristics of the original boards, such as ease of fabrication, good conductivity of copper signal pads and leads, and rigidity of the individual boards were important factors triggering the initial construction and fabrication, but the prototype MLIC exhibited significant limitations. Because the detector elements were predominantly made of copper, the etched pads exhibited a greater multiple Coulomb scattering as compared with water. In Figure 13, a water tank scan is compared to an MLIC measurement with two signal pad of two different diameters, 1.0cm and 2.0cm. The Copper signal pads demonstrate increased scatter as compared to water. As the proton beam traverses each signal pad, the increased scatter is compounded. The result is a perturbation of the distal end, called “distal fall through”. The 2.0cm diameter signal pad shows an improved agreement with water as compared to the 1.0cm diameter signal pad. For the 2.0cm diameter signal pad, the signal is higher as compared to the 1.0cm diameter, and therefore the relative contribution of the increased scatter is smaller.

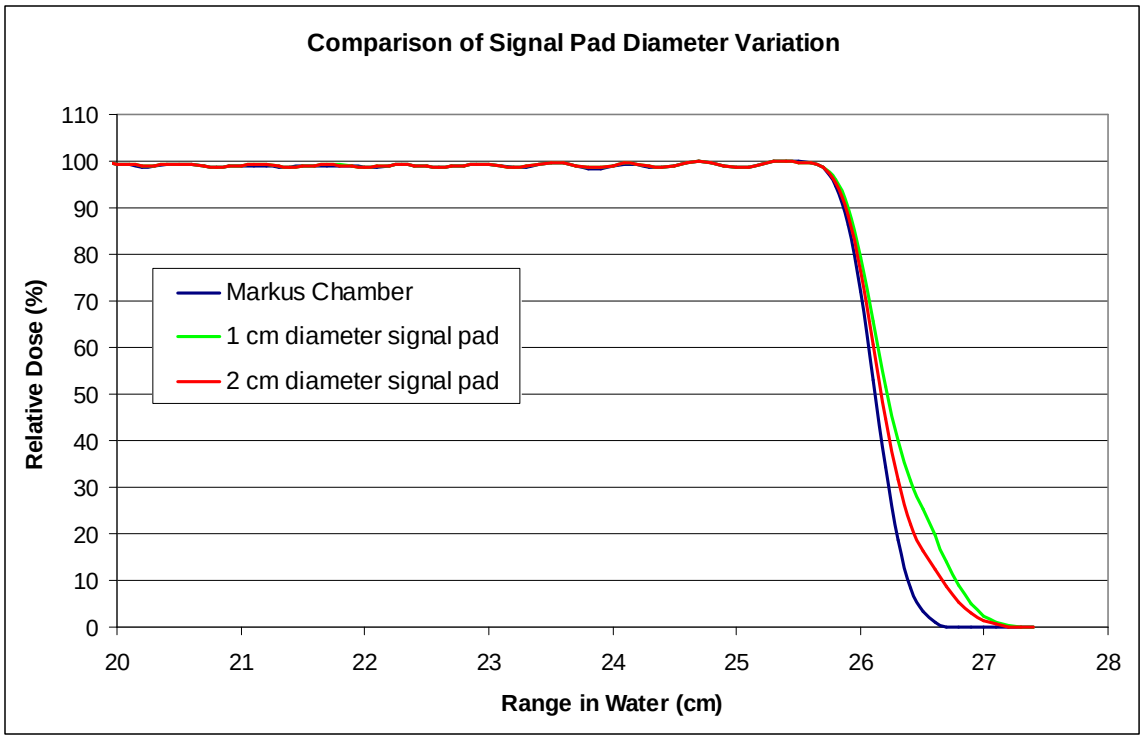

Figure 13. Effect of increased multiple coulomb scattering when comparing an in-water measurement (Markus Chamber) and two signal pad dimensions (1cm and 2cm diameters), where the signal pad is made of Copper.

Furthermore, the electron density and stopping power for copper was significantly different than water. According to most dosimetry protocols, when possible, it is important to perform benchmark dosimetric measurements in water or water-equivalent material. However, in this case, the prototype was only a relative detector and therefore water-equivalence was not required provided a proper cross-calibration was conducted and referenced.

2.2.2 Multi Layer Ion Chamber (MLIC), Version 2 : Designed, Fabricated and Implemented

After building and testing the prototype, the design was refined for the production and clinical implementation version of the Multi Layer Ion Chamber (MLIC)[31]. The prototype predominant design flaw was the copper pads and leads. A depth-dose array of 128 ion chambers, which required a stack of 129 signal and high voltage pads made of Copper, significantly perturbed the proton beam by causing additional distal fall through and increase multiple Coulomb scattering. These effects were not desired in a detector used for commissioning and quality assurance. The clinical implementation MLIC model materials were therefore changed.

The MLIC, see Figure 14, is composed of 122 parallel-plate ion chambers in a 1D array. The MLIC is fabricated from 16cm x 16cm x 1/16" thick high impact polystyrene plates with Kapton insulated leads. As compared to the prototype, the change in materials from Copper to polystyrene, graphite and Kapton converted the detector into a nearly water equivalent device. The detector elements reside in an aluminum housing with thin acrylic windows at the entrance and exit. The ion chambers are vented to ambient air, and the housing includes ports for dry air flushing during periodic maintenance.

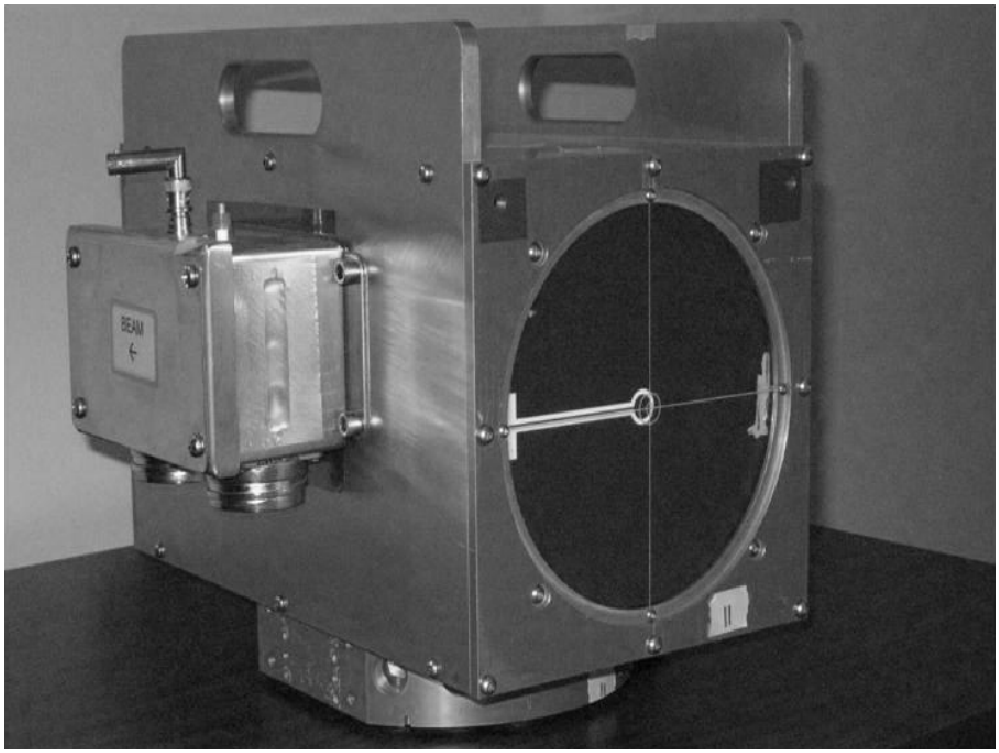

Figure 14. Multi Layer Ion Chamber (MLIC), clinical implementation version.

Each parallel-plate ion chamber was composed of a high voltage pad, signal pad and air gap. The water equivalent thickness of each ion chamber was 1.8mm. This yielded a water equivalent detector length of 220mm. The inherent spatial sampling was 1.8mm. If the measurement required, the spatial sampling could be increased by acquiring two measurements – one with no range absorber and one with a 1mm range absorber – and superimposing the two measurements. This would effectively improve the spatial sampling by a factor of 2. However, in practice, 1.8mm spatial sampling was adequate to characterize a proton beam with sub-millimeter accuracy.

In order to reduce the signal pad diameter to enable the measurement of smaller radiation fields and at the same time preserving good signal-to-noise, the electronics and cabling design was modified. The prototype design required cabling to carry signal from

the detector to the control system in the external control room. For the clinical version, cabling connected the detector to the data acquisition system positioned no more than 10 meters away. The variable sampling time and charge integration were handled by custom-built multiple channel, gated integrator modules. The integrated charge was converted to a digital signal and transported to the external control room through fiber optic cabling. This reduced the distance the analog signal travelled as compared to the prototype, decreasing the overall system noise. This allowed a reduction in signal pad diameter from 10mm to 6mm while still preserving adequate signal-to-noise.

The software was designed in-house to control the detector, acquire data and provide basic analysis. In the software, the chamber bias (100-500V) and sampling time (0.02 to 3000ms) were selected. The data were acquired and viewed in real-time or cumulative mode. The data analysis package performed basic analysis and reports basic properties of the proton depth-dose, such as range in water at distal 90% dose and modulation width at proximal 90% to distal 90%. The software also exported the raw and corrected data in text file form for analysis in a spreadsheet.

2.2.3 Multi Layer Ion Chamber Calibration

The calibration of the MLIC involved three main components – the water equivalent thickness measurement of a single detector element, the offset based on the entrance window water equivalent thickness, and the uniformity, or gain, calibration of each ionization chamber. The initial two components were discussed in the preceeding sub-chapter. The water equivalent thickness of a single detector element is 1.8mm. For

measurement, the acrylic entrance window was removed, so its offset was 0. This section addresses the gain calibration.

Each detector element was composed of polystyrene with graphite leads and Kapton insulation. The detector elements were drafted using computer aided design software and exported to a specialized machine shop for fabrication. The fabrication and etching machines operated with a high degree of reproducibility with tolerances at 3/1000” or 0.1mm. In addition, the housing and rack for the detector elements was fabricated at the Indiana University machine shop to the same specification and tolerances.

Despite the strict machining tolerances, the housing and rack were designed with additional play to accommodate small variations in fabrication. These variations impacted the ion chamber volumes. A more significant effect was the curvature and bow of the individual detector elements. A primary disadvantage of the polystyrene boards was their flexibility and lack of rigidity. Due to fluctuations in ambient temperature and pressure, the polystyrene expanded and contracted. Because of transportation of the detector to different treatment rooms and mounting the detector at different cardinal angles, the detector elements shifted slightly. The variations and fluctuations in the detector shape and location non-systematically modified the ionization chamber volumes. As the chamber volume varied, the signal varied. For this reason, a gain calibration was required.

A robust calibration routine was developed to efficiently and accurately calibrate the gain of each ionization chamber. The gain calibration required a consistent radiation benchmark that was easily characterized and highly reproducible. The calibration had to

be independent of daily beam intensity and energy fluctuations. The calibration benchmark had to be a consistent radiation source with relatively shallow dose gradients and had to be readily available. The calibration routine also had to provide a gain value for each of the 122 chambers.

The entrance region of a 210 MeV pristine Bragg peak, Figure 15, was the most stable and reproducible region of the Bragg peak. The entrance region dose was independent of many day-to-day variable factors, such as cyclotron energy and energy spread, that affected the Bragg peak. Because the entrance region exhibited a shallow dose gradient, each chamber in the MLIC was calibrated to a similar dose. The shallow gradient of the entrance region was easily fit by fitting a polynomial. This simplified the calibration routine.

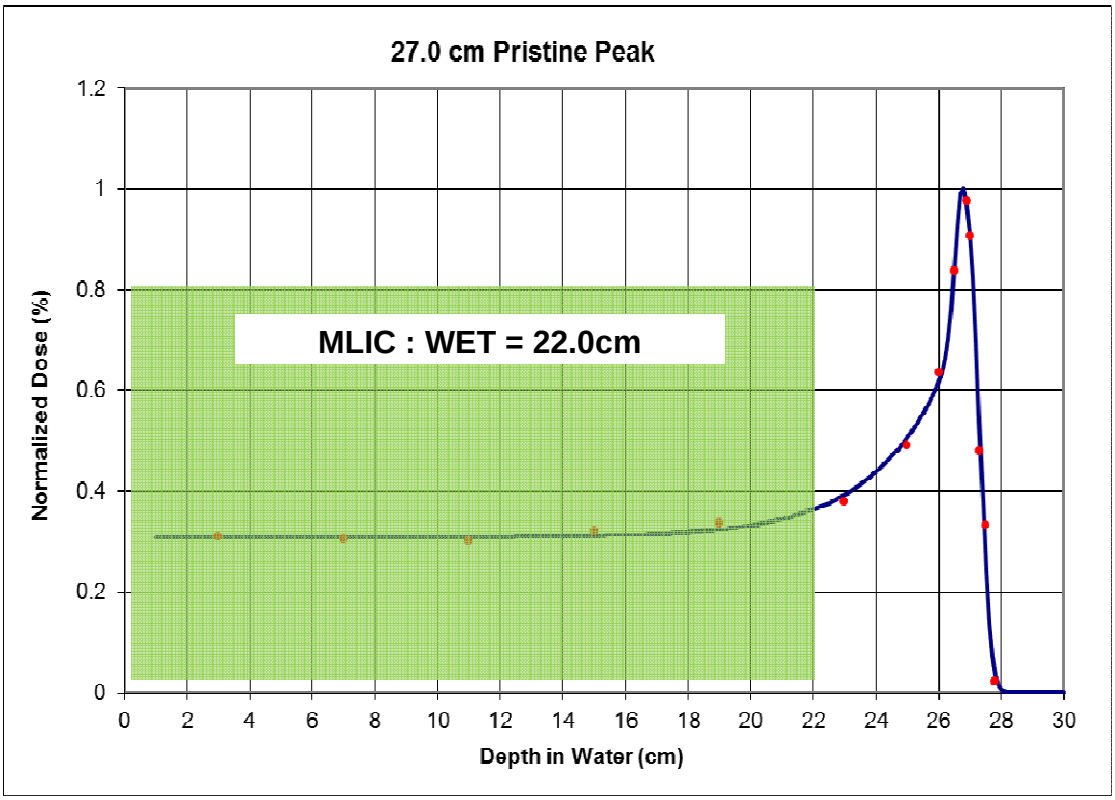

Figure 15. Entrance region of a 210 MeV Bragg peak used for MLIC gain calibration. The blue line is the measured pristine Bragg peak. The red markers are discrete ion chamber point-by-point measurements in uniform scanning treatment room for validation. The green rectangle represents the MLIC.

2.2.3.1 Multi Layer Ion Chamber Gain Calibration Routine

Prior to the first use, each MLIC ion chamber was assigned a default gain calibration factor of 1.00. Using this factor, the on chamber signals varied by approximately +/- 30%. This was due to the issues discussed previously related to the variation in construction of each ion chamber and its volume. In practice, for each measurement session, a new gain calibration was acquired and the previous calibration was overridden.

In order to calibrate the MLIC, the detector was positioned with the front face at isocenter with the chamber array along the central axis of the proton beam. A background measurement was acquired using the background acquisition routine in the software. This provided a background reference measurement (e.g. leakage current) that was subsequently subtracted from each field measurement. The calibration reference beam delivery was as follows: a pristine Bragg peak, 27.0cm range in water (i.e. maximum range), 10cm diameter field size, 100 monitor units. The gain calibrations were determined using these measurements, Figure 16.

The measured day-to-day gain calibration variation was +/- 5% per MLIC ion chamber. The pre-calibration measurement exhibited significant detector variation and noise and could not be used for high precision measurements, see Figure 16. Because of the detector construction, the gain calibration of the each chamber oscillated about the true value. For example, if a chamber had a gain calibration value greater than 1.0, the preceding and following chambers often had a gain calibration of less than 1.0. This was because a single detector element board contained the signal pad of one chamber and the high voltage pad of the following chamber. If a detector element expanded or flexed decreasing the volume of one chamber, it often increased the volume of the abutting chamber.

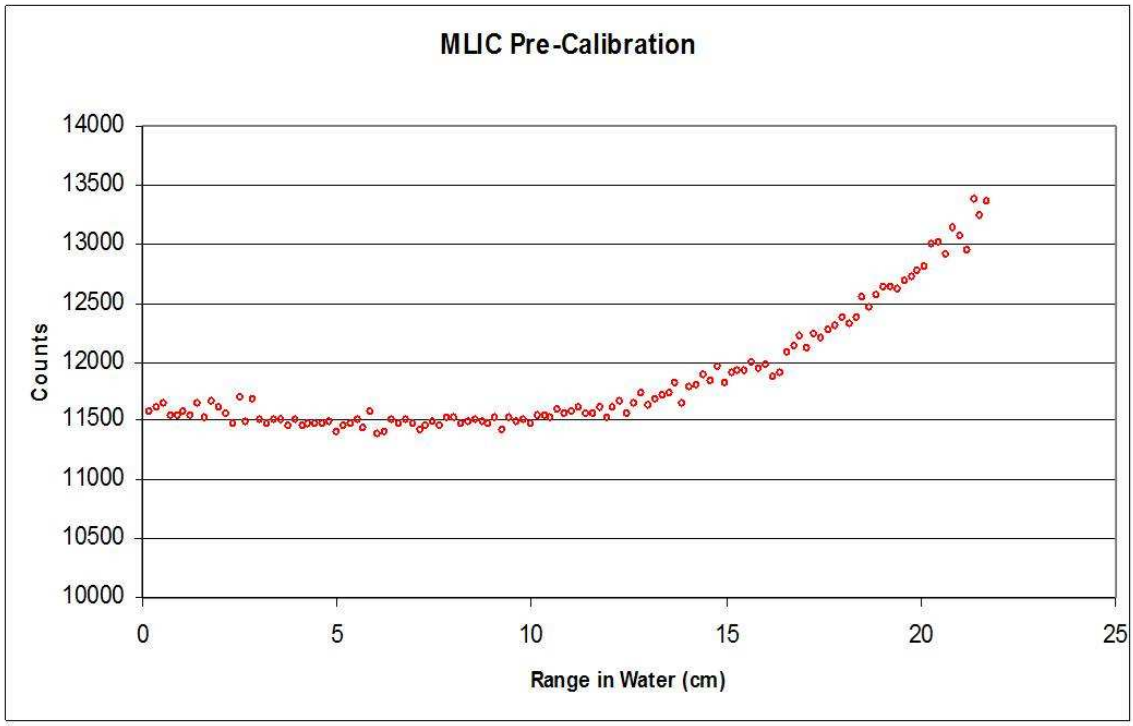

Figure 16. Pre-calibration measurement. Each red marker is a detector element ion chamber.

A reference curve was established to compare against the measured ionizations, see Figure 17. The reference Bragg peak was measured in the passive scattering system using continuous ion chamber scanning mode with the 3D water tank and fit with the standard Bragg peak Bortfeld model curve[32]. That measurement was validated using point-by-point measurement in the uniform scanning room. This yielded a stable, averaged entrance region of a pristine Bragg peak. The curve was normalized such that the maximum in the Bragg peak was 100 counts. Therefore, the entrance region of the reference curve ranged from 32 to 37 normalized counts. The normalized counts were proportional to normalize dose when the measured Bragg peak maximum was normalized to 100% relative dose.

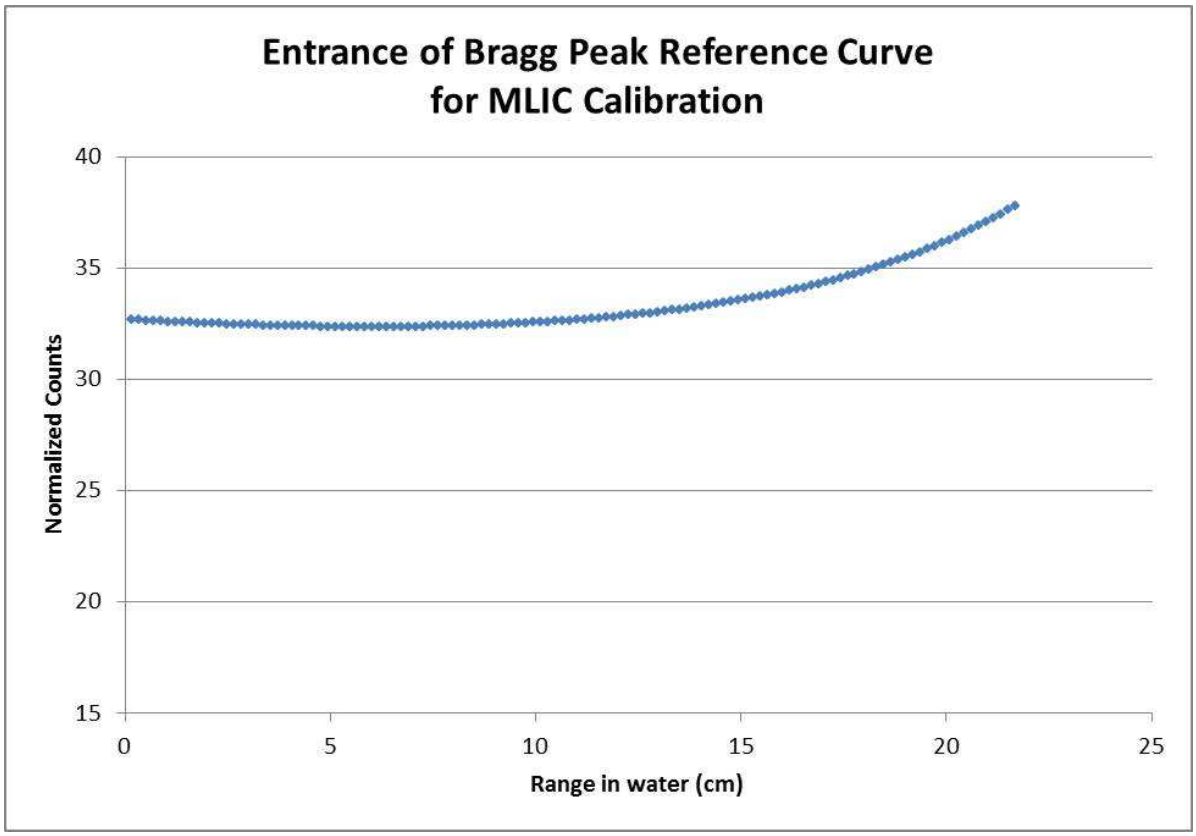

Figure 17. Reference pristine Bragg peak for MLIC calibration.

An ion chamber gain calibration dataset was produced using the pre-calibration measurement and the reference curve. The MLIC calibration curve dataset was stored in a text file named “cal_depth.txt” in the home directory of the MLIC software. The text file, see Figure 18, was composed of five columns in ASCII format: channel ID, water equivalent depth in centimeter, gain calibration factor, electronics card identification, and electronics card address. An in-house calibration script was designed to efficiently calculate the daily gain calibration values and generate a new, replacement calibration text file with the new values.

#Depth ChannelId	Detector:	X Distance(mm)	direction Cal_multiplier		in Card	USER1 Address	Coordinates Offset
#8-JUN-2006							
1	0.182	1.020176571	0x5B00	0x00			
2	0.36	0.689829158	0x5B00	0x02			
3	0.538	0.839236066	0x5B00	0x04			
4	0.716	0.76403845	0x5B00	0x06			
5	0.894	0.823880363	0x5B00	0x08			
6	1.072	0.737949479	0x5B00	0x0A			
7	1.25	0.748902273	0x5B00	0x0C			
8	1.428	0.858112376	0x5B00	0x0E			
9	1.606	0.728213418	0x5B00	0x10			
10	1.784	0.828669844	0x5B00	0x12			
11	1.962	0.685233635	0x5B00	0x14			
12	2.14	0.776646424	0x5B00	0x16			
13	2.318	0.914724725	0x5B00	0x18			
14	2.496	0.860329664	0x5B00	0x1A			
15	2.674	0.662455411	0x5B00	0x1C			
16	2.852	0.944277149	0x5B00	0x1E			
17	3.03	0.65500631	0x5B40	0x00			
18	3.208	1.00886728	0x5B40	0x02			
19	3.386	0.684815485	0x5B40	0x04			
20	3.564	0.806492961	0x5B40	0x06			
21	3.742	0.801098627	0x5B40	0x08			
22	3.92	0.872743488	0x5B40	0x0A			
23	4.098	0.778911031	0x5B40	0x0C			
24	4.276	0.773355323	0x5B40	0x0E			
25	4.454	0.822382	0x5B40	0x10			
26	4.632	0.748740484	0x5B40	0x12			
27	4.81	0.865941894	0x5B40	0x14			
28	4.988	0.757971783	0x5B40	0x16			
29	5.166	0.841688723	0x5B40	0x18			
30	5.344	0.778313749	0x5B40	0x1A			
31	5.522	0.707331178	0x5B40	0x1C			
32	5.7	0.968657338	0x5B40	0x1E			
33	5.878	0.700361798	0x5B80	0x00			
34	6.056	0.899769672	0x5B80	0x02			
35	6.234	0.752539103	0x5B80	0x04			
36	6.412	0.815144952	0x5B80	0x06			
37	6.59	0.791819582	0x5B80	0x08			
38	6.768	0.983729953	0x5B80	0x0A			
39	6.946	0.704524608	0x5B80	0x0C			
40	7.124	0.830527143	0x5B80	0x0E			
41	7.302	0.784921209	0x5B80	0x10			
42	7.48	0.886724811	0x5B80	0x12			
43	7.658	0.641881182	0x5B80	0x14			
44	7.836	1.042078631	0x5B80	0x16			

Figure 18. Example of "cal_depth.txt", the calibration file for the MLIC.

Using the acquired and reference data, the calibration algorithm was straightforward:

$$\frac{M_i}{M_{REF,i}} * M_{64} = C_i$$

$$M_i = M_{signal,i} - M_{background,i}$$

Figure 19. Gain calibration algorithm.

where "i" was the channel ID, M_i was the measured signal at a specific channel, $M_{REF,I}$ was the measured signal for reference curve at specific channel, M_{64} was the measured signal for reference curve at channel 64, and C_i was the gain calibration factor. The measurement at a specific channel (M_i) was the measured signal ($M_{signal,i}$) after subtraction of the measured background signal ($M_{background,i}$).

After the new calibration file was generated, a verification measurement was performed to ensure the new calibration file adequately compensated for the MLIC ion chamber gain variations. The verification measurement showed that the gain compensation process improved the comparison between MLIC-measured and actual depth dose, see Figure 20.

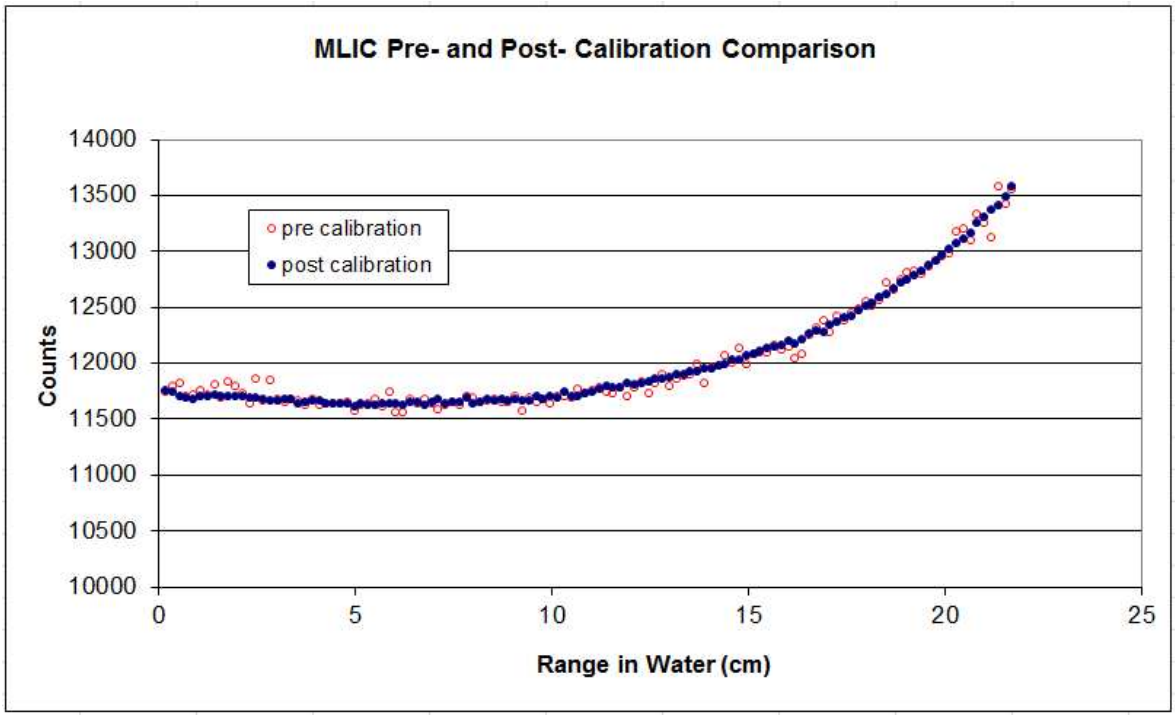

Figure 20. Comparison of pre- and post-calibration measurements.

2.2.3.2 Multi Layer Ion Chamber Clinical Impact

The MLIC significantly increased the efficiency of clinical activities that required substantial data collection. A typical efficiency improvement using an MLIC was one order of magnitude. For example, performing point-by-point measurements could yield 3-4 well characterized depth-doses per hour. In contrast, using the MLIC, 30-40 well characterized depth-doses per hour measurements were possible. This work represented the first thorough test of a 1D integrating depth dose detector in a scanning proton beam environment with a focus on clinically efficient and reproducible results.

2.2.4 The Zebra (IBA Dosimetry, Germany)

In 2008, IBA Dosimetry designed and fabricated a prototype for a commercially available device for the commissioning of the IBA Particle Therapy uniform scanning system. That prototype was based on the Indiana University MLIC, as the only detector like it at the time. Throughout 2008 and early 2009, I was on the development team liaising with IBA Dosimetry on the design and commercial implementation of the device hardware and software. My responsibility was to provide clinical and technical feedback on the prototype detector. This feedback was used to fine tune the future commercially available release. In 2009, the first commercially available Zebra was released to ProCure Proton Therapy Center for clinical characterization and integration. The results of that characterization are address in published literature and are not the subject of this dissertation[33].

2.3 Transverse Detector: ImRT Matrixx (IBA Dosimetry, Germany)

With the beam characterized along the beam-axis direction by the MLIC, the plane perpendicular to the beam-axis also required characterization. Film is often considered the standard transverse, integrating detector. However, film dosimetry required significant overhead, required meticulous care in pre- and post-handling and processing, and there was a significant delay between irradiation and readout. For this reason, a real-time detector was desired for transverse measurements.

2.3.1 ImRT Matrixx Description

The ImRT Matrixx, see Figure 21, was a commercially available 2D array of 1020 parallel plate ion chambers. The Matrixx system was composed of 1020 vented ion chambers, plastic housing, 16 on-detector TERA electrometer and accompanying IBA Dosimetry OmniPro ImRT control and analysis software.

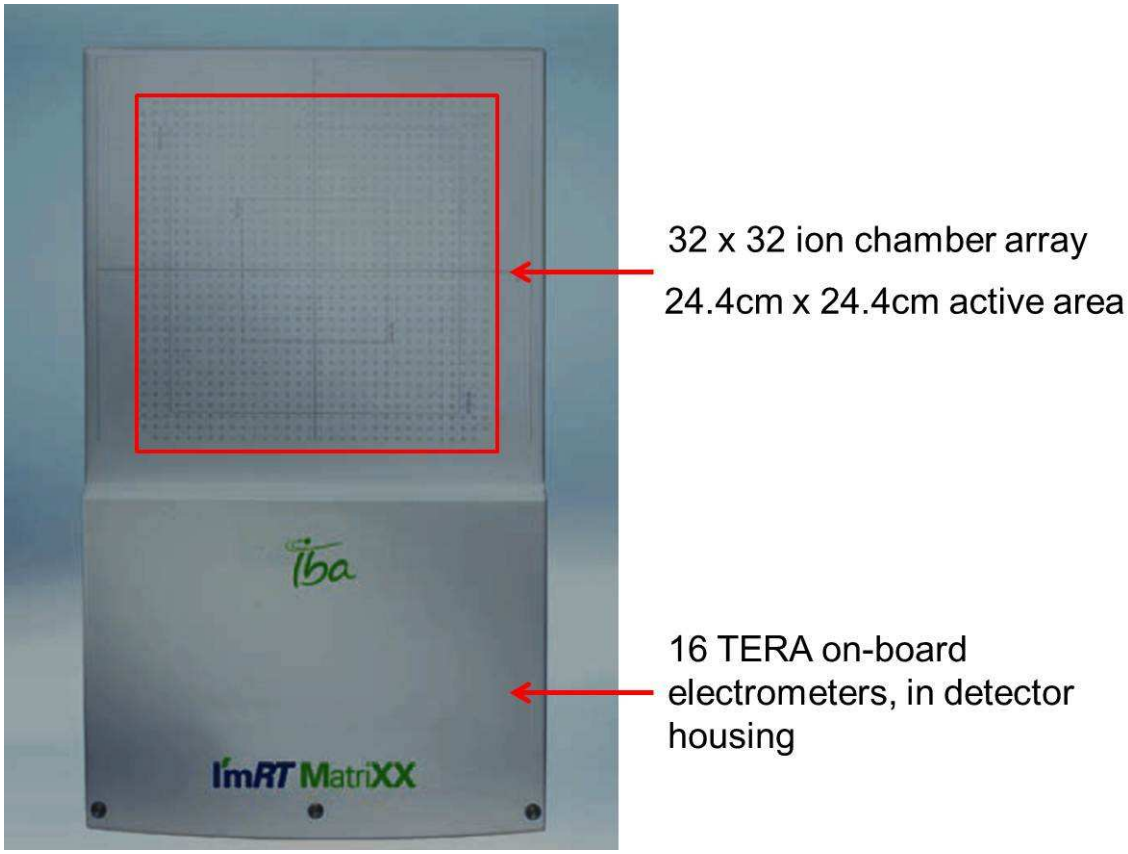

Figure 21. IBA Dosimetry ImRT Matrixx detector, with detector array and electrometer locations identified.

The Matrixx detector dimensions were 56cm long, 32cm wide and 6cm deep. The detector was approximate 10kg in weight. Though the Matrixx was heavier and bulkier

than many equivalent arrays, the added bulk was at the advantage of on-board electronics. This improved the overall detector setup time.

The 1020 ion chambers were arranged in a 2D array of 32 x 32 ion chambers. With a center-to-center chamber distance of 7.62mm, this yielded a 24.4 x 24.4 cm^2 active area. Due to detector spacing, inherent spatial sampling was limited to 7.6mm. Each ion chamber was parallel plate with diameter of 4.5mm and air gap of 5mm. The overall chamber volume was 0.08cm^3, covering an approximate 24.4 x 24.4 cm^2 active area.

The detector performance specifications were sufficient for an active uniform scanning beam environment. The dose rate response of the detector was linear between 2-2000 cGy/min. The charge response was 0.1 pC/count enabling measurements of small dose deliveries. The on-board TERA chip electrometers significantly improved the quality of the detector performance. By digitizing the signal on-board, signal degradation was essentially eliminated. This stood in contrast to the previously discussed MLIC. The signal degradation due to separation of detector and electronics was a significant issue in the MLIC detector design. The TERA chips in the Matrixx allowed for integrated or real-time readout of the signal, and the dead time for the clinical usability range was insignificant. Because the instantaneous dose rate was higher for uniform scanning than passive scattering, the improved electronics and performance were an important part of scanning beam detectors.

IBA Dosimetry OmnioPro ImRT operated as both the detector control software and data analysis package. In addition, OmniPro ImRT interfaced with a Vidar DosimetryPro film scanner, also acting as control and analysis software. The analysis package allowed for

the computation of basic single profile metrics, such as flatness, symmetry, field size, and penumbra. In addition, the software package allowed for film-to-film, detector-to-film or detector-to-detector comparative analysis. Therefore, through one software package, the Matrixx could be be benchmarked against film and commissioning data could be acquired.

2.3.2 ImRT Matrixx Calibration

The ImRT Matrixx system utilized two calibration routines. The uniformity calibration was a factory-provided calibration of each ion chamber. This calibration was similar to the gain calibration for the MLIC. The uniformity correction adjusted for the response variation of each ion chamber. These factors were supplied by IBA and applied as the default factory calibration.

In addition, the Matrixx could be cross-calibrated to report dose in centi-Gray. The OmniPro ImRT software had a cross-calibration module. The process was straightforward. The user irradiated the Matrixx with a known radiation field to a known dose per monitor unit. After irradiation, the software module correlated the charge measured using the central four ion chambers with the delivered dose and monitor units. This created a k-factor (k), which was a constant relating average collected charge to dose. After this process and with the k-factor applied, the Matrixx reported dose in addition to the relative profile dose distributions.

2.3.3 ImRT Matrixx and Film Benchmark

At the beginning of the commissioning project, the Matrixx detector did not have a demonstrated track record of performance in proton therapy center. Importantly, the detector had not been used to commission an active scanning proton beam delivery system. Prior to using the Matrixx detector, the acquired detector data were benchmarked against Kodak XOmat V (Kodak, USA) film measurements, the standard for transverse profile measurements. Using the IBA Dosimetry OmniPro ImRT software package, the analysis was performed comparing several important transverse profile parameters, including penumbra, field size, flatness and symmetry. The performance metrics, as measured with film, were the standard against which the Matrixx data was compared in order to determine its utility in the proton therapy beam.

For the benchmark measurements, both the Matrixx and film were irradiated in the same conditions, see Figure 22, and the results compared. The benchmarking was performed at the extreme of the therapeutic energy spectrum – range (ie, distal 90%) of 8.0cm and 27.0cm in water. A fixed modulation of 4.0cm was used. Three planes within the irradiated volume were measured – a proximal, central and distal plane – perpendicular to the beam axis.

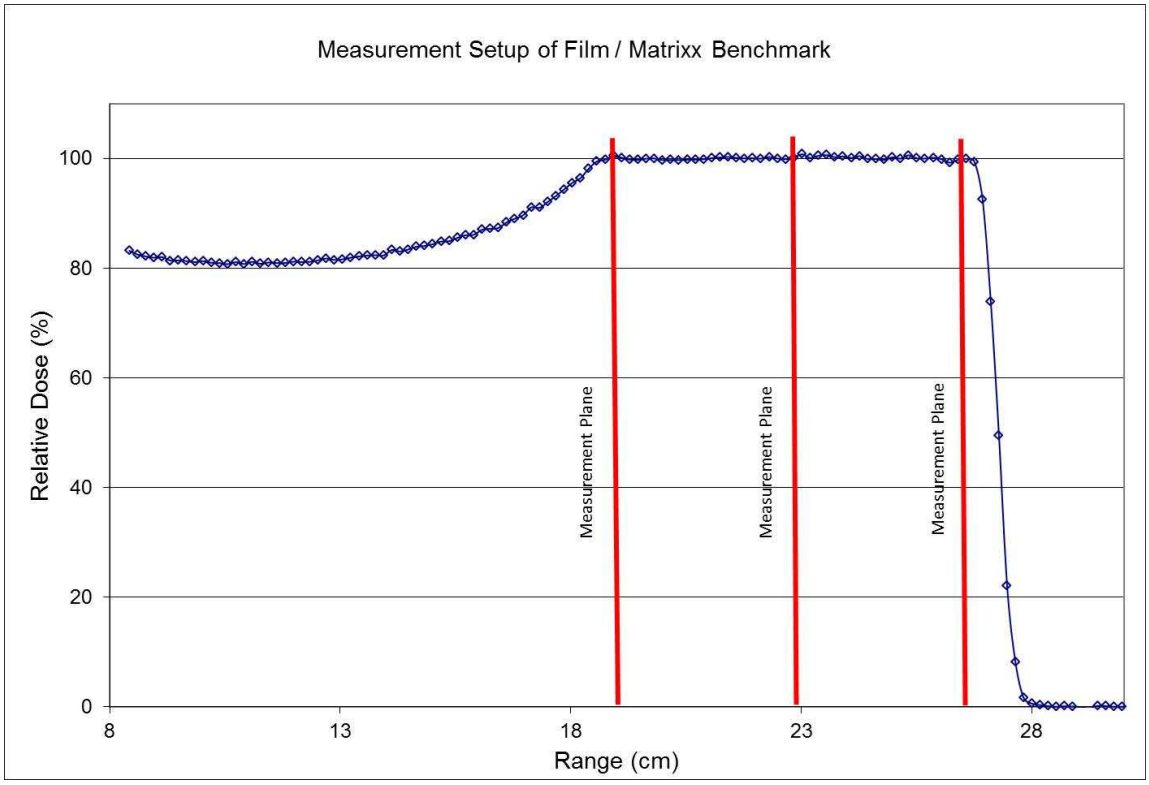

Figure 22. Measurement setup of the film and Matrixx benchmarking study. The red lines are the planes at which the film and Matrixx measurements were acquired.

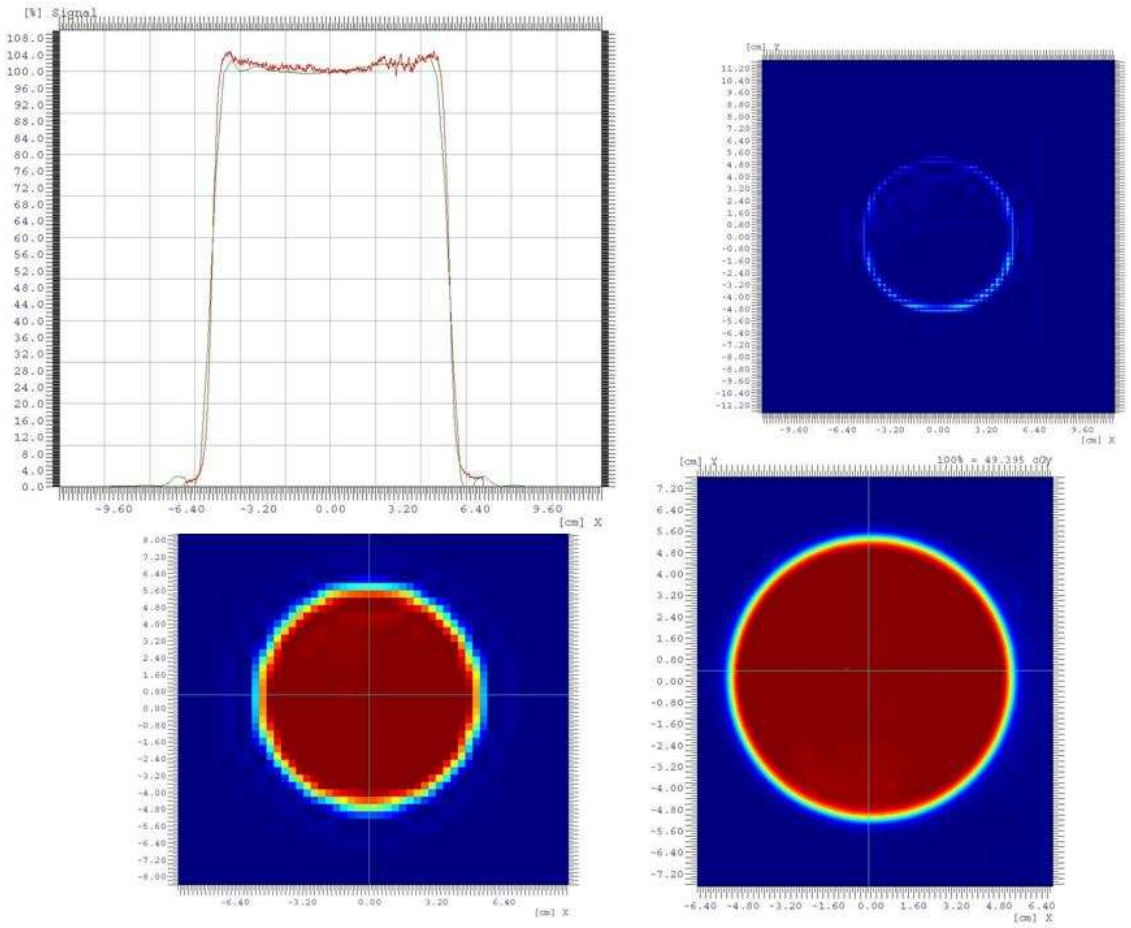

Figure 23. Matrixx (lower left), and film (lower right) and the comparison set (upper left and right). The measurements were normalized to 100% at the central axis.

The primary criteria evaluated for the benchmarking study were the penumbra and field size measurements. The penumbra was defined as the distance from the 80% to 20% dose levels along the transverse dose gradient. The measured field size was defined as the distance from 50% to 50%. Due to the coarse spatial sampling of the Matrixx detector, the penumbra was routinely overestimated, often by a factor of two. The inadequate spatial sampling, equivalent to 7.0mm detector center-to-center, under-sampled the profile, particularly in the steep dose gradient regions. By comparison, the spatial sampling of the XV film was limited to the size of the film grain, processing and

developing process, stated at approximately 0.1mm, and film scanner resolution. In regards to the field size measurement, since both the film and Matrixx were normalized to 100% at the central axis, the 50% isodose level is not as affected. The gradient of the fall off is more affected than the full-width-half-maximum (i.e. the field size).

The secondary criteria for evaluated for the benchmarking study were the flatness and symmetry indices. The flatness was a performance metric based on the relative dose uniformity in a dose reference volume. The dose reference volume for these data was the central 80% of the transverse profile. The flatness calculation was based the maximum and minimum dose differences within the dose reference volume, reflected in the following formula:

$$Flatness = \frac{\left|D_{\max} - D_{\min}\right|}{D_{\max} + D_{\min}} \times 100$$

Figure 24. Flatness equation.

The symmetry calculation was based on the comparison of the area under the profile on both sides of the central axis with a dose floor of 50%, reflected in the following formula:

$$Symmetry = \frac{\left|Area_{left} - Area_{right}\right|}{Area_{left} + Area_{right}} \times 100$$

Figure 25. Symmetry equation.

The flatness and symmetry, as measured by film and the Matrixx detector, met the specification of the uniform scanning system within +/- 3%.

Based on the results, for the purposes of optimizing and characterizing the uniform scanning system, film should be used for detailed, quantitative characterization of penumbra and field size. The Matrixx detector measurement of penumbra and field size were too coarse to adequately characterize the penumbra and field size, especially in the case of small field size and narrow penumbra. The Matrixx detector could be used for flatness and symmetry measurements with no loss in data quality and a substantial improvement in measurement efficiency. Furthermore, the Matrixx detector could be used for reproducibility and constancy measurements and studies. Flatness and symmetry could be analyzed using either the Matrixx detector or film.

2.3.4 1D Water Phantom and Holder Adaptation

Due to the common installation of horizontal fixed beamline (FHBL) treatment rooms in proton therapy, the standard, commercially available 1-dimension scanning water tanks are often not used. Due to the FHBL design, in-water profile measurements are performed with the beam oriented horizontally, therefore entering the scanner through the tank wall. This is different than the common practice in photon therapy where the measurements are often conducted at 0 degrees, delivering through the water surface. Furthermore, because the dose reference volume varies by modulation width, range and field size, there are many combinations of potential depth dose and transverse profiles that could be measured. During the optimization and characterization process, it is critical to measure at the extents of the dose reference volume, i.e. at the proximal, and distal planes, and somewhere near the center of the volume. Due to these requirements, for the optimization and commissioning project, I adapted a commercially

available 1D scanning water tank for measuring transverse profiles using the Matrixx detector at any water equivalent depth.

The Water Phantom 1-D (WP1D) (IBA Dosimetry, Germany), see Figure 26, was a standard 1-dimensional scanning water phantom. The precision of the translational motor assembly was 0.1mm. The WP1D was commercially available and primarily used for absolute calibration of photon or proton beam delivery systems. The physical components and control and analysis software (OmniPro ImRT) were not changed. Those key components did not require modification.

Figure 26. Water Phantom 1-Dimension (WP1D). Photo courtesy of IBA Dosimetry, WP1D manual.

In order to retrofit the WP1D for the purposes of acquiring transverse profiles, three main items were addressed. First, the 1D translational drive assembly was rotated by 90 degrees and remounted to the water tank. This required designing a simple jig to hold

the drive assembly. Second, a water-tight holder was designed for the Matrixx detector. This allowed the Matrixx detector to be partially submerged in the water tank. Third, a connection was established between the drive assembly and the water-tight holder. This allowed the Matrixx to be driven to any depth within the water tank along the drive assembly. The final system is displayed in Figure 27.

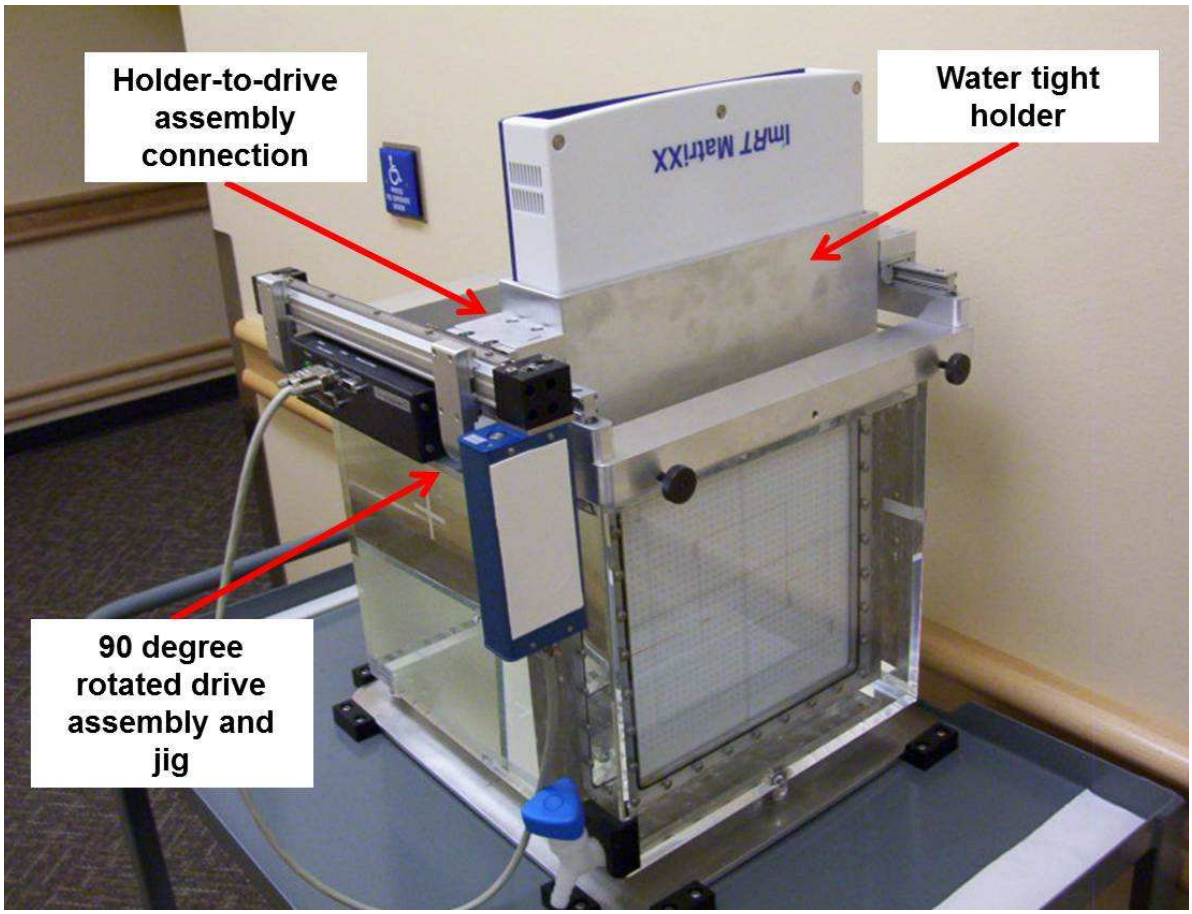

Figure 27. 1-dimensional scanning water phantom (WP1D) with 90 degree drive assembly rotation, water tight holder and mounting jig, therefore, completing the retrofit and allowing the Matrixx detector to acquire transverse profiles at any depth in water.

The modified WP1D significantly improved the efficiency of acquiring multiple transverse profiles at depth in water. The typical method of acquiring a transverse profile with film or Matrixx at a water equivalent depth simulated by using solid water was replaced by true measurement in water. The modified WP1D was remotely controlled from the external control room using OmniPro ImRT, which was the acquisition and analysis software. Also, by operating the water phantom remotely, the need for routine measurement setup modifications (e.g. by adjusting the thickness of solid water in front of the detector) was eliminated. However, the modified system did have some disadvantages. The main disadvantage was the hindered venting of the ion chambers. The Matrixx was composed of 1020 vented ion chambers. Furthermore, because the electronics were placed on-board, small on-board exhaust fans were used to mitigate the heat build and encourage the venting of the ion chambers. Also, the heat was generated and dissipated from one end of the detector. By placing the Matrixx detector in a water tight jig, open only at one end, there was a demonstrable drift of the signal over time (i.e. 0.5 hour and larger). For practical purposes, relative measurements were impacted less than absolute or cross-calibrated dose measurements.

2.3.4.1 IBA Dosimetry DigiPhan

In 2008, IBA Dosimetry designed and fabricated a holder for the Matrixx detector based on the design implemented at Indiana University. IBA Dosimetry created the “DigiPhan”, a translational motor-driven, water-tight jig for the Matrixx detector for use in the commercially available 1D scanning water phantom. During that collaboration, I provided design feedback and tested the commercially available product.

3 Binary Range Modulator Optimization and Characterization

3.1 Introduction

All therapeutic proton beam delivery systems manipulate a near-monoenergic proton beam from an accelerator in order to create a large therapeutic proton field. The near-monoenergetic proton beam is modulated in both the plane perpendicular to the beam and the beam axis. The uniform scanning system has two major components – the binary range modulator and the wobbling magnet. In this chapter, the optimization and characterization of the binary range modulator is described.

The binary range modulator (BRM), Figure 28, is a nozzle component downstream of the wobbling magnet (discussed in detail later) but upstream of the primary monitor chamber, aperture and compensator. The primary role of the BRM is to modulate the proton beam along the beam axis, or, in other words, to construct a spread out Bragg peak by layer or energy stacking pristine peaks. The BRM is composed of 6 plates– 2 Lucite and 4 graphite– of varying thicknesses. The plates are arranged in a binary fashion with the following water equivalent thicknesses – 3.0mm, 6.0mm, 12.0mm, 24.0mm, 48.0mm, 96.0mm. Each plate can be pneumatically driven into the proton beam pathway in any binary combination. By using different combinations of the six plates, any spread out Bragg peak can be created from a modulation width of a 2.0cm to 27.0cm, limited by the maximum energy of the cyclotron.

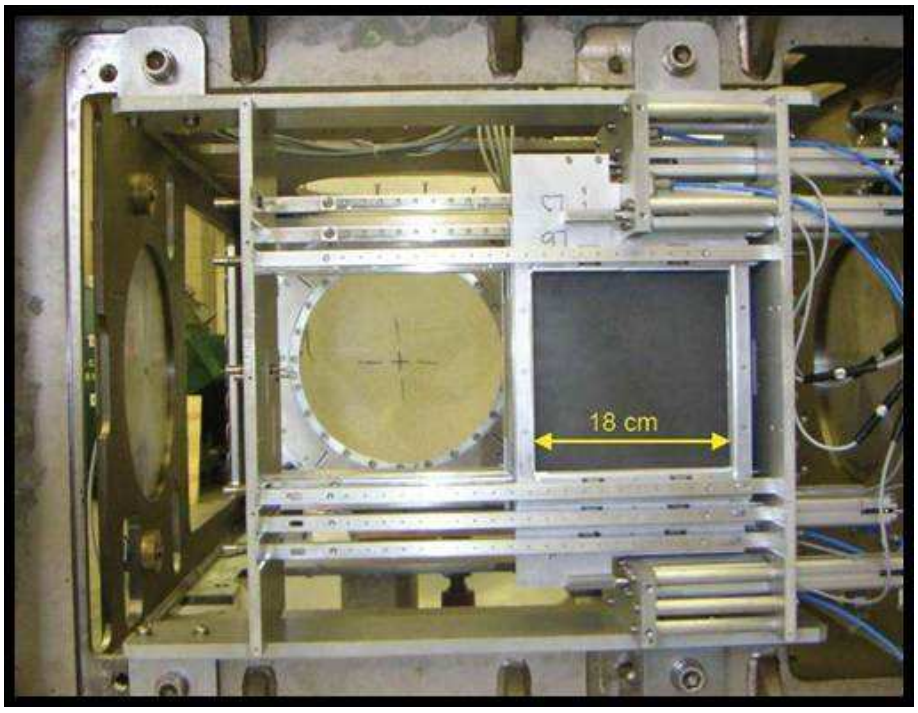

Figure 28. Beam's eye view of binary range modulator as installed in the uniform scanning nozzle.

3.2 Materials and Methods

Through the dose delivery system (DDS) which controls the uniform scanning nozzle, the binary range modulator control system utilizes a layer definition file (LDF) in order to create SOBPs. The SOBP is constructed by a series of pristine peaks with predefined weights. Each LDF is a specific file within a given clinical range of energies and a certain weight per layer, yielding a specific SOBP width. The LDF is determined through a hybrid empirical-analytical process, using pristine Bragg peak data, layering and finding the best weight to produce a flat SOBP, then verifying and "tweaking" the weights for best in-room results. After installation, the BRM was functional but the LDFs were not created or optimized so therapeutically relevant proton fields were not deliverable. I

was responsible for creating, optimizing and validating the layer definition files. A subset of the results is contained in publication[34].

The layer definition files (LDF) had a specific format. Each LDF started as a ".dat" file. The .dat file had a specific naming convention that allowed the DDS to interpret and translate the contents of the file. The title of the .dat file correlated to a clinical range spectrum and modulation width. For example, see Figure 29, "RNG0B_SOBP100_Layers.dat" translated to a .dat file for a SOBP width of 10.0cm in the clinical range spectrum between 6.0cm and 12.0cm range in water.

Range (cm)	LDF Title
6.0cmn - 12.0cm	RNG0B_SOBPXXX_LAYERS.ldf
12.0cm - 20.0cm	RNG0D_SOBPXXX_LAYERS.ldf
20.0cm - 27.0cm	RNG0F_SOBPXXX_LAYERS.ldf

Figure 29. Layer definition file title specifications, where "B", "D", "F" stand for low, medium and high energy and "XXX" stands for modulation width in millimeters.

This .dat file was a simple ASCII text file, tab delimited, see Figure 30. Each layer was a separate row in the .dat file, with layer 1 being the most distal layer, layer 2 being the abutting proximal layer, and so forth. The .dat file weights were arbitrary number strings in the text file. However, as a default, the first layer was always weighted "0.9280". This was by design and regarded as a safety feature, prohibiting accidental tampering. The remaining weights were always less than 0.9280.

RNG0D_SOBP100_Layers.dat

1	0.9280
2	0.3364
3	0.2494
4	0.2001
5	0.1711
6	0.1450
7	0.1276
8	0.1160
9	0.1073
10	0.0986
11	0.0928
12	0.0870
13	0.0812
14	0.0754
15	0.0812

Figure 30. Example of layer .dat file for medium energy (12.0cm to 20.0cm) and 10.0cm SOBP width.

When the .dat file was finalized, a simple script converted the .dat file to a .ldf file. This process has two major operations. First, the .dat file weights were converted from an arbitrary number string to a layer weight in the form of a percentage. For example, compare Figure 30 and Figure 31, layer 1 was converted from the arbitrary 0.9280 to 0.3200 (or 32.0%). Layer 2 was converted from 0.3364 to 0.1160 (or 11.6%). This percentage allowed the clinician to more intuitively interpret the layer definition file as displayed on the treatment console, which improved the overall safety and openness of the treatment system. Second, using the new percentage .ldf file, a checksum was computed and converted to hexadecimal. This hexadecimal number was stored in the treatment console database. Prior to each treatment, the treatment console computed the file checksum for the loaded .ldf and compared it to the official checksum computed

during commissioning. If the checksums did not match, the treatment could not be delivered.

RNG0D_SOBP100_Layers.ldf

1	0.3200
2	0.1160
3	0.0860
4	0.0690
5	0.0590
6	0.0500
7	0.0440
8	0.0400
9	0.0370
10	0.0340
11	0.0320
12	0.0300
13	0.0280
14	0.0260
15	0.0280

Figure 31. Example of .ldf file for medium energy (12.0cm to 20.0cm) and 10.0cm SOBP width.

The MLIC (described in Chapter 2.2.2) was used to validate the layer definition files. The initial validation was gathered, followed by a reproducibility test. Once validated by measurement, the .dat files were converted to .ldf files and that specific SOBP was deemed “validated” and then commissioned in the treatment planning system.

3.3 Pristine Peak Characterization

Regardless, of the beam delivery system, an SOBP was composed of layered pristine peaks. Therefore, the characterization of the pristine peaks was important in determining the requisite number of layers, the layer spacing and the layer weight. For example, a broader pristine peak could allow a coarser layer spacing and by extension a reduction in the total number of layers for a given SOBP width. Therefore, prior to creating .dat or .ldf files, a pristine peak characterization was performed. The pristine peak characterization study served two main purposes. First, the calibration of the energy selection line degrader was required to correlate a given degrader setting with a specified range in water in the treatment room. Second, the map of pristine peak width, specified by the full-width half-maximum (FWHM) with respect to the range in water, was required for determining the initial layer spacing and weighting.

Pristine Bragg peak percentage depths doses were the first measurements required for commissioning the binary range modulator. This group of measurements was used for both validating the range in water in the treatment room due to the calibration of the degrader and quantifying the pristine peak full width half maximum. The MLIC was used to measure the pristine peak depth doses for a sampling of ranges between 6.0cm and 27.0cm range in water. The MLIC was indexed to the patient positioning system and the face of the MLIC was aligned to the isocenter plane. The depth-dose profiles were measured and converted to percentage depth dose profiles by normalizing the peak maximum to 100%. The results were then tallied according to the specific metric and goal.

3.3.1 Pristine Peak Range in Water Validation

The calibration and validation of the energy selection line degrader settings and the range in water in the treatment room was critical. In the treatment beamline, the degrader setting was established according to the range upstream of the nozzle as measured using the Multi Layer Faraday Cup (MLFC). The MLFC is a common tool in proton therapy, consisting of alternating copper and Kapton, an insulator, plates. The proton beam loses protons in each plate, thereby inducing a charge collection per plate. This charge collection as a function of plate water equivalent depth is used to measure the range. The MLFC measured range is then correlated to the range measured in the treatment room by the MLIC. Because an SOBP does not exist upstream of the nozzle, the range in water is established using pristine peaks.

The range required in the treatment room was requested through the Beam Delivery System (BDS). The BDS requested range was translated to a specific degrader setting. The residual range transmitted through the degrader was then measured by the MLFC. For a subset of ranges across the clinical spectrum, from 6.0cm to 27.0cm range, the beam was requested through BDS and delivered on a beam stop containing the MLFC. The MLFC reported the range at the distal 80% of dose. In order to verify the degrader is producing the range requested, the requested range and MLFC measured range were compared, see Figure 32. The maximum difference in requested and measured range was 0.8cm. The average difference was 0.02cm. The differences were generally larger at the extremes of the clinical spectrum. This was a byproduct of the fact that the BDS was calibrated at range 16.0cm, which was the center of the clinical spectrum. The degrader calibration was within the overall uncertainty of treatment delivery system.

BDS Range (cm)	MLFC Range (cm)	Range Difference (cm)
27.0	27.08	0.080
24.0	23.96	-0.040
22.0	21.94	-0.060
20.0	19.95	-0.050
19.0	18.98	-0.020
16.0	15.97	-0.030
13.5	13.50	0.000
12.0	11.98	-0.020
11.0	10.99	-0.010
8.5	8.48	-0.020
6.0	5.98	-0.020

Figure 32. The requested range and measured range, upstream of the nozzle in the MLFC.

Because properly calibrated range in the treatment room was the desired endpoint, the upstream range measurement in the MLFC was correlated to the downstream range in the treatment room. For the same ranges, the MLIC was used to measure the pristine depth dose and the range at the distal 80%. Both the MLFC and MLIC correlate within 0.07cm. The average difference was 0.02cm.

MLFC Range (cm)	MLIC R80 (cm)	Range Difference (cm)
27.08	27.12	0.040
23.96	23.96	0.000
21.94	21.95	0.010
19.95	19.95	0.000
18.98	18.96	-0.020
15.97	15.96	-0.010
13.50	13.48	-0.020
11.98	11.95	-0.030
10.99	10.96	-0.030
8.48	8.42	-0.060
5.98	5.91	-0.070

Figure 33. The MLFC measured range and the MLIC measured range.

By plotting the upstream and downstream range measurements, the trendline fit should have had a slope of ~1.0 and an intercept of 0.0 if perfectly correlated. This plot should have represented a direct variation or 1-to-1 correlation. From the plot, see Figure 34, the slope was 1.004 and the y-intercept was -0.08. With the supporting data, the calibration of the degrader was within 0.07cm. This was within the specification of the machine. Furthermore, it should be noted that this data represented the calibration of the degrader and range in the treatment room. This does not imply a 0.08cm range offset in the treatment. This range data was used as input to the treatment planning system. Provided the degrader was properly characterized and any offset was part of the treatment planning data, no patient treatment was affected by this calibration.

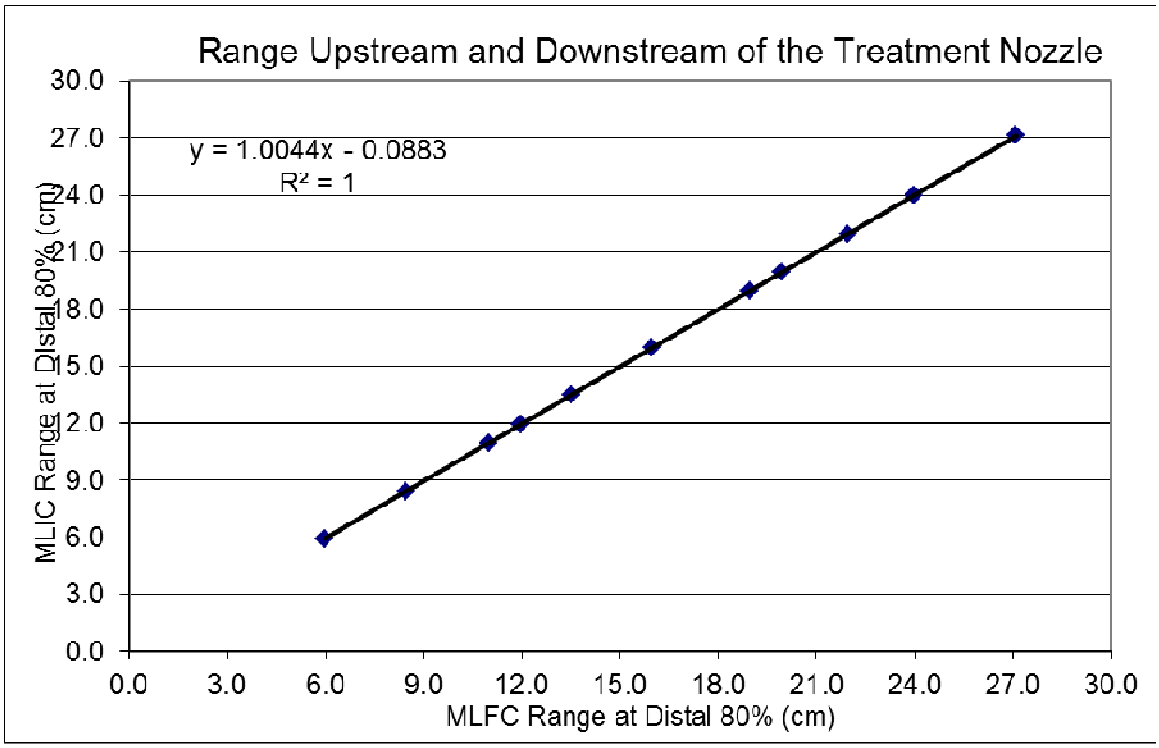

Figure 34. Correlation plot of range upstream (MLFC) and downstream (MLIC) of the nozzle.

3.3.2 Pristine Peak Full-Width Half-Maximum (FWHM) Characterization

Now that the range in the treatment room had been characterized, the energy spread, or full-width at half-maximum (FWHM) along the beam axis, was next characterized. The energy spread was a critical parameter that determined the SOBP layer spacing. As in the case of the range validation, the energy spread was measured both upstream of the nozzle in the MLFC and downstream of the nozzle in the treatment room by the MLIC for a subset of ranges that spanned the clinical spectrum.

Prior to entering the treatment nozzle, the energy spread in the MLFC was measured and validated, see Figure 35 and Figure 36. The FWHM ranges from 1.68cm at 6.0cm range in water, the shallowest clinically deliverable range, to 2.43cm at 27.0cm range in water, the deepest clinical energy. As the energy or range increased, the energy spread was increasingly dominated by multiple coulomb scattering and range straggling in the medium. This explained the increase in energy spread as a function of range. However, as shown in Figure 36, there was a stabilization of the energy spread as a function of range between 10.0cm and 20.0cm range. This was due to a device called the momentum band slits, or “slits”.

Range (cm)	ES (cm)
27	2.43
24	2.29
22	2.31
20	2.24
19	2.05
16	2.05
13.5	1.99
12	2.03
11	2.05
8.5	1.91
6	1.68

Figure 35. Tabulated data for range and energy spread (ES), both measured in water equivalent centimeters in the MLFC.

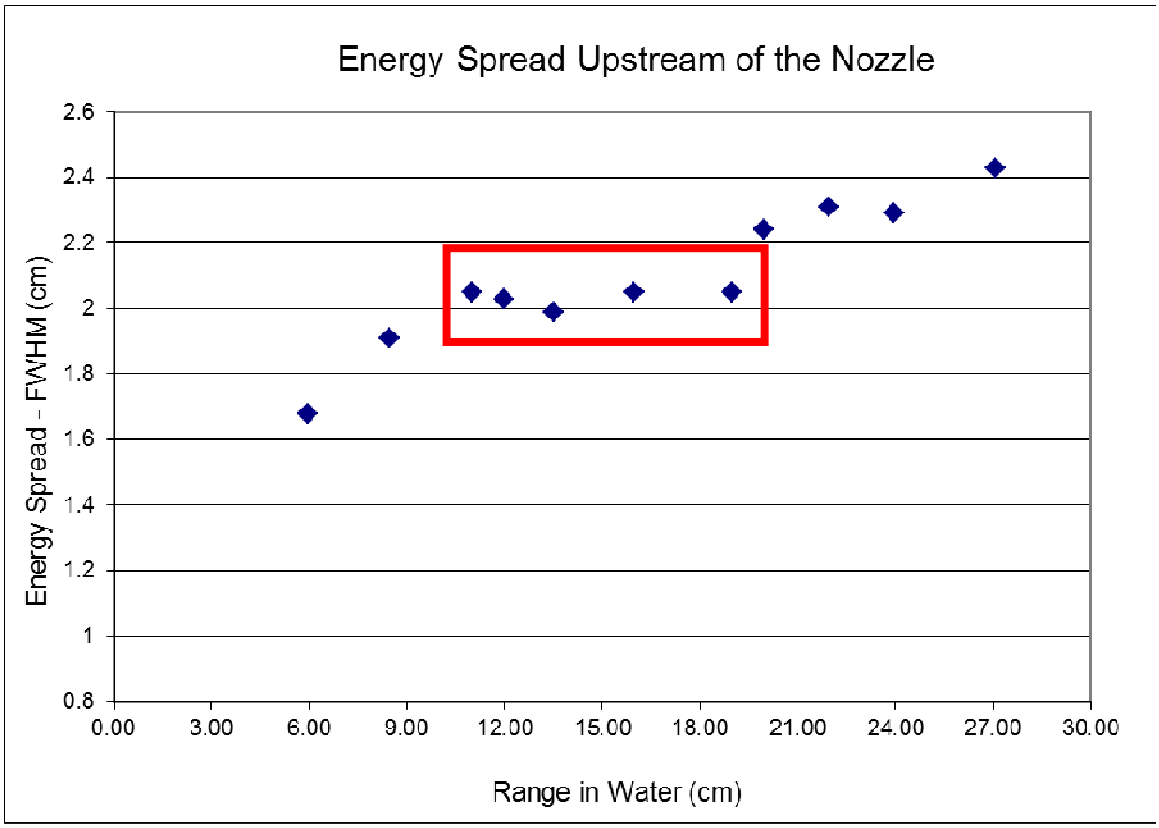

Figure 36. Energy spread, as measured by full width half maximum (FWHM), in the MLFC. The red box represents the region where the momentum band slits adjusted the energy spread in order to achieve a constant energy spread.

The energy spread in the treatment room, the clinically relevant parameter, was a function of two properties. The dominant parameter in influencing the energy spread in the treatment room was multiple coulomb scattering and range straggling in the media the proton beam traversed. This was a basic physical property and could not be modified. However, a secondary parameter that influenced the ultimate energy spread in the treatment room was the energy spread entering the nozzle. The slits, mentioned earlier, were physical devices, wedge-like pieces of metal alloy similar to a degrader, that served to trim the energy spread by removing protons at energies above or below the requested energy in the nozzle. By reducing the polyenergetic spread of the proton

beam entering the nozzle, the range straggling effect was reduced and therefore the FWHM of the proton beam along the beam axis was reduced. Also, by improving the energy homogeneity of the beam entering the nozzle, the beamline optics, magnet scanning parameters and overall efficiency were improved.

The energy spread was characterized in the treatment room. The FWHM of the pristine Bragg peak in the treatment room had a direct impact on several treatment parameters, such as layer spacing, number of layers, and SOBP uniformity. As expect, the FWHM in the treatment increased as the range in water increased, see Figure 37. When examining the correlation between the MLFC and the MLIC, the region in which the energy spread was controllable yielded an increasing function of the range in water, see Figure 38.

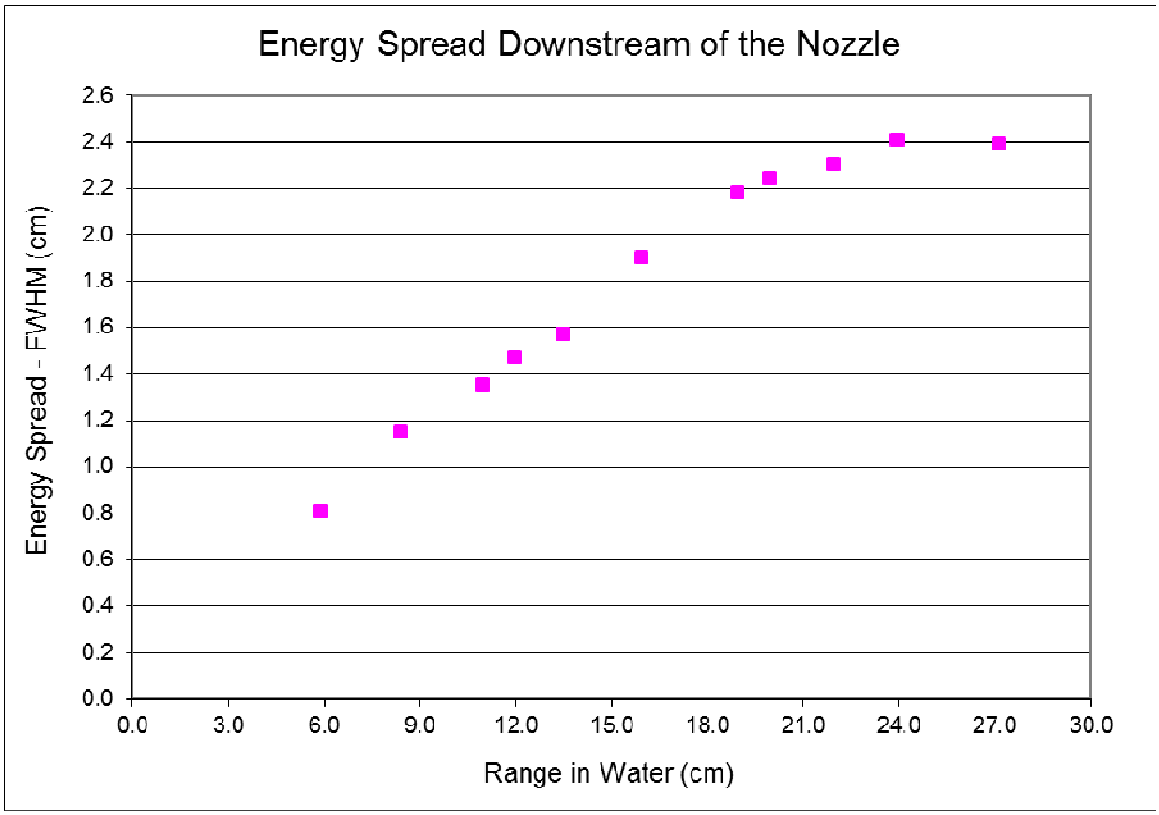

Figure 37. Energy spread (FWHM) in the treatment room measured by MLIC in water equivalent centimeters.

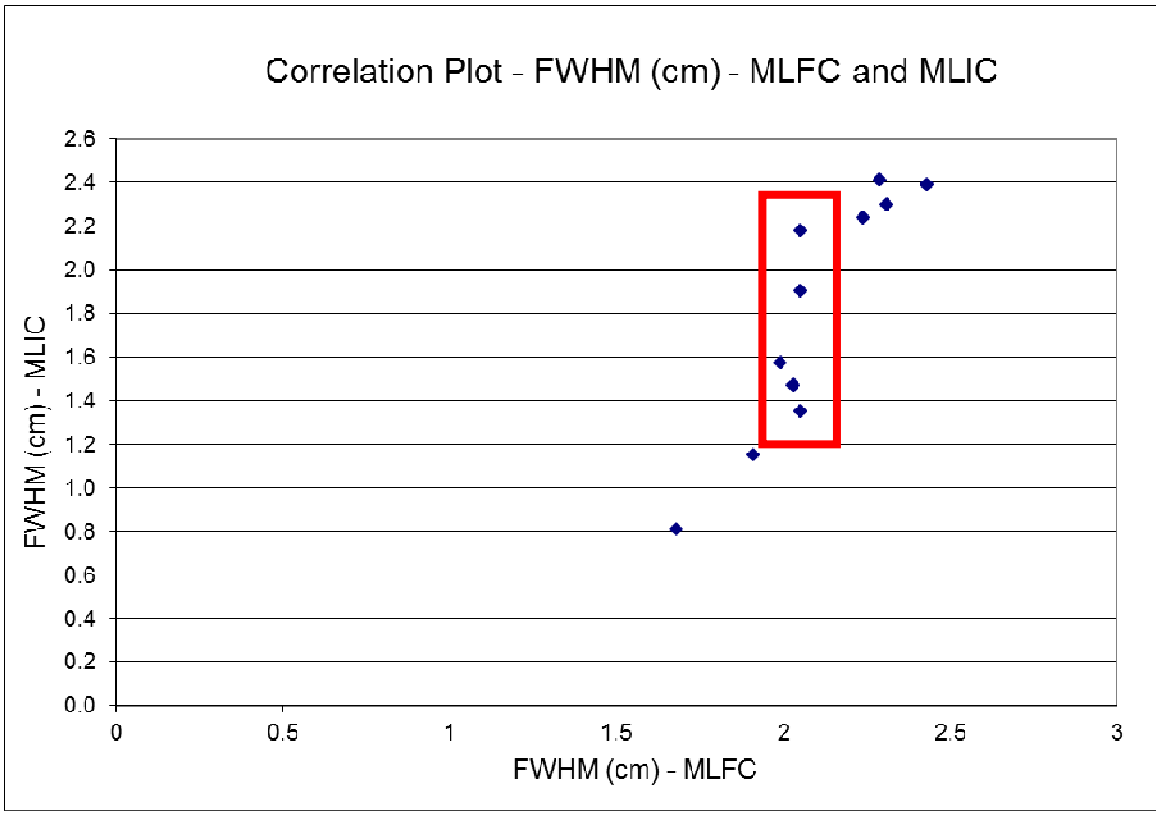

Figure 38. Correlation plot showing the impact of controlling the energy spread upstream of the nozzle on the energy spread in the treatment room. The red box is the clinical spectrum within which the energy spread can be adjusted by the momentum band slits.

Though FWHM was commonly used to characterize the Bragg peak width, it was a poor indicator of layer spacing in uniform scanning. The layers were not spaced such that the 50% isodose lines were matched. This would have resulted in severely deteriorated field flatness. The layers were spaced such that the overlap was between the 90% and 98% isodose lines. However, using FWHM or sigma to characterize the Bragg peak remained reasonable because a stable relationship existed between FWHM and the width at 90%, see Figure 39.

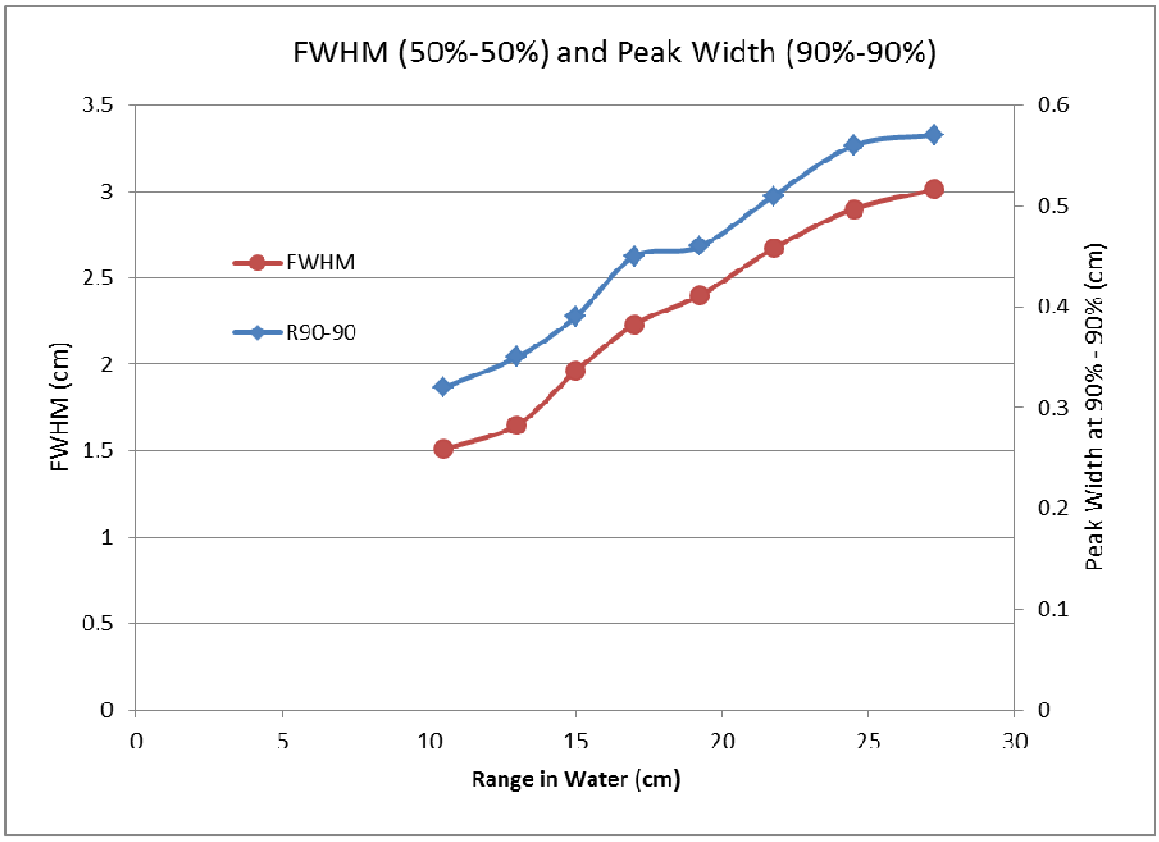

Figure 39. Trend analysis of FWHM and the width at 90%. Both metrics, though different in magnitude, represent the same trend. Therefore, either metric may be used for characterization.

3.3.3 Results and Impact

The pristine Bragg peak in the treatment room was characterized and parameterized in terms of range in water and energy spread. Based on the results, the each of the three dose delivery system (DDS) energy regimes required separate layer weights and layer spacing. Also, based on the the energy spread spectrum in the treatment room, a skewness parameter, discussed in would be introduced to correct for the tilt of the SOBP caused by the energy spread variation within the DDS energy regime.

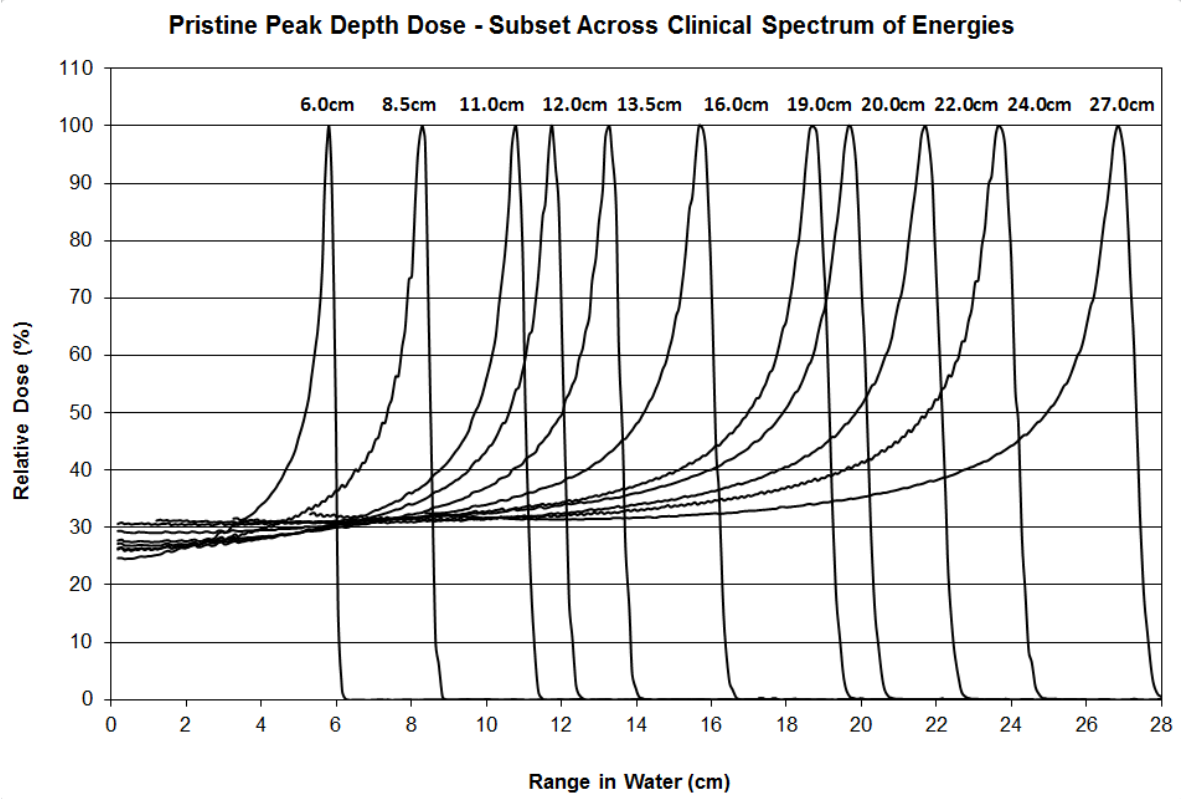

Figure 40. Subset of pristine peak data. Graph clearly demonstrates the variation of energy spread as a function of range in water. The numbers (in cm) at the peak of each depth dose is the range in water at the distal 90%.

Based on this information, the layer weight files (.dat and .ldf) were constructed. The Bragg peak characterization process yielded an initial estimate on the required layer spacing based on range in water. By using the normal distribution approximation of the Bragg peak, which was limited in its accuracy, and Bragg peak measurement, the system 90%-90% width was reduced to 3.0mm at 11.0cm range in water. Due to the design of the binary range modulator, the minimum layer spacing was either 6.0mm or 3.0mm. Based on this study, the original estimate for creating finer layers (ie, 3.0mm as opposed to 6.0mm) was at an 11.0cm range in water.

Without a detailed Monte Carlo simulation in the treatment nozzle, the layer spacing estimate was only a starting point. The characterization process had limitations. For low energy beams having sharp Bragg peaks, the spaital sampling of the detector limited the measurement precision. Measuring the FWHM of the Bragg peak and relating this to the standard deviation only provided a rough estimate as the Bragg peak could not be well approximated using a single Gaussian fit. The final optimization was accomplished empirically through iterative modification and measurement.

3.4 Layer Definition File Creation, Optimization and Validation

In creating the initial layer definition files, I established a common workflow for each DDS energy regime, with exceptions based on specific charcteristics of that particular energy regime, such as range of the energy regime and variation and size of the energy spread within that region.

Based on the characterized data, a non-commercial, third party software BGWare (Harvard University, Boston, MA) was used to create an initial pass layer definition file. This software had been used to create fixed range modulator wheels in the fixed beamline line, passiver scattering treatment rooms. The software used a single representative pristine Bragg peak depth-dose in order to calculate the layers and weights for a given spread out Bragg peak. Though useful and efficient, the software had several drawbacks. The use of a single Bragg peak was insufficient to achieve optimal field flatness and uniformity due to the energy spread variation. Also, BGWare was not designed for a uniform scanning environment or a binary range modulator. The primary difference between a range modulator wheel and a binary range modulator was

layer spacing. The modulator wheels had variable layer spacing because they were custom-fabricated per modulation width. The BRM had fixed layer spacing for all modulation widths.

A “master” layer definition file (LDF) was created using BGWare. Typically, this master file contained the layers and weights for the maximum modulation achievable or desired for a particular energy regime. The master LDF was then loaded into the dose delivery system and tested at the conditions within the energy regime that most closely matched the data loaded into BGWare. In each energy regime, a specific pristine peak was considered the “definition energy”. In other words, at a particular energy, the LDF was defined, and all other energies would use the same LDF. Though this simplified the dose delivery system software architecture, it introduced the need for a skewness paramters, discussed in Chapter 3.6.2.

The LDF was measured using the MLIC and then modified based on the results. The modifications were a manual and iterative process based on the results of the measurement. For example, if a particular part of the SOBP had a peak or valley, I would manually open the LDF, modify the corresponding or abutting layers and weights in the LDF, then remeasure the new, modified LDF. This process continued until the LDF produced an SOBP of the desired width with appropriate field uniformity.

With a flat, maximum modulation width LDF created and validated, all remaining SOBPs would be created from this master file. Systematically, one or two layers were removed from the LDF and a new file created. In Figure 41, the progression from the maximum LDF to each subsequent LDF is demonstrated. The modulation width of 14.3cm was the

maximum LDF for the medium energy regime. By removing one or two layers and creating a new LDF, a new modulation width was created. By following this process, the SOBP uniformity for all subsequent modulation widths was estimate according to the master LDF. Each new LDF was then individually validated.

Modulation Widths	14.3cm	13.1cm	12.3cm	11.4cm	10.5cm	10.0cm	9.0cm	.....
Layer Number	Relative Weight							
1	0.281	0.307	0.312	0.299	0.313	0.32	0.329	.....
2	0.113	0.084	0.088	0.109	0.114	0.116	0.12	.....
3	0.077	0.08	0.081	0.081	0.084	0.086	0.089	.....
4	0.059	0.06	0.061	0.064	0.067	0.069	0.071	.....
5	0.049	0.052	0.05	0.054	0.057	0.059	0.06	.....
6	0.042	0.046	0.046	0.047	0.049	0.05	0.052	.....
7	0.039	0.04	0.04	0.041	0.043	0.044	0.045	.....
8	0.036	0.036	0.037	0.037	0.039	0.04	0.041	.....
9	0.033	0.032	0.033	0.034	0.036	0.037	0.038	.....
10	0.03	0.029	0.03	0.031	0.033	0.034	0.035	.....
11	0.027	0.028	0.028	0.029	0.031	0.032	0.032	.....
12	0.028	0.025	0.027	0.028	0.030	0.03	0.031	.....
13	0.024	0.024	0.025	0.026	0.028	0.028	0.029	.....
14	0.025	0.024	0.024	0.024	0.026	0.026	0.028	
15	0.022	0.023	0.025	0.024	0.024	0.028		
16	0.022	0.023	0.023	0.025	0.028			
17	0.023	0.022	0.023	0.025				
18	0.024	0.022	0.022	0.025				
19	0.021	0.022	0.022					
20	0.026	0.023						

Figure 41. Table showing the progression of layer definition files from the maximum modulation width and each subsequent modulation width.

3.5 High Energy Characterization and Validation

The high energy regime, i.e. range in water from 20.0cm to 27.0cm, was the first characterized and validated region within the dose delivery system. This regime was chosen for practical purposes. The regime was relatively small, spanning only 7.0cm water requivalent range. The energy spread within in the region was relatively large, i.e.

greater than 2.0cm FWHM, and the variation was relatively small, i.e. less than 0.4cm. This energy regime also served a large number of patients and therefore had the highest clinical impact.

	Number of Layers	SOBP Width (cm)
High Energy Regime: 20.0cm - 27.0cm	4	2.2
	5	2.8
	6	3.5
	7	4.1
	8	4.8
	9	5.5
	10	6
	11	6.7
	12	7.5
	13	8
	14	9
	15	10
	16	10.5
	17	11.5
	18	12.5
	19	13.5
	20	14.5

Figure 42. Summary of available modulation widths in the high energy regime from 20.0cm to 27.0cm range in water.

The master LDF was created and optimized for modulation width and uniformity at 27.0cm range using the process outlined in Chapter 3.4. The final LDF was validated using MLIC measurements, see Figure 43. In the figure, the measured doses appeared to increase at the shallow end, but this was not physical, but was due to in-scatter from a block of solid water used to reduce the maximum energy of the depth dose to a range in water measureable by the MLIC. As noted in the detector chapter, the MLIC was

used for measuring water equivalent ranges of 22.0cm or less. In other cases, a solid water block was used to allow the MLIC to measure high energy beams. The modulation extent measured 14.9cm and the field uniformity measured 1.63%. Both metrics were within specification, and therefore, the LDF was accepted and used for creation of the remaining modulation widths in Figure 42.

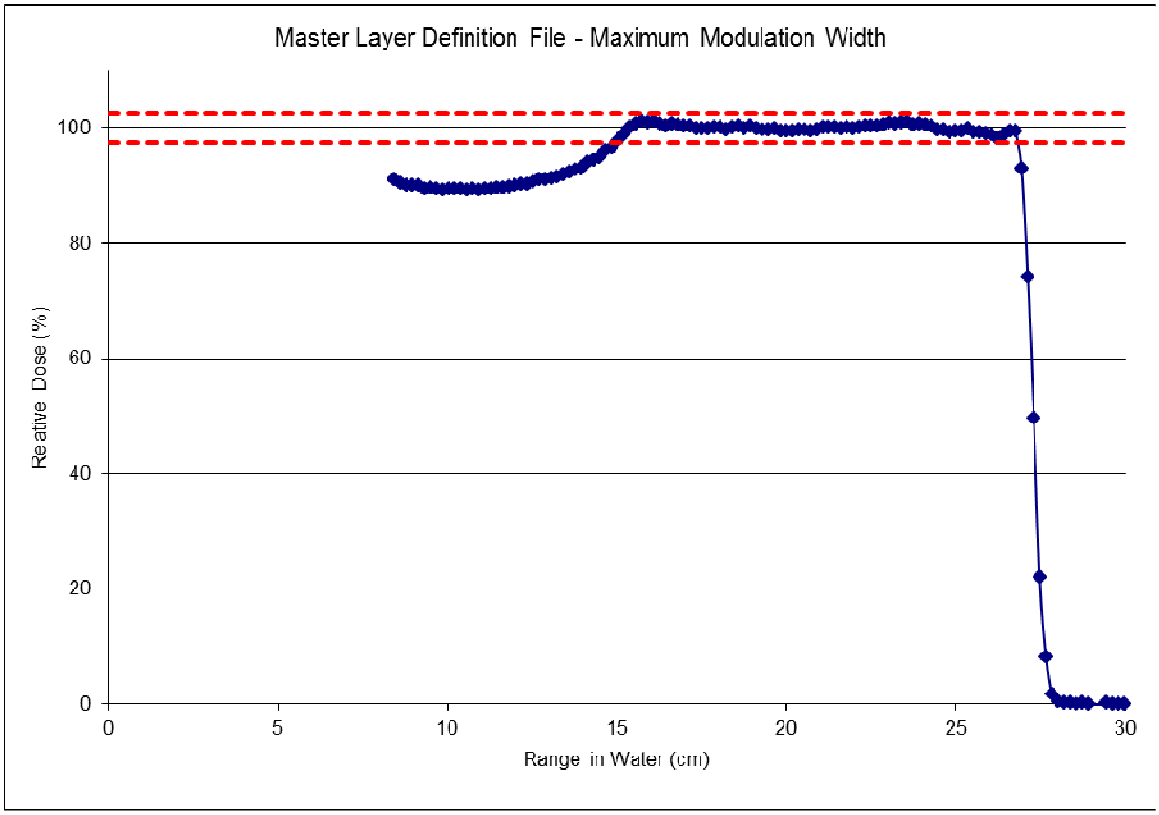

Figure 43. The depth dose measurement validating the master LDF at maximum modulation extent for the high energy regime. Dashed red lines are +/-2.5%.

All subsequent LDFs were created in the dose delivery system. The MLIC was used to validated the modulation extent and field uniformity of each LDF. Once validated, the LDF was officially accepted and commissioned in the dose delivery system. A subset of the depth doses are shown in Figure 44.

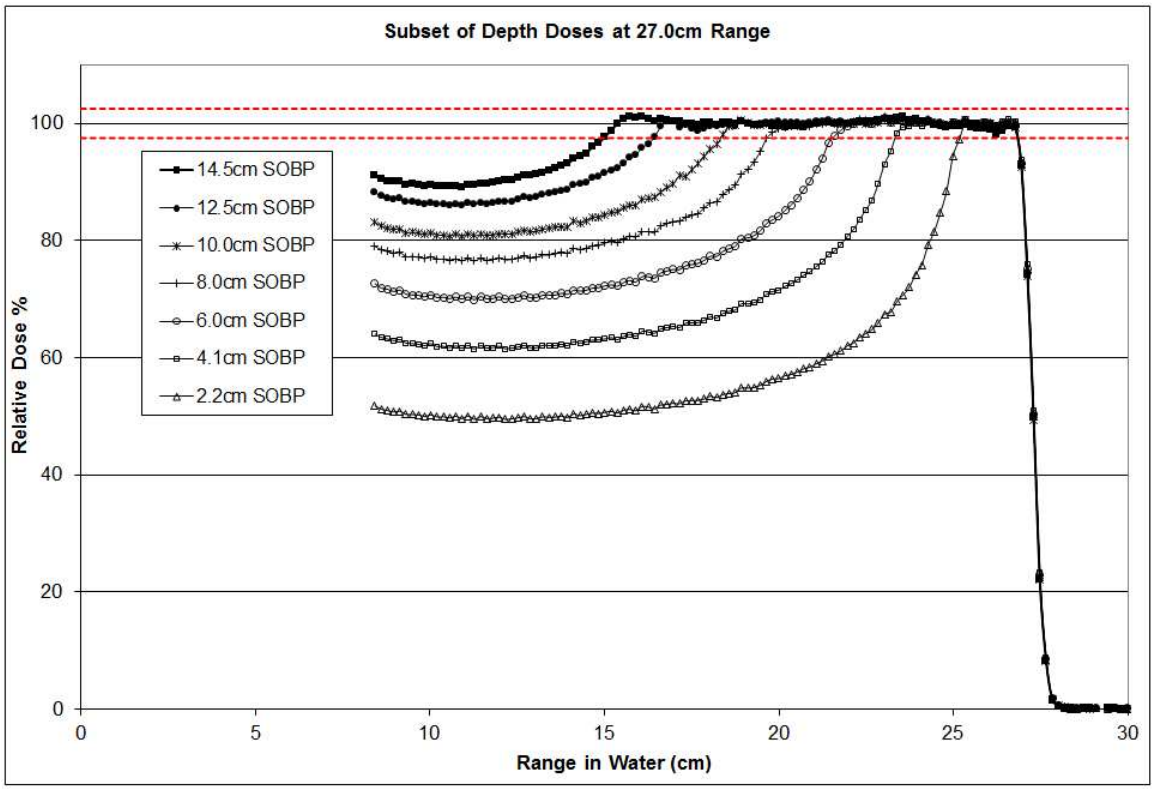

Figure 44. Subset of depth doses commissioned in the dose delivery system for the high energy regime, measured at 27.0cm range in water. Dashed red lines are +/-2.5%.

Because the LDFs were created and validated at the definition range of 27.0cm, further validation was required at the other extreme of the energy regime, i.e. 20.0cm. From 27.0cm to 20.0cm range in water, the energy spread expressed as FWHM changed from approximately 2.4cm to 2.0cm. This change in energy spread was relatively small but had the potential to change the slope, uniformity or extent of the validated LDFs. As shown in Figure 45, the slope of the SOBP was skewed due to the reduction in energy and energy spread. However, the modulation uniformity was within the +/- 2.5% specification.

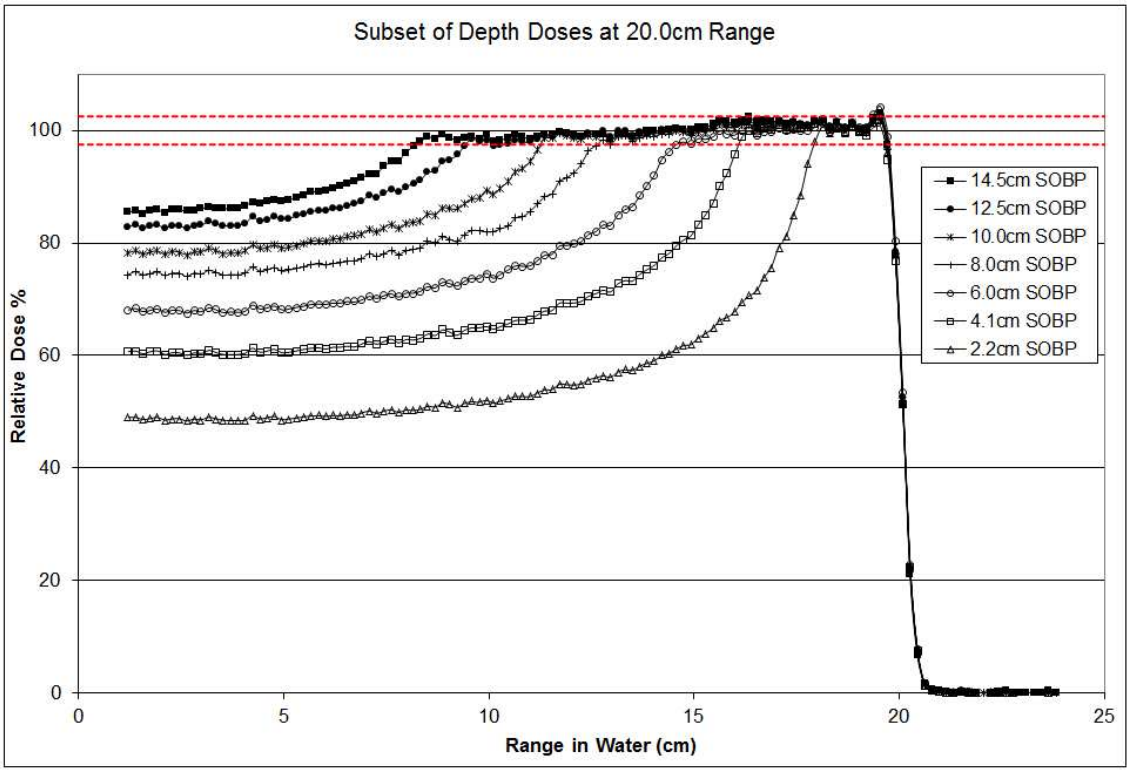

Figure 45. Subset of depth doses commissioned in the dose delivery system for the high energy regime, measured at 20.0cm range in water. Dashed red lines are +/-2.5%.

Because the depth-dose profiles were within the clinical specification, the longitudinal profiles were accepted. Furthermore, the treatment planning system would reflect the slight slope and the resulting dose distributions would meet clinical needs.

The next step was to evaluate the reproducibility of the longitudinal profiles, see Figure 46. This was done by measuring each modulation width on five separate days. The nominal SOBP widths were within 0.13 cm for all SOBPs except the largest 14.5 cm modulation width, which measures 0.39 cm larger than the nominal. The standard deviation was less than 0.06 cm for all SOBPs, except the largest, 14.5cm, modulation

width, which had a standard deviation of 0.10cm. The maximum modulation flatness for each SOBP was less than 2.0%.

Nominal SOBP Width	Average (cm)	Standard Deviation (cm)	Percent Standard Deviation	Flatness (%)
2.2	2.13	0.01	0.47	1.14
2.8	2.79	0.01	0.25	1.16
3.5	3.46	0.01	0.29	1.31
4.1	4.13	0.02	0.37	1.50
4.8	4.79	0.02	0.43	1.24
5.5	5.51	0.05	0.91	1.19
6.0	6.07	0.02	0.25	1.38
6.7	6.70	0.01	0.15	1.78
7.5	7.39	0.06	0.74	1.86
8.0	8.16	0.05	0.61	1.54
9.0	9.10	0.06	0.61	1.29
10.0	9.91	0.04	0.38	1.07
10.5	10.46	0.02	0.15	1.11
11.5	11.47	0.03	0.28	1.07
12.5	12.48	0.01	0.08	0.93
13.5	13.44	0.06	0.45	1.29
14.5	14.89	0.10	0.64	1.63

Figure 46. Table of nominal SOBP width (cm), standard deviation and flatness (%) reproducibility study.

The nominal SOBP width as a function of energy regime extrema was also quantified. Each longitudinal profile was measured at the maximum and minimum of the energy regime – 27.0cm and 20.0cm range in water. The results are reported in Figure 47. The magnitude of the difference of the measured SOBP widths increased as the SOBP width increased. As the SOBP width increased, the entrance dose of the longitudinal profile approached 90%, which was the proximal modulation width definition point.

Furthermore, as the SOBP width increased, the entrance region dose gradient became shallower. For a large SOBP, a 1.0% change in dose corresponded to a 1.0cm change in the depth of the proximal 90%. According to Figure 47, although the 14.5cm nominal SOBP width measured width varied by 1.2cm from range in water 27.0cm to 20.0cm, the entrance dose varied by 1-2%. Because of this fact, the high energy regime depth-doses were accepted for clinical use with no further modification.

Nominal SOBP Width	Average SOBP Width (cm) at Range=27.0cm	Average SOBP Width (cm) at Range=20.0cm	Difference (cm)
2.2	2.13	2.15	0.02
2.8	2.79	2.81	0.02
3.5	3.46	3.45	0.01
4.1	4.13	4.14	0.01
4.8	4.79	4.77	0.02
5.5	5.51	5.43	0.09
6.0	6.07	6.01	0.06
6.7	6.70	6.68	0.02
7.5	7.39	7.35	0.04
8.0	8.16	8.07	0.08
9.0	9.10	8.95	0.15
10.0	9.91	9.54	0.37
10.5	10.46	10.25	0.22
11.5	11.47	11.21	0.26
12.5	12.48	12.11	0.37
13.5	13.44	12.73	0.72
14.5	14.89	13.68	1.21

Figure 47. Table of SOBP width and energy regime extrema.

3.6 Medium & Low Energy Characterization and Validation

The medium and low energy regimes were characterized and validated within the dose delivery system. Both the medium and low energy regimes contain the typical clinical spectrum of all non-pelvic treatments, such as intracranial, lung, abdominal and head and neck. Because the FWHM of the Bragg peak vary considerably within these regimes, careful creation of the layer definition files was created. Furthemore, two critical system architecture innovations were required in order to satisfy the clinical specifications within these energy regimes. First, the cutoff point from medium to low energy was determined in order to preserve clinical specification but minimize the impact of additional layers. Second, a skewness parameter was defined and implemented in order to meet the clinical specification within the energy regime.

3.6.1 Energy Cut-off Study

The FWHM of the Bragg peak varies from 2.2cm at 20.0cm range in water to 0.6cm at 6.0cm range in water. This change in FWHM spans two energy regimes. The change is significant enough such that at some “cut off” the Bragg peak has become to sharp to use the standard 0.6cm layer spacing. The binary range modulator allows for 0.6cm or 0.3cm layer spacing. The more coarse 0.6cm spacing is prefered because the treatment time is improved, due to few number of slices. Changing the layer spacing from 0.6cm to 0.3cm effectively doubles the number of layers for a given modulation width. Determining the appropriate cut-off energy is worthwhile in balancing the minimum treatment time with appropriate dose uniformity specification. The increased ripple or peak-to-valley on the SOBP, most pronounced at the distal end, is a direct result of the decreasing FWHM as a function of decreasing energy. For this study, the skew or slant of the SOBP is not evaluated. This will be discussed in the following subchapter.

The Dose Delivery System was designed with a cutoff range in water of 10.0cm. That range in water represented the switch from medium to low energy and from 0.6cm to 0.3cm layer spacing. In order to optimize the cut-off energy, the MLIC was used to systematic change the range in water and evaluate the depth-dose profile and its uniformity. In Figure 48 and Figure 49, the depth doses at 10.5cm and 11.0cm range in water show significant rippled. The peak-to-valley at the distal end is approximately 10% for 10.5cm range in water and 7% for 11.0cm range in water. These results are not clinical suitable. Therefore, the DDS cut-off energy was changed.

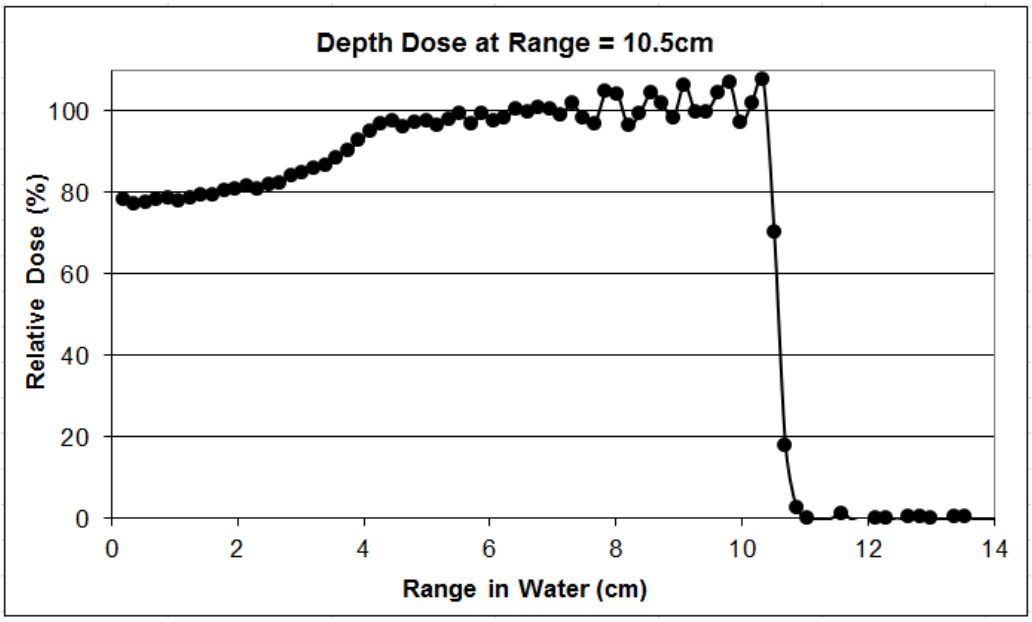

Figure 48. Depth dose at 10.5cm range in water.

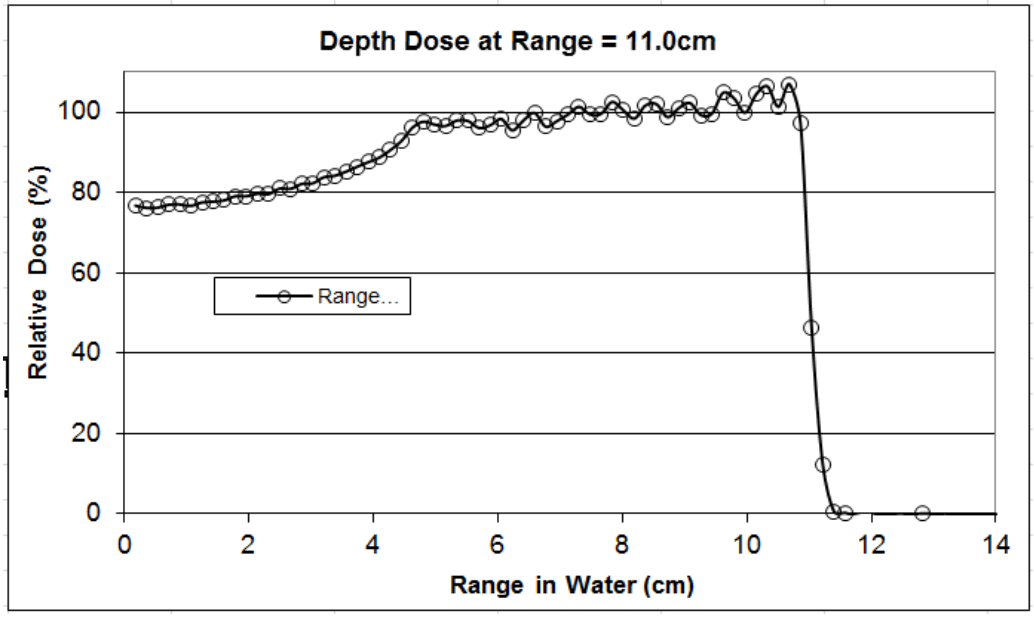

Figure 49. Depth dose at 11.0cm range in water.

Based on further experimentation, in Figure 50, 12.0cm range in water provided a clinically suitable uniformity along the SOBP. No significant peak-to-valley ripples were identified, and the field uniformity is comparable to commissioned SOBPs in the treatment planning system. Furthermore, in Figure 51, when compared to a measurement at 13.0cm range in water, no descernable difference exists in the field uniformity. Therefore, from a uniformity perspective, 12.0cm and 13.0cm range in water are clinically equivalent. Therefore, for the sake of efficiency, using the lowest possible cut-off energy while still preserving clinical specifications is preferred. The new cutoff energy for the Dose Delivery System was set to 12.0cm range in water.

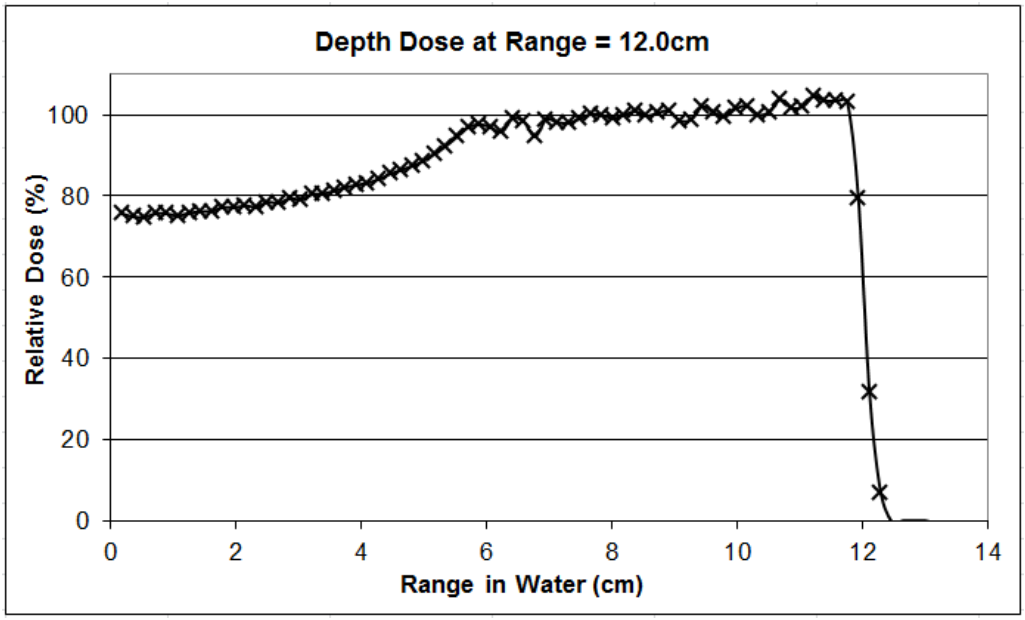

Figure 50. Depth dose at 12.0cm range in water.

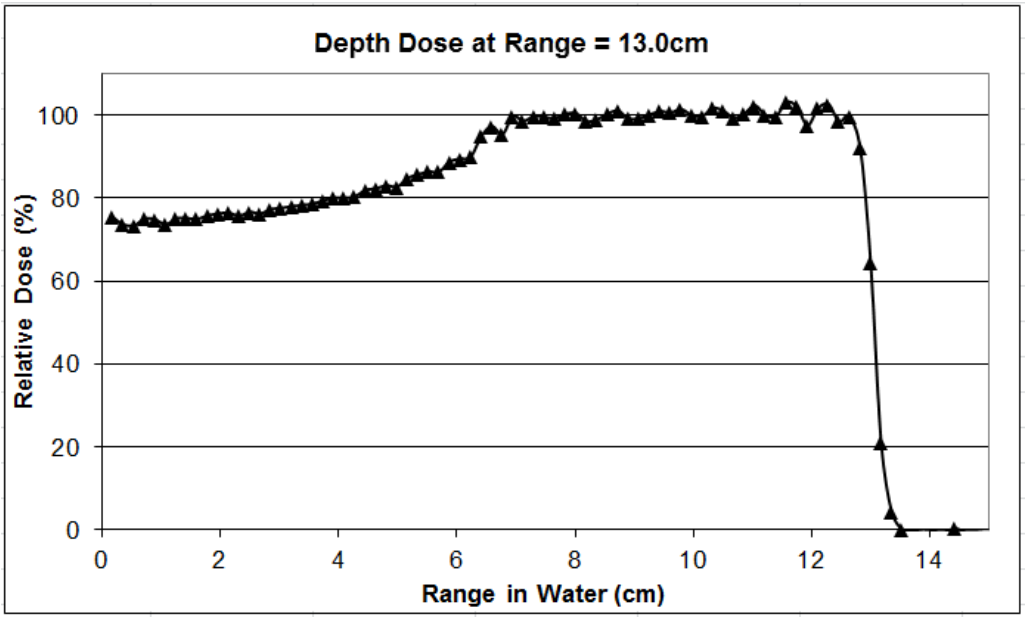

Figure 51. Depth dose at 13.0cm range in water.

3.6.2 Skewness Parameter

With significant decrease in FWHM as a function of decreasing energy, a single layer definition file may not contain the correct number of layers and layer weights for specific

modulation width across a large energy regime. Because the layer spacing is fixed within a given energy regime, small adjustments to the skew or slant of the SOBP are managed by adjusting the weighting of given layers. The effect was studied experimentally for the widest energy regime – the medium energy regime.

In Figure 52, the depth dose for a 7.0cm modulation width at 16.0cm range in water is displayed. For the medium energy regime, the definition energy is 16.0cm range in water. At that energy, the layer definition file is produced and optimized. With adjustment for the skewness, the depth uniformity is acceptable and the SOBP slope is 0.0, i.e. the SOBP is flat.

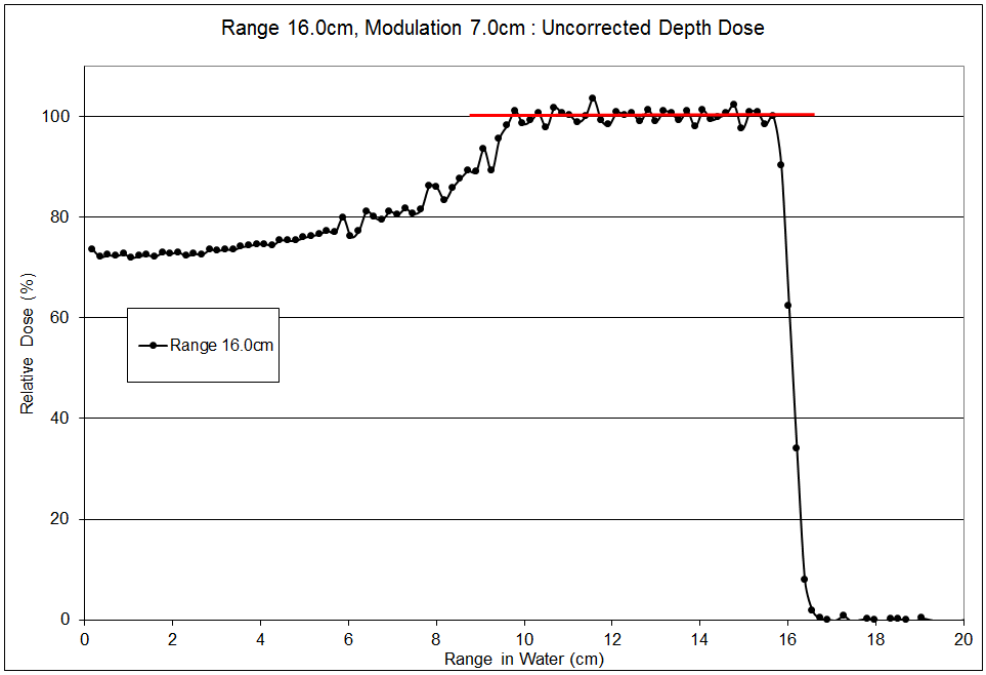

Figure 52. Depth at 16.0cm range in water and 7.0cm modulation width. Depth is not corrected for skewness. 16.0cm range in water is the definition energy for the medium energy regime.

In Figure 53, the depth dose for a 7.0cm modulation width at 12.0cm range in water is displayed. This depth-dose is at the low extreme of the medium energy regime. A clear slope, equal to 1.08, is introduced to the SOBP by reducing the range in water. Without a correction, the layer definition file is delivered as optimized. Without a correction to the SOBP tilt, the clinical specification is not met. In Figure 54, the depth dose for a 7.0cm modulation width at 19.5cm range in water is displayed. This depth dose is at the high extreme of the medium energy regime. A slope, equal to -0.49, is introduced by increasing the range in water. Without a correction to the SOBP tilt, the clinical specification is not met. Based on energy changes from the layer definition file optimization energy, a tilt is predictably introduced to the SOBP. The system required a method for correcting the layer weights to “re-flatten” the SOBP. A “skewness parameter” was introduced to the Dose Delivery System.

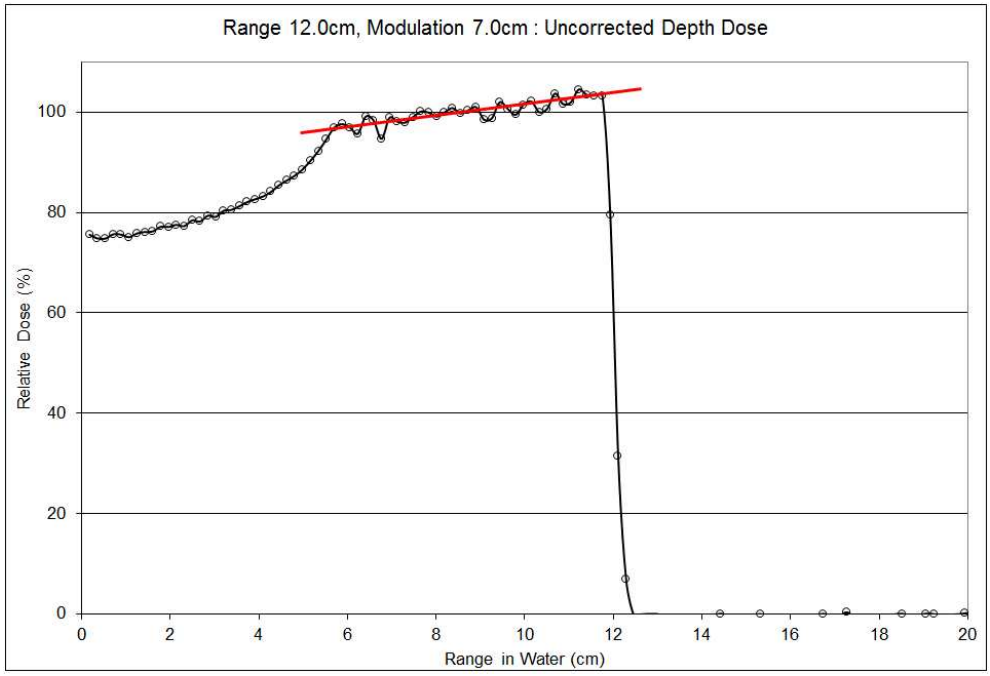

Figure 53. Depth dose for 12.0cm range in water and 7.0cm modulation width. This depth dose is at the low extreme of the energy regime.

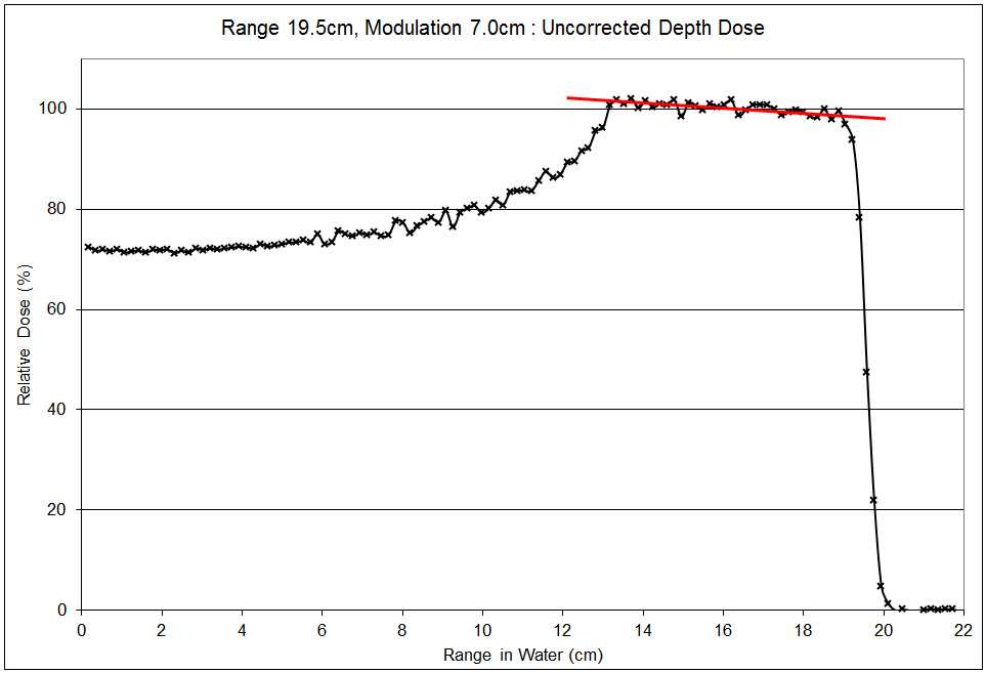

Figure 54. Depth dose for 19.5cm range in water and 7.0cm modulation width. This depth dose is at the high extreme of the energy regime.

The skewness is quantified by the slope of the SOBP. In the above examples, a change in slope from -0.49 to 1.08 is expected within the medium energy regime. The slope is not dependent on SOBP, as each SOBP is created from the truncation and reoptimization of the largest SOBP. In other words, the slope is dependent on the width of the Bragg peak which is depent on range in water, not modulation width.

By using the slope of the SOBP as a metric, a nominal parameter of “skewness” is defined to readjust the layer weights to account for the given slope. Because the skew or tilt of the SOBP is dependent on range, the nominal skewness parameter is alos a function of range in water. For the low and medium energy regime, the nominal skewness parameter was mapped as a function of range in water, see . This data is used to “re-flatten” skewed SOBPs in the Dose Delivery System. This parameter became part of the Dose Delivery System and a required parameter for all treatments with range in water below 20.0cm.

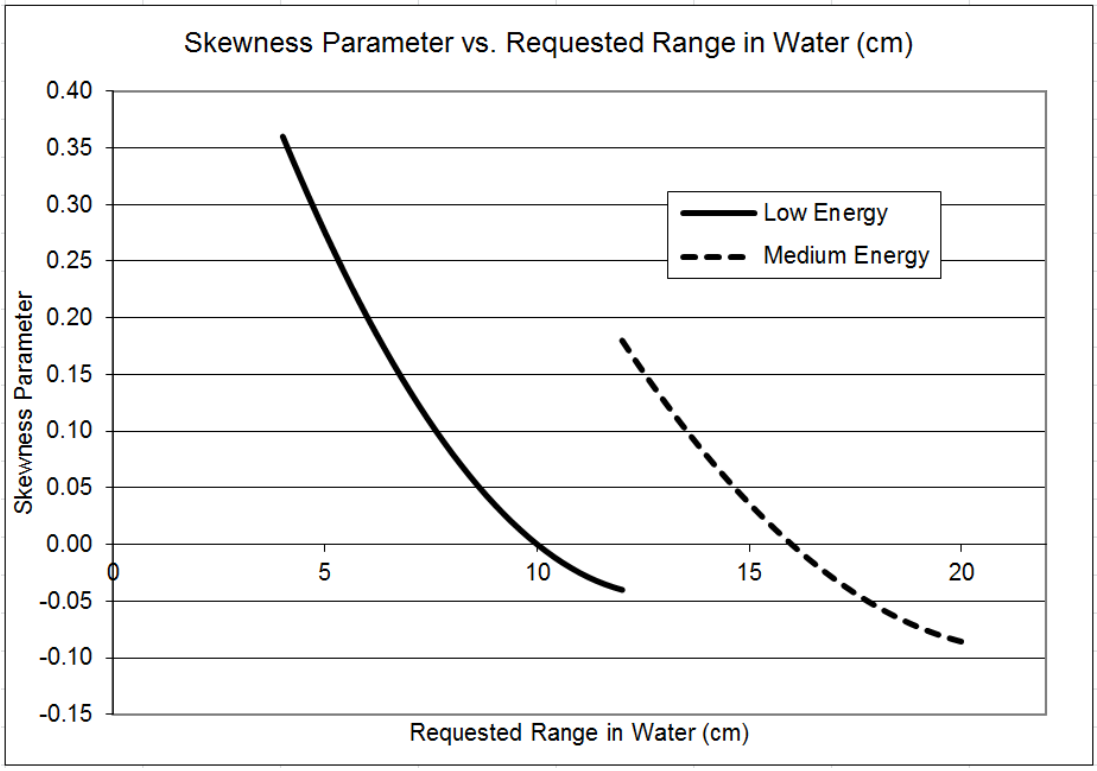

Figure 55. Skewness parameter map as a function of range in water.

After the skewness parameter map was generated, the results were validated for a subset of modulation widths and ranges in water. In Figure 56, the comparison of both an uncorrected and corrected depth-dose are presented. Without the skewness parameter implementation, the depth-dose tilt is not acceptable or within the clinical specification. After using the skewness parameter map and remeasuring the depth-dose, the SOBP is within clincal specification.

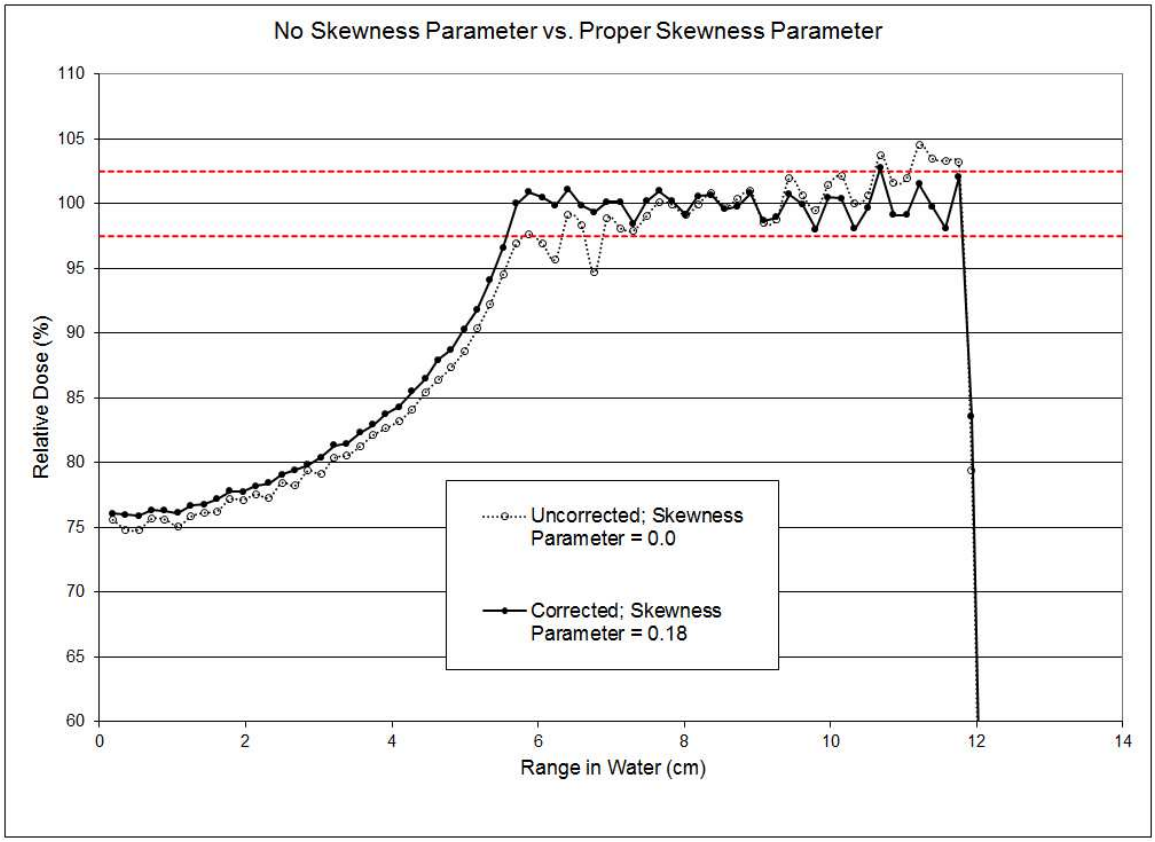

Figure 56. Depth dose for modulation width of 7.0cm and range in water of 12.0cm with and without the skewness parameter correction. Dashed red lines are +/-2.5%.

3.6.3 Medium Energy Characterization and Validation

The medium energy regime contains all depth doses from range 12.0cm to 20.0cm. This regime represents both a large variation energy and a corresponding large variation in Bragg peak FWHM. Based on the previous methodology, see Figure 57, the SOBPs for the medium energy regime were created from a master, large extent SOBP.The minimum nominal modualtion width is 2.2cm and the maximum nominal modulation width is 15.5cm. The number of layers spans 4 to 21 layers.

	Number of Layers	SOBP Width (cm)
Medium Energy Regime: 12.0cm - 20.0cm	4	2.2
	5	2.8
	6	3.5
	7	4.1
	8	4.8
	9	5.5
	10	6.1
	11	6.8
	12	7.5
	13	8.2
	14	9.0
	15	10.0
	16	10.5
	17	11.5
	18	12.5
	19	13.5
	20	14.5
	21	15.5

Figure 57. Medium energy regime number of layers and nominal SOBP widths.

The master layer definition file was created and optimized for modulation width and uniformity at 16.0cm range in water. The final LDF was validated by measurement with the MLIC, see Figure 58. All subsequent LDF were created in the dose delivery system. The MLIC was used to validated the modulation extent and field uniformity for each LDF. Once validated, the LDF was accepted and commissioned in the dose delivery system. A subset of depth-doses are shown in Figure 59.

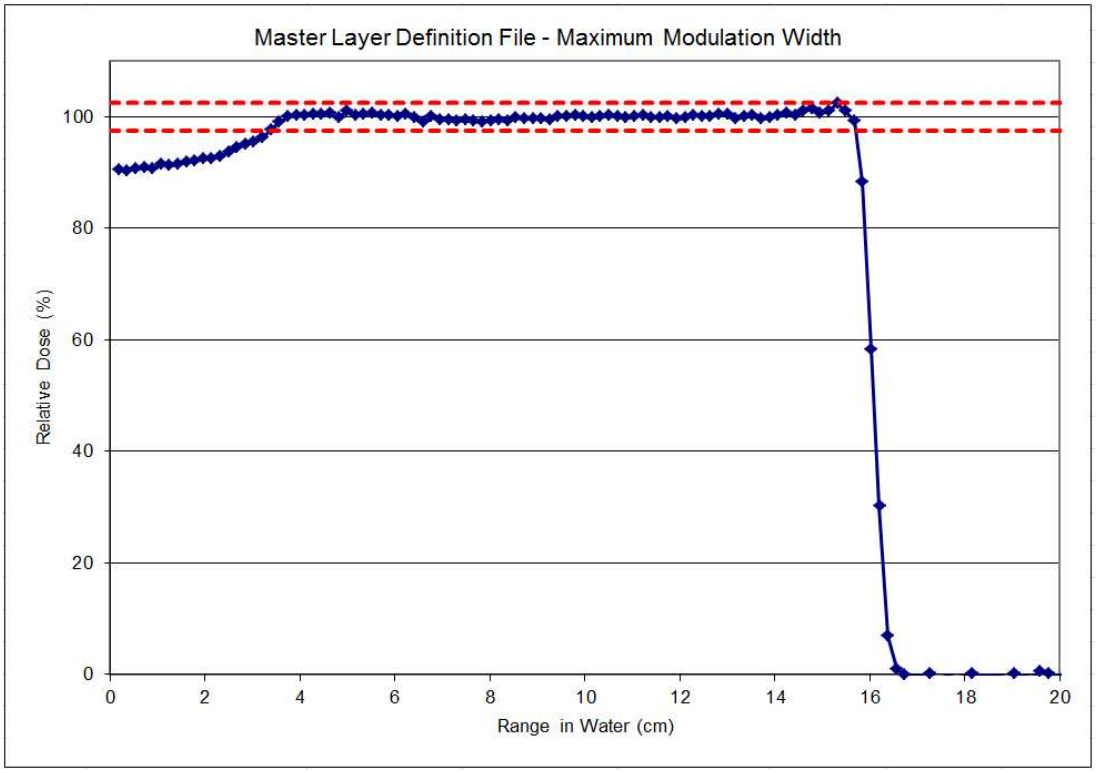

Figure 58. Master layer definition file for medium energy regime corresponding to a nominal 15.5cm modulation width. Dashed red lines are +/-2.5%.

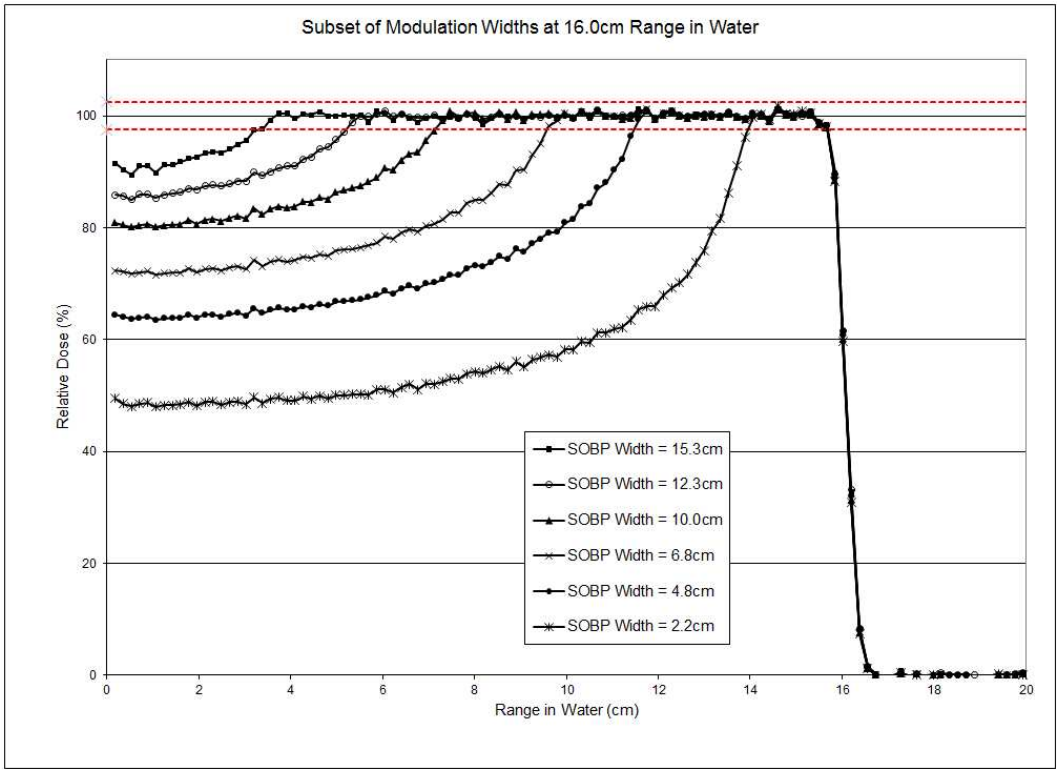

Figure 59. Subset of depth-doses for the medium energy. Dashed red lines are +/-2.5%.

Each layer definition file was tested for reproducibility. Five independent validation meaurement were preformed. The results are shown in Figure 60. SOBP widths are within 0.1cm for all SOBPs, except the largest modulations widths of 13.5cm, 14.5cm and 15.5cm. For the larger modulations, the measured width differs from the nominal by up to 0.4cm. This is explained in the previous chapter. Due to the shallow dose gradient at the proximal end of large modulation widths, small changes in dose results in a large changes of modulation width. The flatness and uniformity specifications are met for all SOBPs.

Nominal SOBP Width	Average SOBP Width (cm)	Standard Deviation (cm)	Percent Standard Deviation	Flatness (%)
2.2	2.15	0.01	0.54	2.81
2.8	2.81	0.00	0.00	1.89
3.5	3.48	0.00	0.00	1.41
4.1	4.20	0.05	1.24	1.67
4.8	4.80	0.04	0.73	2.68
5.5	5.54	0.02	0.36	2.09
6.1	6.21	0.02	0.34	1.38
6.8	6.90	0.05	0.72	1.78
7.5	7.57	0.05	0.65	2.72
8.2	8.15	0.05	0.61	2.9
9.0	8.96	0.06	0.61	1.38
10.0	9.82	0.07	0.72	2.61
10.5	10.46	0.07	0.62	2.89
11.5	11.35	0.01	0.12	1.5
12.5	12.26	0.05	0.42	1.79
13.5	13.09	0.01	0.11	1.53
14.5	14.26	0.04	0.31	1.53
15.5	15.19	0.07	0.47	1.65

Figure 60. Reproducibility measurements for medium energy regime.

Because the layer definition file is optimized at a single range in water, the LDFs required further validation at differing ranges in water. The average of three measurements of the SOBP widths was computed for the extremes of the medium energy regime and the definition point, see . The differences are within 0.25cm for all modulation widths.

Nominal SOBP Width	Average SOBP Width (cm) at Range=16.0cm	Average SOBP Width (cm) at Range=12.0cm	Average SOBP Width (cm) at Range=19.5cm	Difference (cm)
2.2	2.15	2.19	2.13	0.04
2.8	2.81	2.84	2.78	0.03
3.5	3.48	3.49	3.41	0.07
4.1	4.20	4.17	4.09	0.11
4.8	4.80	4.84	4.78	0.04
5.5	5.54	5.56	5.46	0.08
6.1	6.21	6.21	6.11	0.10
6.8	6.90	6.92	6.74	0.16
7.5	7.57	7.58	7.44	0.13
8.2	8.15	8.31	8.19	0.16
9.0	8.96	9.09	9.00	0.13
10.0	9.82	9.84	9.76	0.06
10.5	10.46	10.71	10.50	0.25
11.5	11.35	11.35	11.33	0.02
12.5	12.26	----	12.30	0.04
13.5	13.09	----	13.20	0.11
14.5	14.26	----	14.03	0.23
15.5	15.19	----	15.05	0.14

Figure 61. Reproducibility of SOBP width at extremes of medium energy regime.

3.6.4 Low Energy Characterization and Validation

The low energy regime contains all depth doses from range 6.0cm to 12.0cm. This regime represents a small variation in energy but a large decrease in Bragg peak FWHM. Furthermore, based on the cutoff study, the Bragg peak width decreases such that a finer layer spacing of 0.3cm is required. For the low energy SOBPs, see Figure 62, the number of layers are roughly doubled as compared to the same SOBP in a higher energy regime. The minimum nominal modulation width is 2.3cm and the maximum nominal modulation width is 10.1cm. The number of layers spans 8 to 30 layers.

	Number of Layers	SOBP Width (cm)
Low Energy Regime: 6.0cm - 12.0cm	8	2.3
	10	3.0
	12	3.6
	14	4.3
	16	5.0
	18	5.7
	20	6.4
	22	7.1
	24	7.8
	26	8.5
	28	9.2
	30	10.1

Figure 62. Low energy regime SOBP widths and number of layers.

Based on the previous methodology, the SOBPs for the low energy regime were created from a master, large extent SOBP, see Figure 63. Though the finer layer spacing is implemented to improve uniformity, the finer layer spacing is not used to increase the number of SOBP widths available. The current spacing of SOBP width is approximately 5-10mm. This is adequate for clinical practice. Because of this, in between each SOBP width, is a truncation of two layers, which is the equivalent of one layer in the higher energy regimes.

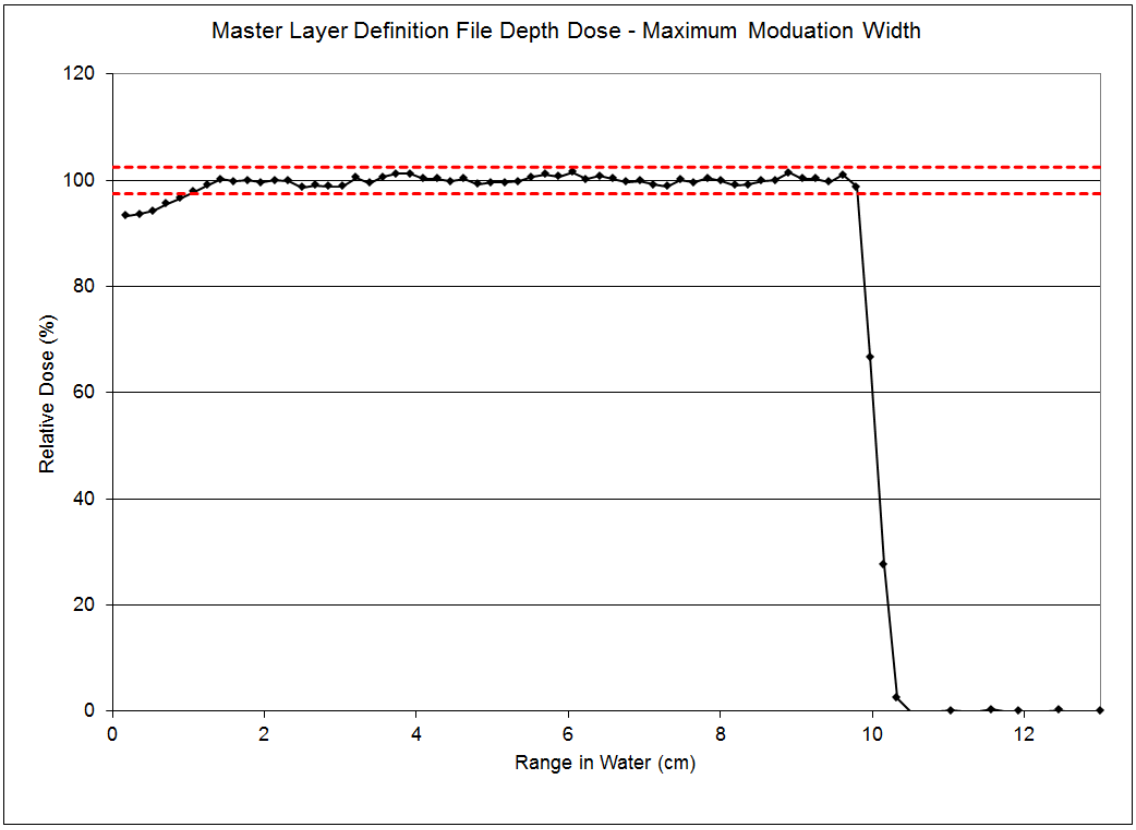

Figure 63. Master layer definition file for low energy regime equivalent to 10.1cm modulation width. Dashed red lines are +/-2.5%.

The master layer definition file was created and optimized for modulation width and uniformity at 10.0 cm range in water. The final LDF was validated by MLIC measurement, see Figure 63. All subsequent LDFs were created in the dose delivery system. The MLIC was used to validated the modulation extent and field uniformity for each LDF. Once validated, the LDF was accepted and commissioned in the dose delivery system. A subset of depth-doses are shown in Figure 64.

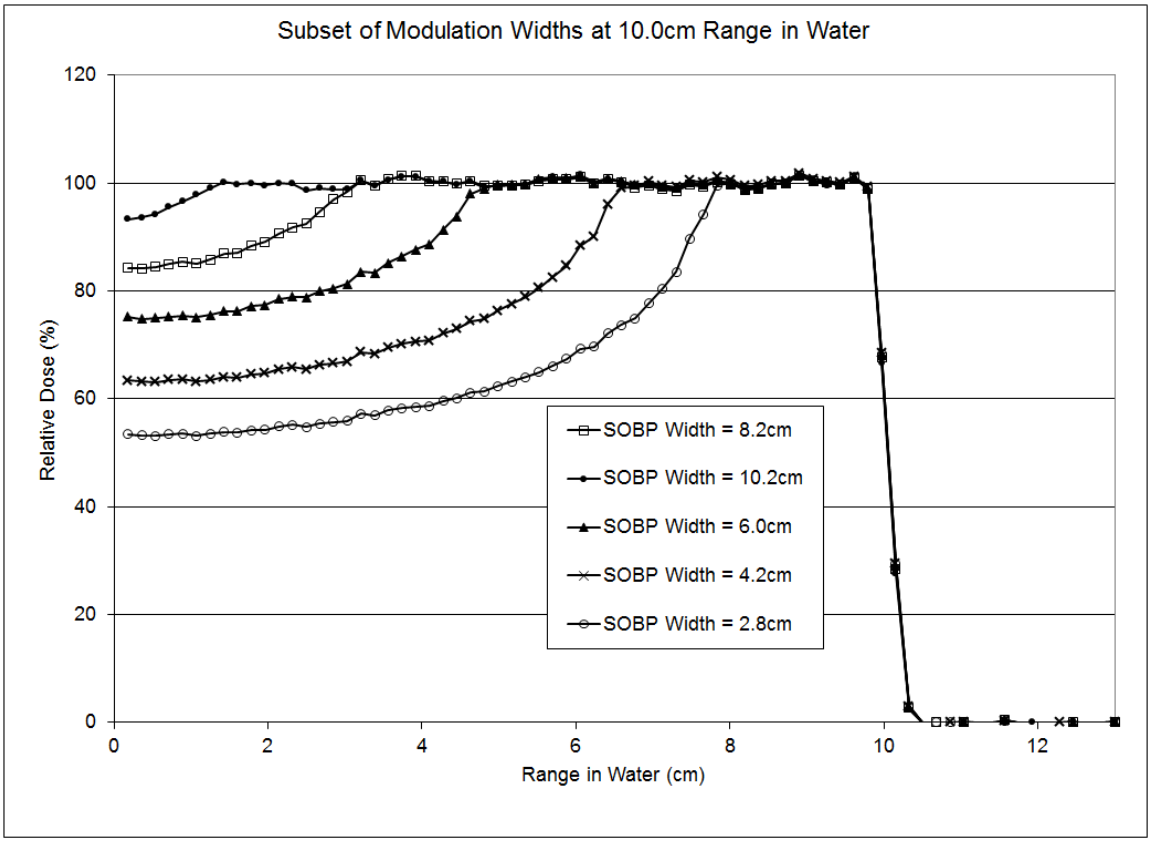

Figure 64. Subset of depth-doses for the low energy regime.

Each layer definition file was tested for reproducibility. Five independent validation meaurement were performed. The results are shown in Figure 65. SOBP widths were within 0.04 cm for all SOBPs, except the largest modulations widths of 9.2 cm and 10.1 cm. For the larger modulations, similar to the other energy regimes, the measured width differed from the nominal by up to 0.5 cm. The reason for this was explained in the previous chapter. Due to the shallow dose gradient at the proximal end of large modulation widths, small changes in dose resulted in a large changes of modulation width. All SOBPs met the flatness and uniformity specifications.

Nominal SOBP Width	Average SOBP Width (cm)	Standard Deviation (cm)	Percent Standard Deviation	Flatness (%)
2.3	2.33	0.03	1.31	2.32
3.0	2.97	0.00	0.00	2.02
3.6	3.62	0.03	0.78	2.64
4.3	4.33	0.02	0.35	2.8
5.0	4.97	0.01	0.12	2.53
5.7	5.67	0.02	0.41	2.18
6.4	6.39	0.01	0.09	2.75
7.1	7.07	0.04	0.50	2.3
7.8	7.75	0.01	0.18	2.08
8.5	8.51	0.03	0.30	2.19
9.2	9.64	0.48	4.98	1.95
10.1	10.72	0.55	5.15	1.82

Figure 65. Reproducibility study for nominal SOBPs width in low energy regime.

Because the layer definition file was optimized at a single range in water, the LDFs required further validation at differing ranges in water. The average of three measurements of the SOBP widths was computed for the extremes of the low energy regime and the definition point, see Figure 66. The differences were within 0.25 cm for all modulation widths, except 5.7 cm, 9.2 cm and 10.1 cm. The average modulation width of the nominal 5.7 cm width was distorted by the measurement at 6.0 cm range in water. By reducing the energy and using the maximum modulation at the energy, the proximal gradient was shallow and exhibited similar properties as the 9.2 cm and 10.1 cm modulation widths. In these cases, as in previous cases, as the proximal gradient

became shallower, a small change in dose equated to a large change is measured modulation extent.

Nominal SOBP Width	Average SOBP Width (cm) at Range=10.0cm	Average SOBP Width (cm) at Range=6.0cm	Average SOBP Width (cm) at Range=11.9cm	Difference (cm)
2.3	2.33	2.31	2.10	0.23
3.0	2.97	2.96	2.96	0.01
3.6	3.62	3.75	3.66	0.13
4.3	4.33	4.45	4.35	0.12
5.0	4.97	5.11	4.94	0.14
5.7	5.67	6.25	5.73	0.58
6.4	6.39	----	6.37	0.02
7.1	7.07	----	7.11	0.04
7.8	7.75	----	7.60	0.15
8.5	8.51	----	8.43	0.08
9.2	9.64	----	9.17	0.47
10.1	10.72	----	10.10	0.62

Figure 66. Reproducibility and variation of SOBP widths at low energy regime extrema.

4 Wobbling Magnet Optimization and Characterization

4.1 Introduction

The uniform scanning system had two primary beam spreading components. In the previous chapter, the binary range modulator was discussed and characterized in depth. The binary range modulator spread the beam through layer stacking along the beam axis creating a spread out Bragg peak. The wobbling magnet scanned the near monoenergetic proton beam in the plane perpendicular to the beam axis. Through the commissioning of both devices, the ultimate dose distribution at isocenter was controlled in three dimensions – X-axis by the binary range modulator and Y-axis and Z-axis by the wobbling magnet. This chapter addresses optimization and characterization of the wobbling magnet.

The unforming scanning system wobbling magnet was a compact X-Y scanning magnet designed at the Indiana University Cyclotron Facility, see Figure 67. Unlike other commercially available proton beam scanning systems, the compact X-Y magnet design allowed the beam to be modeled using a single source-to-axis distance (SAD). All other commercially available proton scanning systems utilized a dual magnet design. In that case, each magnet was located at different SAD, which resulted in differences in the distance behavior of the X-axis and Y-axis penumbrae. Furthermore, when utilizing a single magnet nozzle, the composite SAD could be increased, therefore decreasing the geometric component of the penumbra.

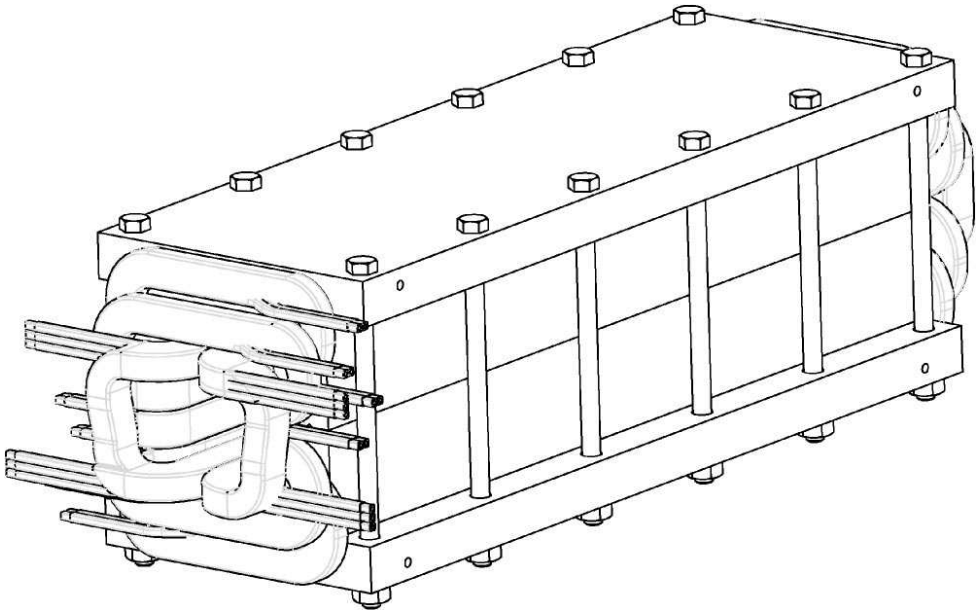

Figure 67. Drawing of compact X-Y scanning magnet.

The wobbling magnet was capable of scanning a 22 x 22 cm^2 field size at isocenter for a 208 MeV proton beam. The operating frequency ranged from 0 – 100 Hz. The bore of the magnet matches the 2" stainless steel beampipe from the energy selection beamline. In order to match the spot position clinical specification of +/- 0.5cm, the accuracy of the magnet and power supply unit were designed with current amplitude and reproducibility specification capable of accurately scanning the proton at <0.002 mradians. The current amplitude ranges to 418.8 Amps which yielded approximately 2000 Gauss magnetic field. The magnetic field uniformity was within 2 – 7% for a 2 cm radius within the magnet bore. Importantly, uniformity was a second order effect on the overall beam spot position precision at isocenter.

4.2 Materials and Methods

The scan pattern is not strictly patient-specific in a uniform scanning environment. The scan pattern depends on two factors – the snout size and the range in water for the particular field. In the case of snout size, the scan pattern was optimized to provide a uniform field for the maximum field size of the particular snout. As the snout increased, the maximum field size would increase and the scan pattern required adjustment. In the case of range in water, the spot size in air depended on the energy. At high energy, defined as greater than 20.0 cm range in water, the spot size in air was narrow. The high energy proton beam traversed only thin thicknesses of the energy selection line degrader. Therefore, the narrow spot exiting the cyclotron was better preserved. For low energy, defined as less than 20.0cm range in water, the spot size in air was large. As the energy decreased, the spot size increased due increased interactions through larger energy selection line degrader thicknesses.

Range in Water (cm)	Snout Diameter (cm)	Maximum Field Size (cm)	Waveform File
6.0cm - 20.0cm	10	10	Snout10Range20.wwf
20.0cm - 27.0cm	10	10	Snout10Range27.wwf

Figure 68. Transverse scanning system file structure, requiring a optimized scan pattern for high (20.0-27.0cm range in water) and low (6.0-20.0cm range in water) energies.

4.3 Scanning Pattern

The wobbling pattern, or scan pattern, had several parameters, such as pattern, amplitude and pattern density. The value of each parameter was determined and

empirically validated, such that the clinical performance criteria, such as flatness and symmetry, were not compromised.

4.3.1 Zig zag, circles and lines

The primary parameter of the wobbling pattern was the pattern. The X-Y scanning magnet was capable of generating a wide variety of patterns. The IUCF developer of the scanning magnet experimented with several patterns[35]. Wobbling magnets in particle therapy have had a unique history. Some of the patterns developed were: lines, zig-zags, concentric circles, and sequential rectangles. For simplicity, both in concept and testing, the clinical requested scanning patterns were restricted to line-based uniform scanning. Ultimately two scan patterns were tested; zig-zags and rasters.

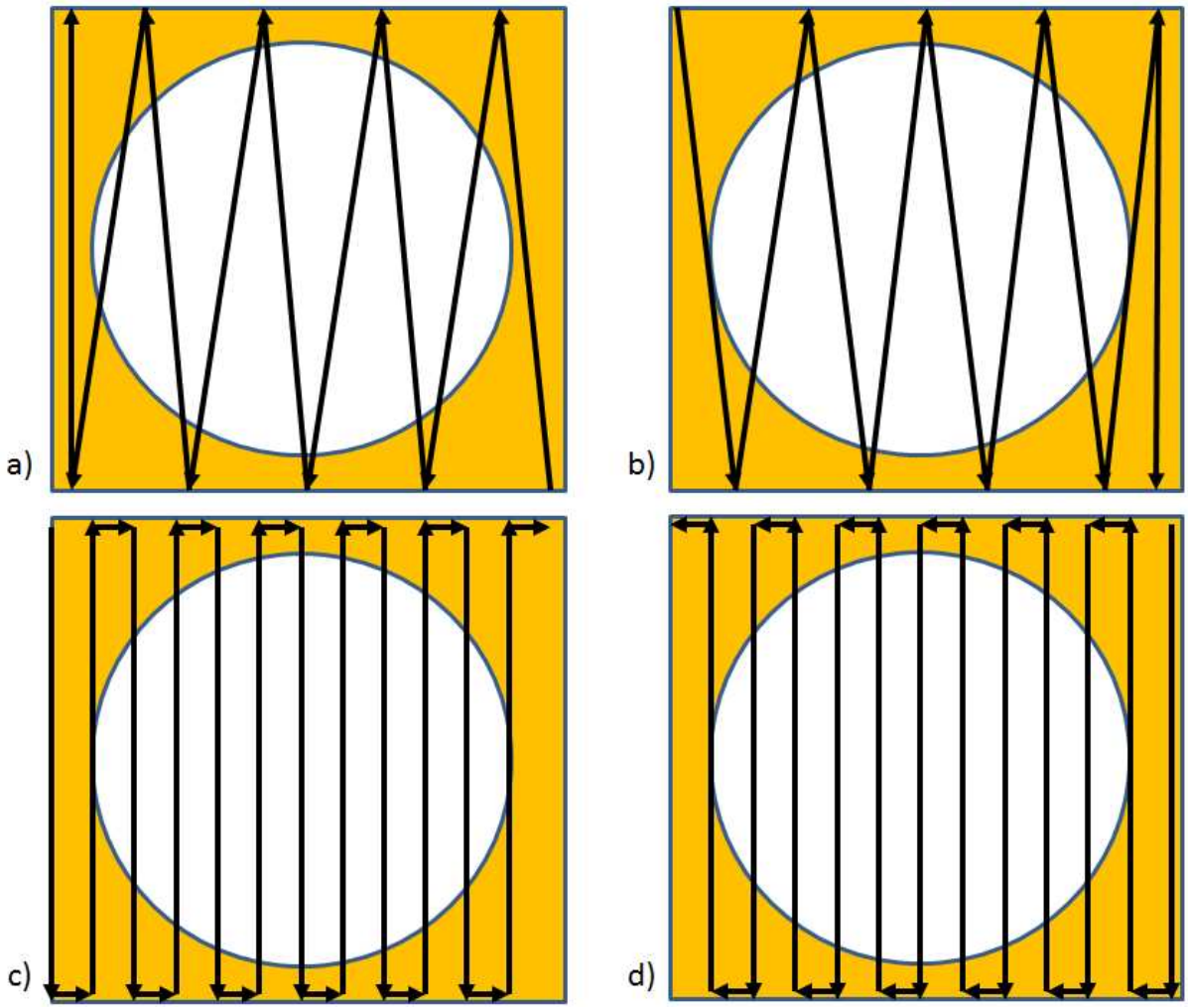

Figure 69. Wobbling magnet scan patterns. a) zig zag moving left, b) zig zag moving right, c) raster scan moving right, d) raster scan moving left. a) and b) form a full zig zag scan. c) and d) form a full raster scan.

The two main scan patterns are shown in Figure 69. In a uniform scanning system, the proton beam moves in a fast scan and slow scan direction. In the figure above, the slow scan direction is right-left; the fast scan is up-down. For a full uniform scan pattern, the beam must pass in the slow scan direction for a roundtrip, for example right-to-left and left-to-right.

Both patterns were examined from a safety and clinical efficiency perspective. Both patterns were capable of creating a clinically acceptable field. However, the raster scanning pattern was preferable for two reasons. First, uniform scanning systems required that the patient specific aperture be overscanned by a certain margin to ensure uniformity. By simple geometric analysis, the zig-zag pattern required a larger overscan margin because of the non-symmetrical pattern design. The raster scan did not have this limitation. Second, and more importantly, the zig-zag pattern required a full round trip to provide a flat field. By examination, any single pass was non-uniform. The raster pattern was uniform both on a single pass and a round trip. Because the scanning system was designed to start and stop randomly within the scanning field, the uniformity produced by a single raster scan pass was preferred.

4.3.2 Amplitude and density

The raster pattern was a straight forward design and had only two physical, configurable parameters, the amplitude and line density. These were configured based on the design of the scan pattern, see Figure 70. The amplitude was defined as the length of the raster scan. Both an X and Y amplitude were designated for the scan pattern. Also, they were configurable on-the-fly through the dose delivery system. However, by modifying the amplitude on the fly, the line density could be indirectly changed. The line density was defined in simple terms as the number of lines per centimeter. For example, if there were 10 lines in a 10 x 10 cm^2 scan, then the line density was 1 line/cm. In the uniform scanning system, the scan pattern was designed with a specific number of lines. By design, those number of lines correspond to a certain X and Y amplitude. If the amplitude was changed through the DDS but the pattern remained the same, the

designed number of lines will be used over a modified amplitude, therefore changing the line density. For uniform scanning, line density was the parameter that determined the overall uniformity in the transverse plane. The amplitude determined the aperture overscan margin.

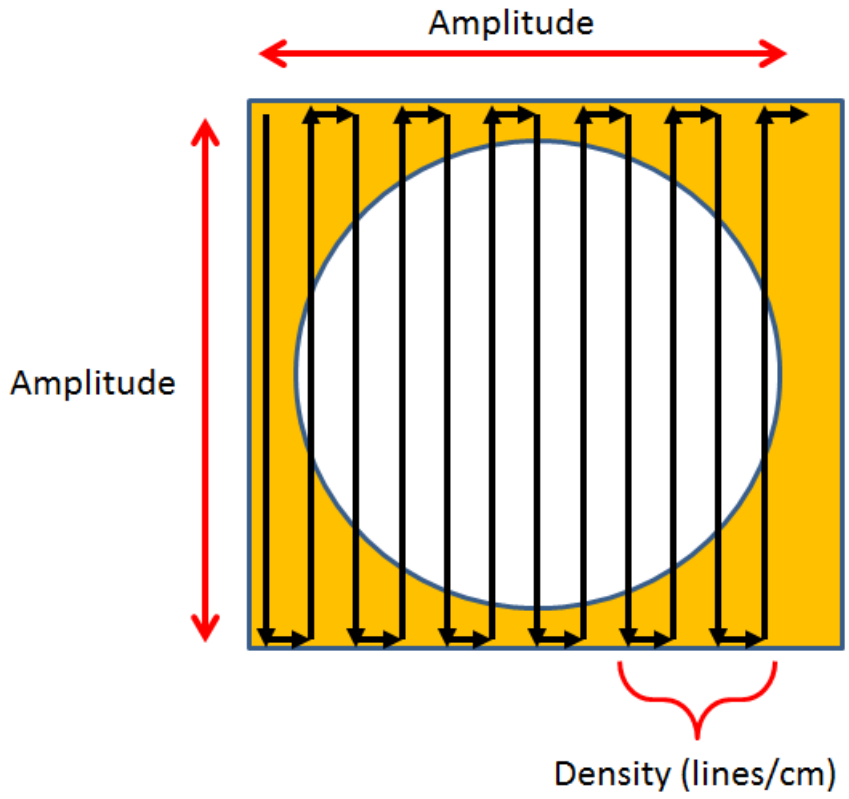

Figure 70. Description of specific parameters of a uniform scanning pattern.

The line spacing was the inverse of line density. In order to create a uniform field, the line spacing was related to the width of the beam spot for that given condition. For our investigation, a matrix of line spacing and sigma was created. The standard deviation of the beam spot is not easily controllable and so was not adjusted. The line spacing was easily configurable based on the scan pattern. Without the availability of a Monte Carlo study, the investigation used measurements to determine the optimal line spacing as a ration of the line spacing to beam spot size. The IUCF developer identified the

appropriate ratio as 1.2-1.6 based on the beam spot size. Through measurement, our results agreed reasonably well. For the high energy and narrowest beam spot, the line spacing was smaller and line density correspondingly higher. For medium and low energy, the beam spot was wider and therefore a larger line spacing and lower line density were required. Regardless, the ratio of line spacing to beam spot size was kept constant. Based on measurement, see Figure 71, the ideal ratio was 1.25.

		Line Spacing		
		0.6	1	1.4
sigma	0.7	0.86	1.43	2.00
	0.8	0.75	1.25	1.75
	0.9	0.67	1.11	1.56
	1	0.60	1.00	1.40
	1.1	0.55	0.91	1.27
	1.2	0.50	0.83	1.17

Figure 71. Values for Line Spacing (cm) / Sigma (cm). Various combination investigated. Solid circle is values used for high energy (20.0cm to 27.0cm range in water). Dashed circle is values used for low and medium energy (6.0cm to 20.0cm).

In order to arrive at this conclusion, an ion chamber profile was measured for a given scan pattern in a given energy regime. For example, in Figure 72 and Figure 73, the inplane and crossplane transverse profiles are displayed for a high energy proton beam. The high energy proton beam spot was narrow. This would necessitate a high line density. For the inplane measurement, there were no significant differences in the dose profile when different line densities were used. This was expected as the inplane measurement was along the direction of the fast scan. However, the crossplane measurement exhibited varying uniformity based on varying line densities. Greater line densities exhibited less ripple than coarser scan patterns (Figure 72). The high line

density profile was rounded near the shoulder was address by adding an overscan margin. The same study was performed for low and medium energy.

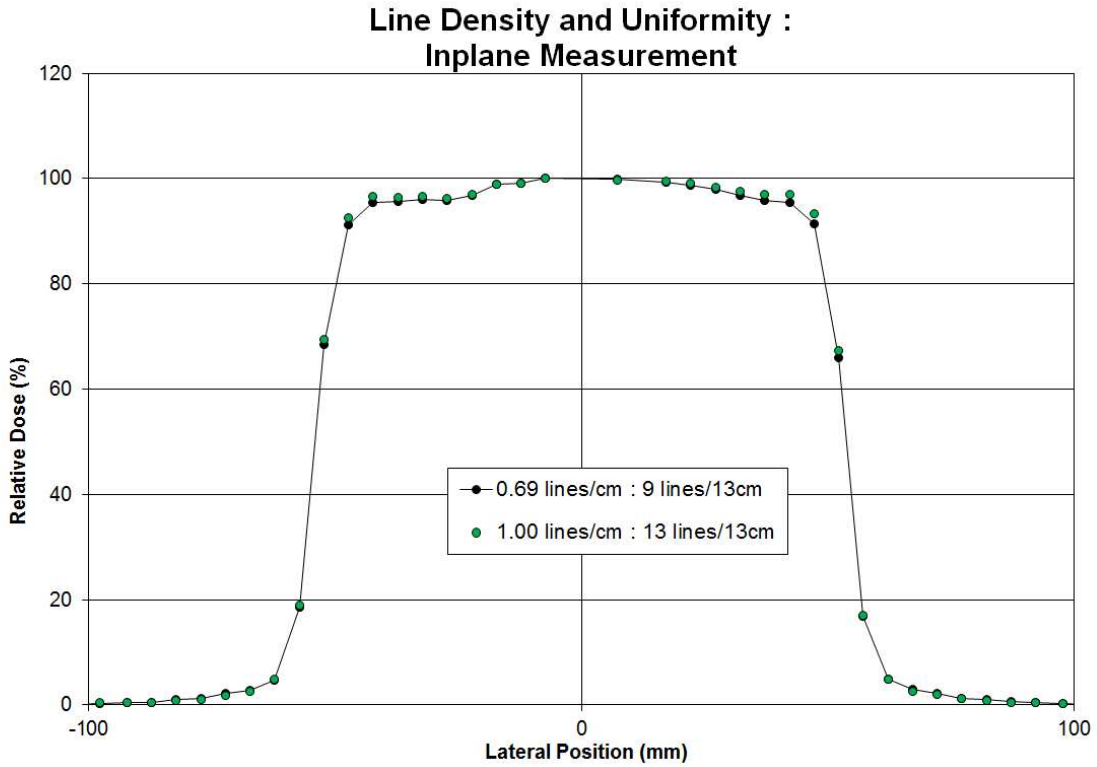

Figure 72. Transverse inplane profile showing uniformity difference between different line densities.

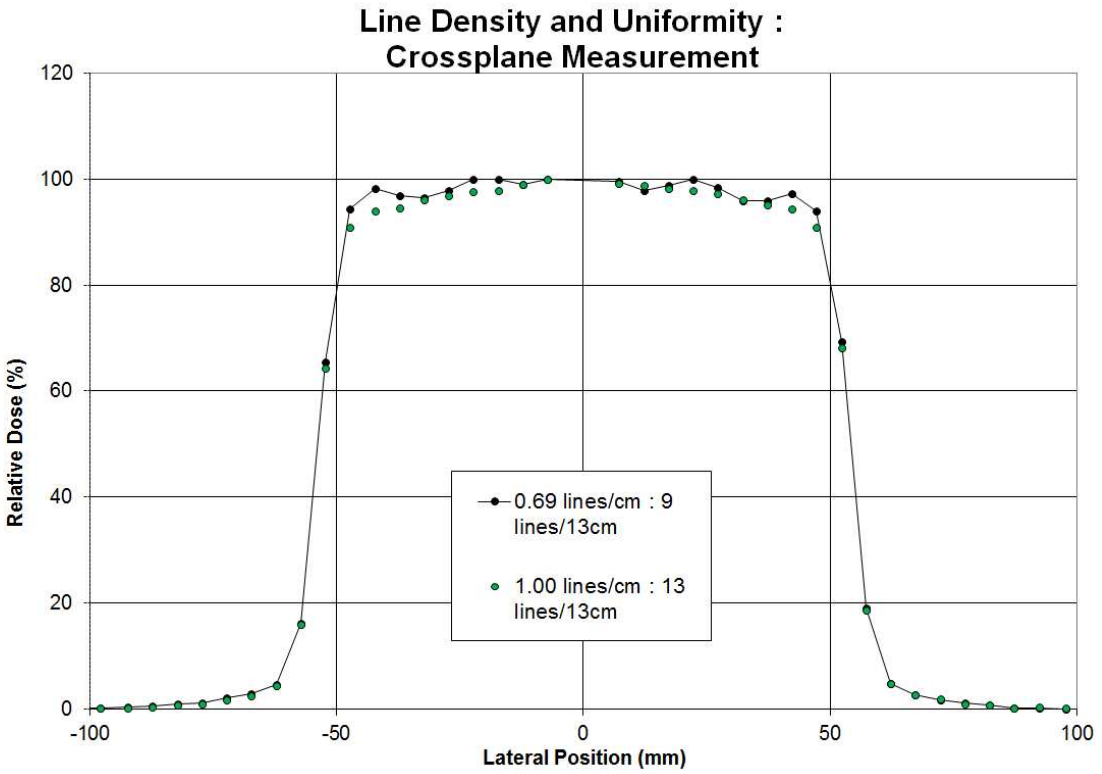

Figure 73. Transverse crossplane profile showing uniformity difference between different line densities

4.3.3 Over-scanning of the Aperture

Patient specific apertures were employed in the uniform scanning system. The aperture was defined to the beam's eye view of the target in the plane perpendicular to the beam. The uniform scanning system overscanned the aperture by a specified margin to ensure uniformity of the field passing through the aperture, with the overscan margin being a function of the beam spot size. If the desired dose at the edge of the aperture was 95%, then the overscan margin would be two standard deviations assuming that the beam profile exhibited a Gaussian shape. For this uniform scanning system, this was approximately 2-3cm.

The effect on the dose distribution of changing the scan margin is apparent in Figure 74 and Figure 75. Examining the inplane transverse profile, as the overscan was increased the dose at the aperture edges increased. Enlarging the overscan margin had the greatest impact at the radiation field perimeter. In the crossplane transverse profile, the same improvement in uniformity was seen when comparing smaller and larger overscan margins. There was a diminishing return on field flatness of expanding the margin more than 2 or 3 standard deviations of the beam spot profile. Increasing the overscan increased neutron and secondary particle production, and decreased dose delivery efficiency.

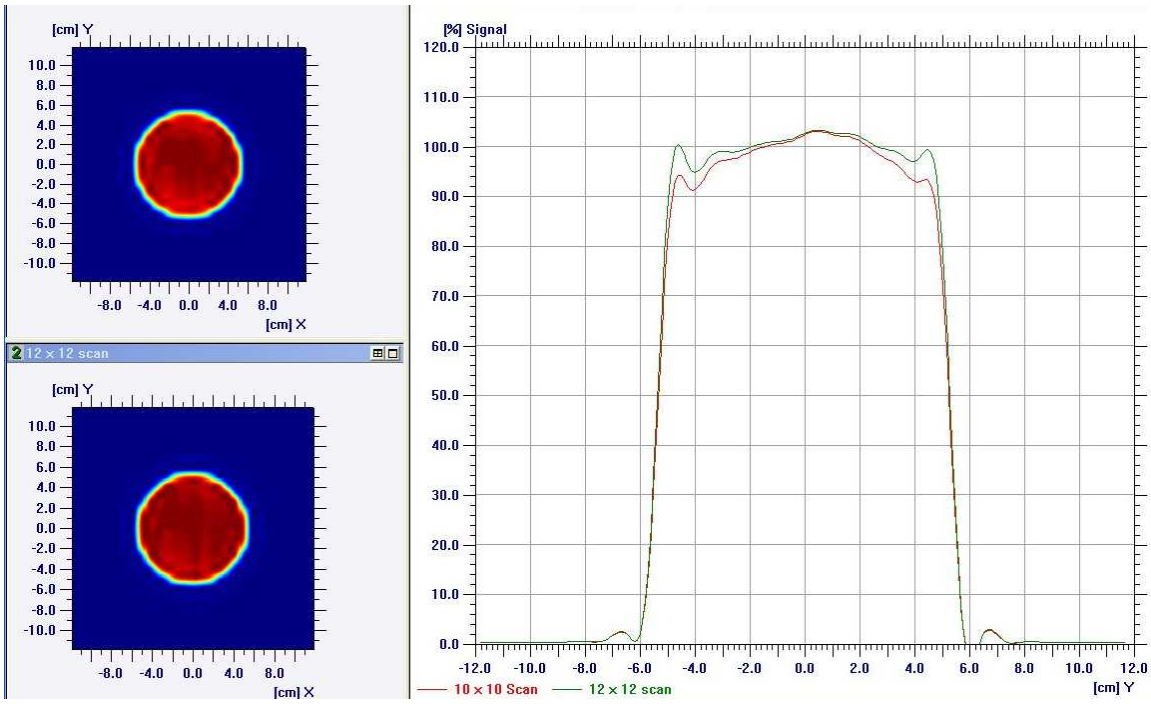

Figure 74. Transverse inplane measurement with varying overscan margin. The red profile is 10 x 10cm^2 scan; the green profile is 12 x 12 cm^2 scan.

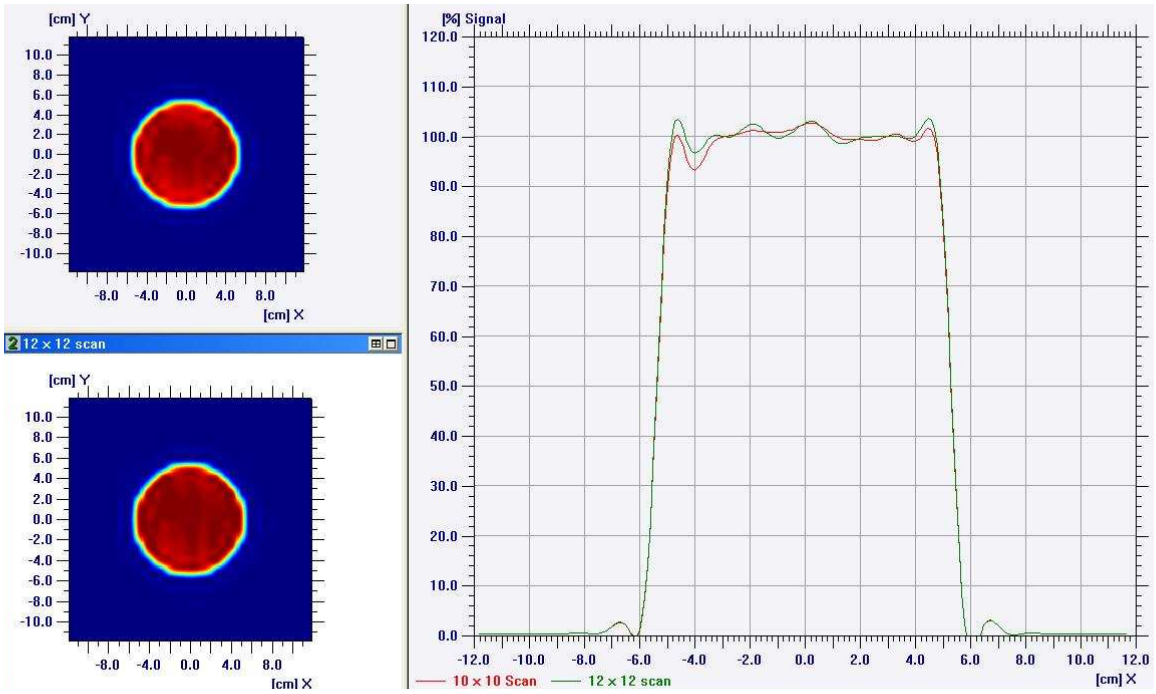

Figure 75. Transverse crossplane measurement with varying overscan margin. The red profile is 10 x 10cm^2 scan; the green profile is 12 x 12 cm^2 scan.

4.3.4 Results and Impact

The line density, scan amplitude and overscan margin were determined based on the results of the above studies. The ratio of line spacing to beam spot size was determined and the scan pattern created. For high energy, the line density was approximately 1.0 line/cm, or 13 lines / 13cm. For low and medium energy, the line density was approximately 0.7 line/cm, or 9 lines / 13cm. The scan amplitude was fixed at 13 x 13 cm^2. Once the amplitude was selected, the appropriate line density was incorporated. This amplitude included a three standard deviation overscan margin from the standard 10 x 10 cm^3 clinical treatment field.

4.4 Waveform File Creation, Optimization and Characterization

The creation of the waveform files that controlled the wobbling magnet was controlled through the architecture of the system. The IUCF developer created a scan pattern and compiled a binary file that the Dose Delivery System could read, interpret and use to instruct the wobbling magnet. The waveform file was dependent on maximum snout size and the energy regime. Three maximum snout sizes were available – 10 cm, 20 cm and 30 cm. For the purposes of transverse profiles, the low and medium energy regimes were combined because they showed no significant difference in transverse spot size. The high energy regime required its own waveform file due to the narrow beam spot.

4.4.1 Creation and Optimization

The transverse profiles next required validation. The initial measurements for a waveform files of a given energy and modulation were the transverse profiles or planes throughout the dose reference volume. Three planes through a single dose delivery are shown in Figure 76. The uniformity of the profile that entered the phantom or patient was generally not flat in a uniform scanning system. The system was designed and scan pattern optimized to deliver a flat field at isocenter in the center of the modulated field. Therefore, a ripple was routinely measured in the entrance dose region. However, as the pattern traversed the medium and underwent multiple coulomb scattering, the uniformity gradually improved due to the widening of the beam spot. The field was flat and symmetric within the clinical specification of 3.0% near the field center. At the field edge, field ripples began to reappear due to the fact that the distal region accumulated does only from the Bragg peak, whereas, the SOBP was composed of a sum of many

Bragg peaks and plateaus. This had the effect of further smoothing the uniformity of the field.

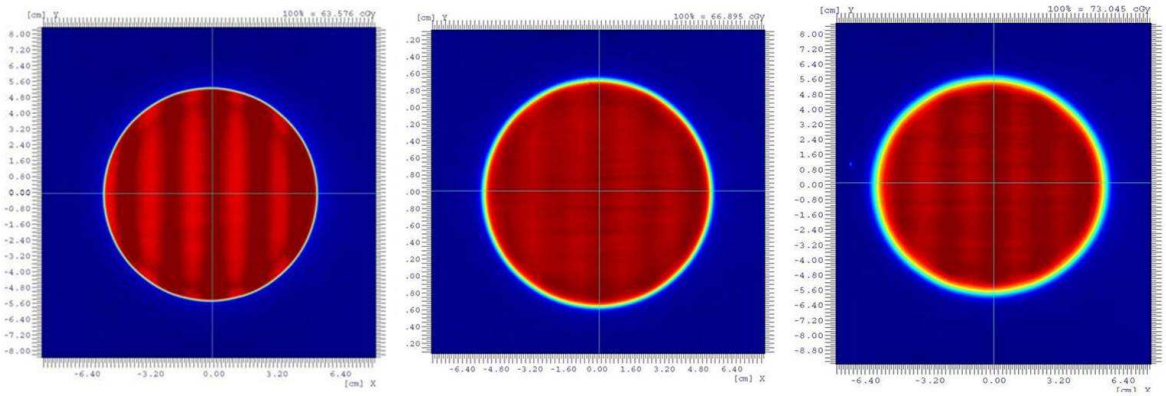

Figure 76. Transverse profiles at the entrance region, center of modulation and distal modulation region.

In Figure 77, the comparison of field uniformity from entrance region and center of modulation is clear. The ripple reduces in magnitude as the field traverse medium. The profiles clearly demonstrated the entrance region was a non-clinically viable treatment region. In proton therapy, this was always the case. The region required to treat the patient's target was defined by the center of modulation. In most cases, the center of modulation, the isocenter of the treatment room, and the geometric center of the patient target coincided. For this reason, uniform scanning systems were designed for flatness and symmetry at the center of modulation.

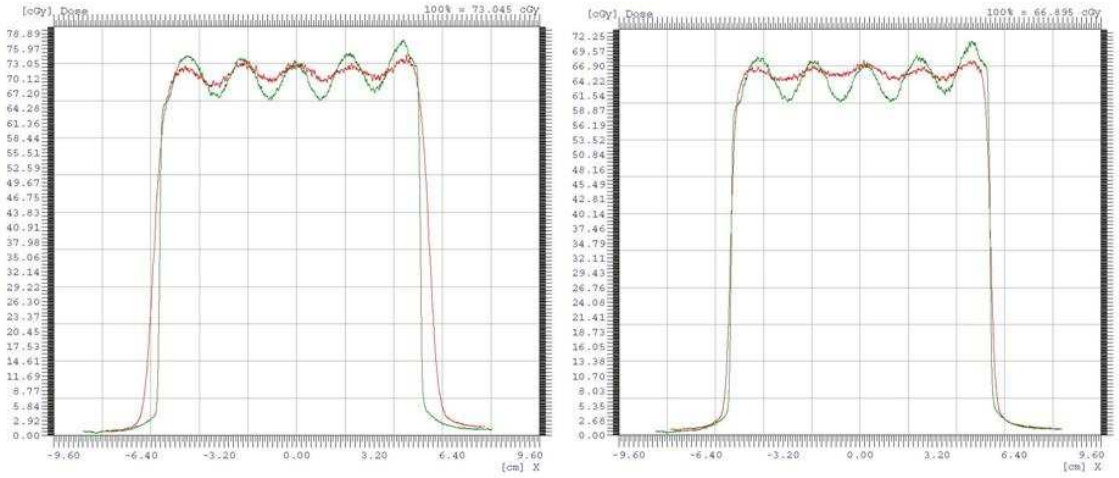

Figure 77. Comparison of entrance uniformity with center of modulation uniformity. Green curve is entrance profile; red line is center of modulation profile.

4.4.2 Characterization

With the waveform files designed, implemented and initial validation performed, the transverse profiles of the uniform scanning system were characterized for clinical use. The summary of the transverse profile measurements are shown in Figure 78 and each metric is an average of at least three independent measurements. The flatness was within 3.2% and the symmetry was within 0.25% for the clinical spectrum of 5.0 cm to 27.0 cm. Predictably, preserving uniformity was a challenge for the narrow beam spot at high energy. However, this system met the clinical specification of 3% flatness and symmetry.

Range (cm)	SOBP (cm)	Cross Plane		In Plane	
		Flatness (%)	Symmetry (%)	Flatness (%)	Symmetry (%)
5	2	1.08	0.2	0.78	0.4
10.5	5	1.22	0.14	0.85	0.24
13	5	1.62	0.11	1.25	0.2
17	10	1.74	0.17	1.08	0.2
19	10	2.1	0.16	1.62	0.19
24.5	10	2.92	0.06	2.57	0.18
27	10	3.18	0.05	3.29	0.24

Figure 78. Summary of transverse profile data. Each metric is the average of three independent measurements.

The penumbrae of the pristine peaks and uniform scanned fields are characterized and shown in Figure 79. As the range in water increased, the radiation field penumbra widths increased. Over the clinical spectrum, the penumbrae widths varied from approximately 1.0 mm to 8.0 mm. It should be noted that the uniform scanning resulted in a smaller penumbra widths as compared to older passive scattering systems. The penumbra had two components – geometric penumbra and scatter penumbra. By eliminating scattering foils, the angular confusion of the proton beam was reduced and the penumbra improved for a given geometric nozzle design.

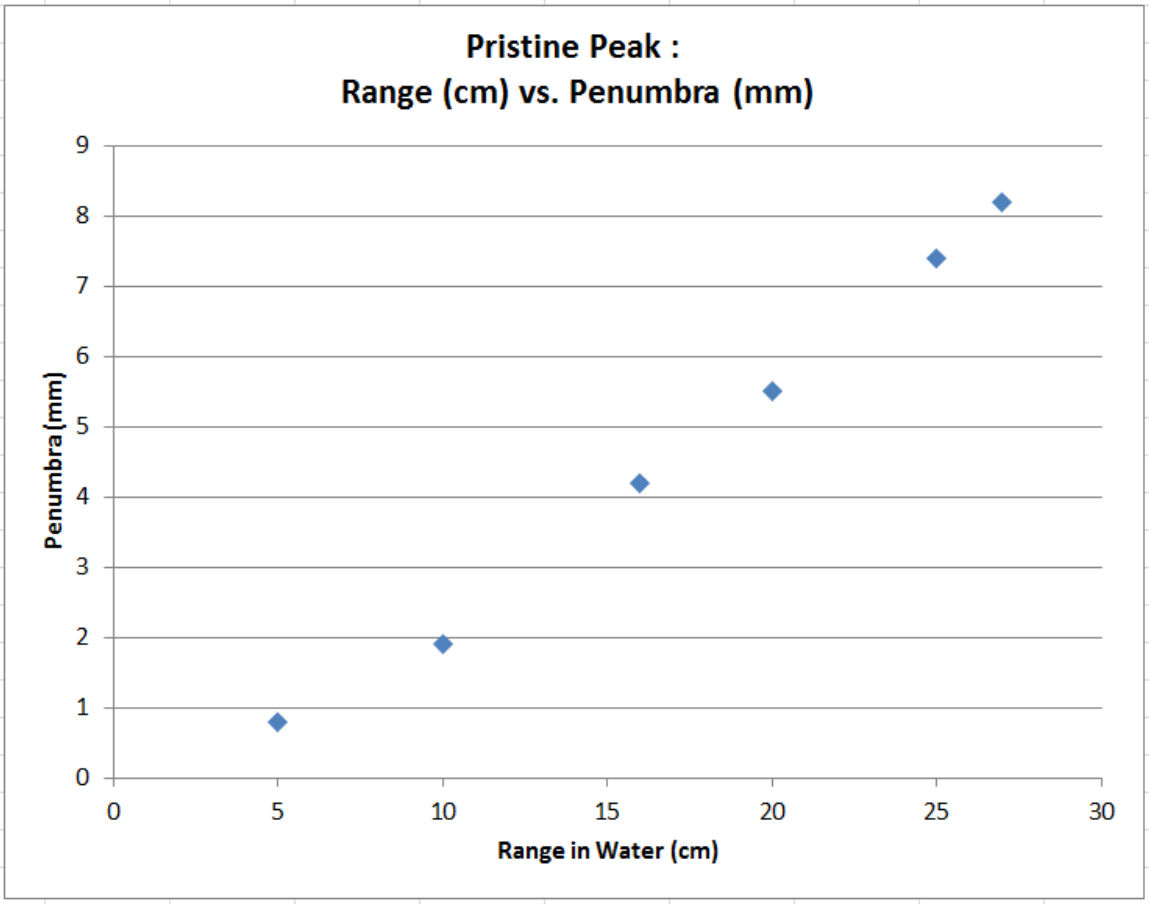

Figure 79. Penumbra as a function of range in water for uniformity scanned pristine Bragg peaks.

The penumbra for a given range at various depths is shown in Figure 80. For all but the shallowest proton energies, the penumbra is dominated by the proton interaction and scatter in water and the geometry of the beam delivery system (e.g. the source-to-axis distance and effective source size). For example, the 16.0 cm depth penumbra was equivalent to the penumbra of a pristine Bragg peak of 16.0 cm range in water. The uniform scanning penumbra width was dominated by the scatter in the medium. The penumbra width was correlated to the amount of water or material preceding the plane so no significant difference should have existed between penumbra widths as a function of depth and range in water.

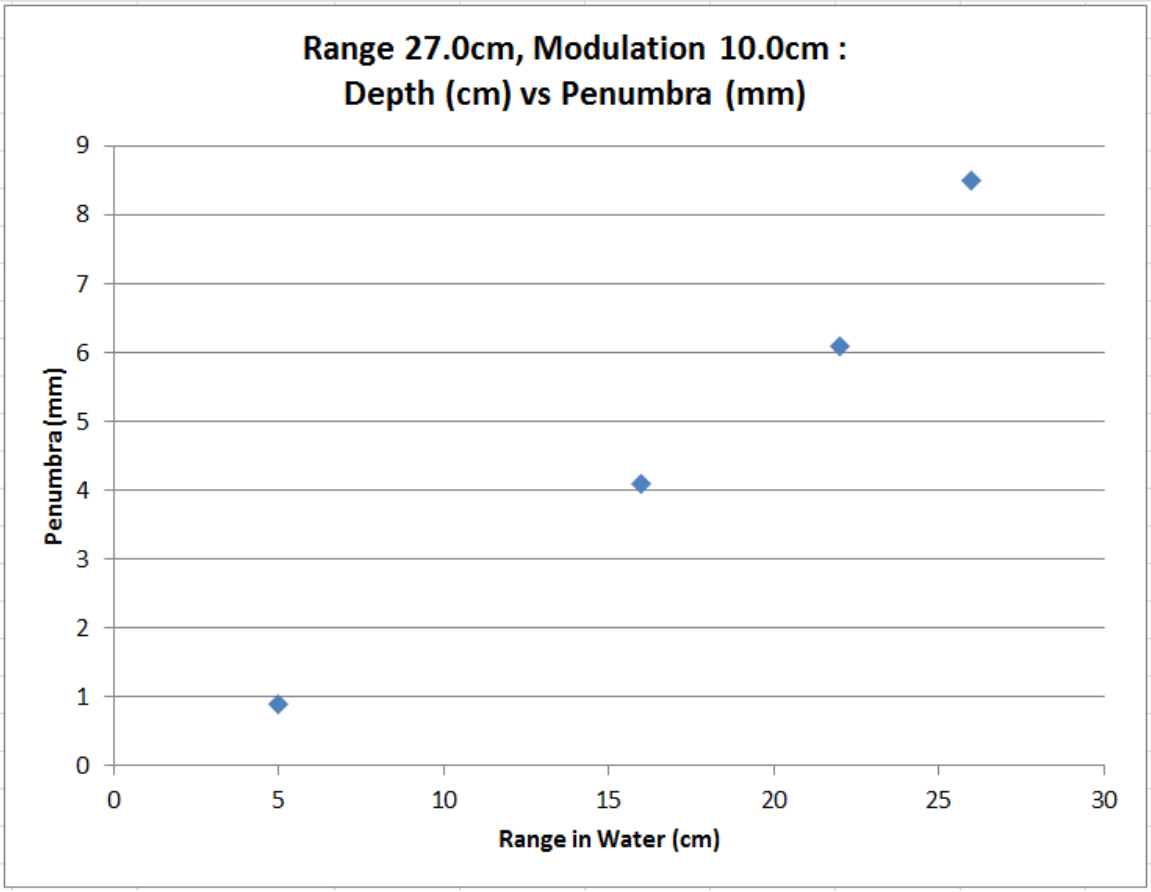

Figure 80. Penumbra at different planes for a full energy proton beam.

5 Conclusion

5.1 Future Work

Several important projects resulted from the clinical implementation of the uniform scanning system.

5.1.1 Detector development

The MLIC at Indiana University was the first user-friendly ion chamber array used for depth-doses in a uniform scanning proton beam. As part of the future work already accomplished, IBA Dosimetry developed a commercial version of the detector. During the physics task force development discussions between Indiana University and IBA Dosimetry, the basic design of the MLIC was preserved. Minor changes to the spatial sampling and overall length of the detector were made. Two significant improvements to the detector designed were implemented. The IBA Dosimetry Zebra, which was the brand name of the commercial MLIC, was integrated into the IBA Dosimetry OmniPro suite of software. Furthermore, the older electronics, electrometer and cabling from the MLIC were eliminated and improved electronics were used. The IBA electronics, identical to the electronics used in the Matrixx detector, provided the processing of the signal at the detector. The signal was then digitized and transmitted through an Ethernet cable to the control computer. This significantly reduced the noise induced by the extensive cabling of the MLIC while increased the number of channels available.

Scanning systems are replacing the scattering systems in both current and future proton therapy installations. Uniform scanning and pencil beam spot scanning are transitioning into the dominant delivery systems. The same nozzle can be used for both uniform and

spot scanning with no additional devices. Though the MLIC is suitable for characterizing a uniform scanning field, detector developments are required for an equivalent pencil beam spot scanning detector.

Uniform scanning fields are typically commissioned with a field size greater than 3 x 3 cm^2. For the development of a detector in this environment, the goal is to design a detector as small as possible that preserves a signal-to-noise greater than 1.0. The smaller detectors have a reduced dose averaging effect, increased resolution and have a less restrictive minimum field size requirement. For example, a detector of 7 mm diameter can easily be used for all uniform scanning fields of 21 mm and greater. However, commissioning a single spot with a full-width-half-maximum of 10 mm, similar to the new Varian or IBA delivery system, poses different detector requirements.

The MLIC or Zebra could be adapted for pencil beam spot scanning (PBS). Instead of using a small detector element in a large proton field, the future detector could be composed of large detector elements for a small (i.e. spot) proton field. A Multi Layer Faraday Cup, as installed in the upstream uniform scanning beamline, is an example of such a detector. However, that detector is composed entirely of copper and an insulator, and importantly, is not an ion chamber. PTW has created a “Bragg peak chamber”, which is a parallel plate ion chamber of approximately 4.5 cm radius. This detector is scanned in a water phantom in order to characterize a Bragg peak. By creating an array of similar chambers, an entire proton beam spot could be characterized. This is a natural evolution for this detector project as applied to an advanced spot scanning beam delivery system. Currently, I am in discussion with colleagues and informally multiple

vendors have expressed interest. With more experience in PBS, the project will become more concrete and a clearer cost-benefit analysis will be made.

5.1.2 Uniform Scanning Beam Delivery

5.1.2.1 Scan Pattern

Implementation of the raster scanning pattern has become the default option in uniform scanning proton therapy. The Indiana University, IBA and emerging vendor solutions focus on delivering a uniformly scanned raster pattern, similar to that studied and implemented in this work. However, further scan pattern optimization could improve the overall quality of the proton radiation field.

Tailoring the scan pattern to the patient-specific aperture reduces the secondary neutron radiation from the aperture and therefore reduces the overall secondary and scattered radiation to the patient. In this study, the overscan margin improved the uniformity within the proton radiation field. However, the scan pattern was optimized to the maximum field size of the individual snout. For example, a 5cm diameter field would be treated using a 10 cm diameter snout and a corresponding patient specific aperture. The overscan margin would be defined by the 10 cm snout the scan pattern, not the 5 cm aperture. If the scan pattern was varied according to the patient specific aperture size, the overscan margin would be reduced, reducing neutron dose to the patient. However, this approach would have drawbacks. By varying the scanned field size, the use of look-up tables to predict output factor would become a function of both the aperture field size and scanned field size. Furthermore, many uniform scanning systems do not have the nozzle detector elements to verify the scanned field size, and therefore, the beam delivery safety system and interlocks would require additional modification.

5.1.2.2 Rescanning or Repainting

The uniform scanning system irradiates the target approximately 15 times per second (i.e. a 15 Hz scan) in the transverse profile but only once along the longitudinal axis. Because of this, dose artifacts can be introduced to moving targets. Several proposed options, in various stages of implementation across the proton therapy vendors, exist to mitigate this issue. However, very little data exists on overall efficacy of the individual approaches.

Reirradiation or repainting the target is a common remedy for the motion-induced dose artifacts. By repainting the target several times during irradiation, the motion artifact is average by the number of repaints. The total dose is subdivided to each single paint. In other words, a 50 MU field repainted 5 times yields 10 MU per single paint. As the number of repaints increases, the importance of monitor chamber ionization measurement resolution increases. Though the Indiana University nozzle could repaint targets, the beam delivery was limited to a layer-dose resolution of one monitor unit (MU). In order to safely repaint the target multiple times, the resolution of the monitor chamber would require improvement. Furthermore, a new parameter would be required in the treatment control system. For example, the parameter could be called “number of re-irradiations”. The treatment control system would need to translate the proton field from the treatment planning system into multiple deliveries.

5.2 Summary of Results and Conclusions

5.2.1 Detectors

The uniform scanning detector development represents a significant contribution to the field of scanning bream measurement. Prior to the development of the Multi Layer Ion

Chamber (MLIC), no detector existed for measuring a scanning radiation field in a clinically efficient manner without sacrificing the quality of the data.

During the MLIC prototype development, several design elements were investigated and identified as critical – signal pad size, signal to noise ratio, materials, and required sampling. The exercise of designing and fabricating a prototype ultimately led to an improved design and fabrication phase for the clinically implemented version. The MLIC gathered data with 1.8 mm spatial sampling, which was adequate to characterize a proton depth-dose, in a user-friendly, efficient manner. The calibration routine proved reliable and efficient, accounting for day-to-day fluctuations of the ion chamber scaling factor. The overall clinical efficiency gain was estimated at a factor of 20. The MLIC proved critical to commissioning and characterizing the uniform scanning system. The detector design and utility was ultimately adapted by IBA Dosimetry through a clinical task force.

The adapted water phantom jig for the Matrixx detector proved useful for improving the overall efficiency of acquiring uniform scanning commissioning data. However, the improvement in efficiency was less substantial when compared to the MLIC. The cost of the adaptation and the introduction of non-optimal venting of the ion chamber decreased the utility of the detector jig. Nonetheless, the improvement in characterization of multiple water-equivalent depths within the uniform scanning dose volume demonstrated the usefulness of the detector jig. This design was adapted by IBA Dosimetry through a clinical task force and resulted in the commercially-available DigiPhant, a translational waterproof jig for acquiring transverse profile data with the Matrixx detector.

5.2.2 Longitudinal Optimization and Characterization

The binary range modulator (BRM) in the uniform scanning nozzle required clinical implementation and optimization. The developers created and installed the device in the nozzle. After installation, the full integration of the device required several iterations.

The pristine Bragg peak characterization preceded the development of the layer definition files because the layer spacing and weights depend on the Bragg peak energy and width. The pristine Bragg peak is the building block of a spread out Bragg peak (SOBP). Based on the pristine Bragg peak measurements, the BRM was “programmed” with layer definition files, which were used as the blueprint of each spread out Bragg peak. The layer definition files were created manually and empirically, as no software or simulation program was available. A significant portion of the BRM project was defining the format, method and content of the layer definition file creation.

Following the integration of the layer definition files, the performance of the BRM required assessment and characterization. During the clinical characterization process, a skewness parameter was defined in order to correct the tilt (aka “skewness) of the SOBP. The skewness parameter was created and mapped as a function of range in water. This skewness parameter became an integral part of the treatment control system. Across the clinical energy spectrum, the BRM delivered spread out Bragg peaks within clinical specification – within 0.1 cm for each range and within +/- 2.5% in uniformity.

5.2.3 Transverse Optimization and Characterization

The wobbling magnet in the uniform scanning nozzle required clinical implementation and optimization. The developers created and installed the device in the nozzle. After installation, the full integration of the device required several iterations.

The input waveform file, which controlled the various scanning parameters, was created and optimized. The critical parameters of amplitude, spacing and scan density were defined and used to create a scan pattern. After investigating several scan patterns, a simple raster pattern was implemented. The scan density was found to be a function of the beam spot size, and therefore implemented in two discrete energy regimes. For smaller beam spots at higher energy, a tighter scan spacing, and increased line density, was used to achieve acceptable uniformity. For lower energy, a looser scan spacing was suitable. The scan amplitude, also described as the overscan margin of the aperture, was critical to maintain flatness and reduce the significance of the “dose shoulder” at the aperture edges. Scan amplitude of between two or three standard deviations of the beam spot sigma was adequate.

Following the optimization of the scan pattern, the performance of the wobbling magnet was assessed and characterized. Across the clinical spectrum, the uniformity of transverse profile was within clinical specification, with the exception of ranges in water of greater than 25.0cm. In that case, the flatness uniformity increased to 0.5% out of tolerance, which was deemed clinically insignificant by the physicists and physicians at the proton center. The symmetry of all fields at all ranges in water exceeded clinical specification. The penumbra was characterized and preserved through the

implementation of a single wobbling magnet design, as compared to the passive scattering system.

6 Work Cited

1. Wilson RR. "Radiological use of fast protons." Radiology. 45(5). 487-491. 1946.

2. Slater J, Miller D, Archambeau J. "Development of hospitbal-based proton beam treatment center." Int. J. Radiat. Oncol. Biol. Phys. 14(4). 761-765. 1988.

3. Koehler A, Schneider R, Sisterson J. "Flattening of proton dose distributions for large fields." Med. Phys. 4, 297–301. 1977.

4. Lu H, Brett R, Engelsman M, Slopsema R, Kooy H, Flanz J. "Sensitivities in the production of spread-out Bragg peak dose distributions by passive scattering with beam current modulation." Med. Phys. 34, 3844–3853. 2007.

5. Koehler A, Schneider R, Sisterson J. "Range modulators for protons and heavy ions." Nucl. Instrum. Methods. 131, 437–440. 1975.

6. Lu H, Kooy H. "Optimization of current modulation function for proton spread-out Bragg peak fields." Med. Phys. 33, 1281–1287. 2006.

7. Nohtomi A, Sakae T, Tsunashima Y, et al. "Dosimetry of pulsed clinical proton beams by a small ionization chamber." Med. Phys. 28:7:1431-1435. 2001.

8. Vatnitsky S, Moyers M, Vatnitsky A. "Parallel-plate and thimble ionization chamber calibrations in proton beams using the TRS 398 and ICRU 59 recommendations."

Standards and Codes of Practice in Medical Radiation Dosimetry. Proceedings Series of the International Atomic Energy Association. Vol.2. Vienna 2003.

9. Schreuder A. "A small ionization chamber for dose distribution measurements in a clinical proton beam." *Advances in Hadrontherapy*. Elsevier Science, Amsterdam. 284-289. 1997.

10. Karger C, Jakel O, Palmans H, Kanai T. "Dosimetry for ion beam radiotherapy." Phys. Med. Biol. 55(21), 193-234. 2010.

11. Cirio R, Garelli E, Schulte R, Amerio S, Boriano A, Bourhaleb F, Coutrakon G, Donetti M, Giordanengo S, Koss P, Madon E, Marchetto F, Nastasi U, Peroni C, Santuari D, Sardo A, Scielzo G, Stasi M, Trevisiol E. "Two-dimensional and quasi-three-dimensional dosimetry of hadron and photon beams with the magic cube and the pixel ion chamber." Phys. Med. Biol. 49(16), 3713–3724. 2004.

12. Amerio S, Boriano A, Bourhaleb F, Cirio R, Donetti M, Fidanzio A, Garelli E, Giordanengo S, Madon E, Marchetto F, Nastasi U, Peroni C, Piermattei A, Sanz Freire CJ, Sardo A, Trevisiol E. "Dosimetric characterization of a large area pixel segmented ionization chamber." Med. Phys. 31(2), 414-420. 2004.

13. Troja SO, Egger E, Francescon P, Gueli AM, Kacperek A, Coco M, Musmeci R, Pedalino A. "2D and 3D dose distribution determination in proton beam radiotherapy with Gafchromic film detectors." Technol Health Care. 8(2), 155-164. 2000.

14. Boon SN, van Luijk P, Schippers JM, Meertens H, Denis JM, Vynckier S, Medin J, Grusell E. "Fast 2D phantom dosimetry for scanning proton beams." Med. Phys. 25(4), 464-475. 1998.

15. Nichiporov D, Kostjuchenko V, Puhl JM, Bensen DL, Desrosiers MF, Dick CE, McLaughlin WL, Kojima T, Coursey BM, Zink S. "Investigation of applicability of alanine and radiochromic detectors to dosimetry of proton clinical beams." Appl. Radiat. Isot. 46(12), 1355-1362. 1995.

16. Vatnitsky S, "Radiochromic film dosimetry for clinical proton beams." Appl. Radiat. Isot. 48(5), 643–651. 1997.

17. Anferov V, Broderick B, Collins J, Friesel D, Jenner D, Jones W, Katuin J, Klein S, Starks W, Self J, and Schreuder A. "The Midwest Proton Radiation Institute project at the Indiana University Cyclotron Facility." *Cyclotrons and their Applications 2001. Editor* Marti F. New York. Issue 1, 27-29. 2001.

18. D. L. Friesel, V. Anferov, J. Collins, J. Katuin, S. Klein, D. Nichiporov, M. Wedekind. "The Indiana University proton therapy system." *European Particle Accelerator Conference.* Edinburgh, UK. 2349. 2006.

19. Katuin J, Schreuder A, Starks W, et al. "The use of industrial robots arms for high precision patient positioning." 17th International Conference on the Applications of Accelerators in Research and Industry. Denton, Texas. November 2002.

20. Nichiporov D. “The choice of design for MPRI gantry nozzle.” Particle Therapy Co-Operative Group (PTCOG) 41. Midwest Proton Radiotherapy Institute. Bloomington, Indiana. October 2004.

21. V. Anferov. “Combined *X*–*Y* scanning magnet for conformal proton radiation therapy.” Med. Phys. 3, 815–818. 2005.

22. Lomax A, Bohringer T, Bolsi A, et al. “Treatment planning and verification of proton therapy using spot scanning: initial experiences.” Med. Phys. 31(11)., 3150-3157. 2004.

23. Lomax A. “Intensity modulated methods for proton radiotherapy.” Phys. Med. Biol. 44, 185-205. 1999.

24. Gillin M, Sahoo N, Bues M, Ciangaru G, Sawakuchi G, Poenisch F, Arjomandy B, Marin C, Titt U, Suzuki K, Smith A, Zhu X. “Commissioning of the discrete spot scanning proton beam delivery system at the University of Texas M. D. Anderson Cancer Center, Proton Therapy Center, House.” Med. Phys. 37(1). 154-163. 2010.

25. Kanai T, Kawachi K, Kumamoto Y, Ogawa H, Yamada T, and Matsuzawa H. “Spot scanning system for proton radiotherapy.” Med. Phys. 7, 365–369. 1980.

26. International Commission on Radiation Units and Measurements. Report 59. “Clinical proton dosimetry part 1: beam production, beam delivery and measurement of absorbed dose.” 1998.

27. Medin J, Andreo P, Vynckier S. “Comparison of dosimetry recommendations for clinical proton breams.” Phys. Med. Biol. 45, 3195-3211. 2000.

28. Coray A, Pedroni E, Boehringer T, et al. “Dosimetry with the scanned proton beam on the Paul Scherrer Institute gantry.” Standards and Codes of Practice in Medical Radiation Dosimetry. Proceedings Series of the International Atomic Energy Association. Vol.2. Vienna 2003.

29. International Atomic Energy Association. Technical Report Series Number 398. “Absorbed dose determination in external beam radiotherapy: an international code of practice for dosimetry based on standards of absorbed dose to water.” 2001.

30. International Commission on Radiation Units and Measurements. Report 78. “Prescribing, Recording and Reporting Proton-Beam Therapy.” 2007.

31. Nichiporov D, Solberg K, His W, Wolanski M, Mascia A, Farr J, Schreuder A. “Multichannel detectors for profile measurements in clinical proton fields.” Med. Phys. 34(7). 2683-2690. 2007.

32. Bortfeld T. “An analytical approximation of the Bragg curve for therapeutic proton beams.” Med. Phys. 24(12), 2024-2033. 1997.

33. Dhanesar S, Sahoo N, Kerr M, Taylor MB, Summers P, Zhu XR, Poenisch F, Gillin M. “Quality assurance of proton beams using a multilayer ionization chamber system.” Med. Phys. 40(9), 2013.

34. Farr J, Mascia A, His W, Allgower C, Jesseph F, Schreuder A, Wolanski M, Nichiporov D, Anverov V. "Clinical characterization of a proton beam continuous scanning system with dose layer stacking." Med. Phys. 35(11), 4945-4954. 2008.

35. Anferov V. "Scan pattern optimization for uniform scanning beam scanning." Med. Phys. 36(8), 3560-3567. 2009.